Charge Transport in Disordered Semiconductors in Solid State Sensitized Solar Cells: Influence on Performance and Stability

Tomas Leijtens

St Anne's College, Oxford

Thesis submitted in fulfilment of the requirements for the degree of Doctor of Philosophy at the University of Oxford.

Trinity Term, 2014

Charge Transport in Disordered Semiconductors in Solid State Sensitized Solar Cells: Influence on Performance and Stability

Tomas Leijtens, St Anne's College, Oxford

Thesis submitted in fulfilment of the requirements for the degree of Doctor of Philosophy at the University of Oxford. Trinity Term, 2014

Abstract

This thesis studies parameters influencing both the performance and stability of solid state sensitized solar cells (ssSSCs). ssSSCs benefit from their low materials and manufacturing processing costs, a consequence of using solution processed materials. However, solution processed materials are often structurally and electronically disordered. By characterizing fully operational ssSSCs and their charge transport properties, this thesis elucidates the factors limiting charge transport and proposes routes towards both improved photovoltaic conversion efficiency and long-term stability.

Chapter 2 provides an explanation of the operation of ssSSCs, while Chapter 3 discusses the basic methods used in this thesis. Having set this background, Chapter 4 explores the interaction between atmospheric oxygen and charge doping mechanisms in the organic semiconductors used in ssSSCs. To understand the implications of the findings presented in Chapter 4, a new technique, "transient mobility spectroscopy", was developed to understand the evolution of balanced charge transport behaviour of disordered semiconductors at different operating conditions in ssSSCs. This technique is presented in full in Chapter 5.

The understanding gained in Chapters 4 and 5 suggest that alternative light absorbers with higher extinction coefficients may be beneficial to improving the performance of ssSSCs. Chapter 6 discusses the use of an organometal trihalide perovskite, as light absorber in ssSSCs. Using time resolved techniques, the charge transport and recombination mechanisms in various device architectures are explored, allowing suggestions to be made towards future improvements.

Chapter 7 uses the technique presented in Chapter 5 to understand a rapid degradation mechanism of working ssSSCs. Particular focus is placed on the titanium dioxide charge-transporting layer. Building on this newfound understanding, two methods for attaining stable photovoltaic performance are provided, a great step forward for this technology.

Acknowledgements

First, I want to thank my family for their unwavering support and encouragement throughout the course of my D.Phil and my studies in general. Papa, thank you for stressing the importance of taking my education as far as possible. You have always shown great enthusiasm and pride and towards my scientific endeavours, giving me some much needed encouragement and motivation. Mama, thank you for being the caring, wonderful mother you always have been, even when separated by oceans and continents. The visits home, and particularly all your "verwennerij", have been something to look forward to over the last 7 years. The support you have both given me has been absolutely essential for all of my studies, in many ways. Ik hou van jullie.

Of course, I also owe a great deal to my research supervisor, Professor Henry Snaith, who has had the largest influence of anyone on the course of my studies at Oxford. I should thank Henry for many things, but mostly for showing me how exciting scientific research is. His incredible enthusiasm has been inspiring and infectious, so that there has never been a boring or tedious moment throughout three years of experimental research. His approach to research and ability to identify the important problems and solutions has also been eye opening. He has been a great example, and not just for his arm wrestling prowess.

Great thanks go out to Dr. Alan Sellinger, who gave me my first introduction to research at Stanford. Continued contact and collaboration with Alan has been invaluable over the past three years, and I would not have started the long road towards a research degree had I not met Alan. Thanks go out to collaborators both at Oxford and elsewhere, who have been essential in conducting much of the research presented in this thesis, with special thanks to Dr. Joël Teuscher, Dr. Antonio Abate, Jongchul Lim, Dr. Sandeep Pathak, Nakita Kimberly, Sam Stranks, Giles Eperon, Dr. Pablo Docampo, Dr. Stefan Guldin, Beat Lauber and Davide Moia. To the group at the IIT in Milan, I am very thankful to you for putting up with my general ignorance of physics; you have taught me a great deal in my six months with you.

A very special thanks goes out to all the Snaithlings. We've had good laughs, performed terribly at football tournaments, and done some OK science in between. It has been great to work with all of you, and I hope we all have the opportunity to continue to do so. Nakita, I owe you a massive thank you. You've been spoiling me since our first year with delicious snacks, meals and back rubs. Thanks also for putting up with my sloppy behaviour in the cleanroom, and for only banning me twice.

To 84 Percy street and its inhabitants (Ian, Roweida, Conor, John, Jonny, and Jonny); I want to say that you've been a good and loving house. But that would be wrong, and also completely against the spirit that we strive to maintain in the house. Thanks for inducting me into your odd sense of humour, making jokes and references I generally struggle to understand, filming my greatest moments, and for putting up with some of my more intrusive hobbies. I maintain that the barrel is a good use of space. The study centre was not.

A general thanks to everyone I have met through my work in the physics department and through college. You have all contributed to making my stay in Oxford one that I will always look back on with good memories.

List of Publications

(1) Leijtens, T.; Ding, I. K.; Giovenzana, T.; Bloking, J. T.; McGehee, M. D.; Sellinger, A. Hole Transport Materials with Low Glass Transition Temperatures and High Solubility for Application in Solid-State Dye-Sensitized Solar Cells. *ACS Nano* **2012**, *6*, 1455–1462.

(2) *Abate, A.; *Leijtens, T.; Pathak, S.; Teuscher, J.; Avolio, R.; Errico, M. E.; Kirkpatrik, J.; Ball, J. M.; Docampo, P.; McPherson, I.; et al. Lithium Salts as "Redox Active" P-Type Dopants for Organic Semiconductors and Their Impact in Solid-State Dye-Sensitized Solar Cells. *Phys. Chem. Chem. Phys.* **2013**, *15*, 2572–2579.

(3) Agrawal, S.; Leijtens, T.; Ronca, E.; Pastore, M.; Snaith, H.; De Angelis, F. Modeling the Effect of Ionic Additives on the Optical and Electronic Properties of a Dye-Sensitized TiO2 Heterointerface: Absorption, Charge Injection and Aggregation. *J. Mater. Chem. A* **2013**, *1*, 14675–14685.

(4) Leijtens, T.; Lim, J.; Teuscher, J.; Park, T.; Snaith, H. J. Charge Density Dependent Mobility of Organic Hole-Transporters and Mesoporous TiO2 Determined by Transient Mobility Spectroscopy: Implications to Dye-Sensitized and Organic Solar Cells. *Adv. Mater.* **2013**, *25*, 3227–3233.

(5) Crossland, E. J. W.; Noel, N.; Sivaram, V.; Leijtens, T.; Alexander-Webber, J. A.; Snaith, H. J. Mesoporous TiO2 Single Crystals Delivering Enhanced Mobility and Optoelectronic Device Performance. *Nature* **2013**, *495*, 215–219.

(6) Leijtens, T.; Eperon, G. E.; Pathak, S.; Abate, A.; Lee, M. M.; Snaith, H. J. Overcoming Ultraviolet Light Instability of Sensitized TiO_2 with Meso-Superstructured Organometal Tri-Halide Perovskite Solar Cells. *Nat. Commun.* **2013**, *4*, 2885.

(7) Sivaram, V.; Crossland, E. J. W.; Leijtens, T.; Noel, N. K.; Alexander-Webber, J.; Docampo, P.; Snaith, H. J. Observation of Annealing-Induced Doping in tio2 Mesoporous Single Crystals for Use in Solid State Dye Sensitized Solar Cells. *J. Phys. Chem. C* **2014**, *118*, 1821–1827.

(8) Stranks, S. D.; Eperon, G. E.; Grancini, G.; Menelaou, C.; Alcocer, M. J. P.; Leijtens, T.; Herz, L. M.; Petrozza, A.; Snaith, H. J. Electron-Hole Diffusion Lengths Exceeding 1 Micrometer in an Organometal Trihalide Perovskite Absorber. *Science (80-.).* **2013**, *342*, 341–344.

(9) Leijtens, T.; Lauber, B.; Eperon, G. E.; Stranks, S. D.; Snaith, H. J. The Importance of Perovskite Pore Filling in Organometal Mixed Halide Sensitized TiO2-Based Solar Cells. *J. Phys. Chem. Lett.* **2014**, 1096–1102.

(10) *Docampo, P.; *Guldin, S.; *Leijtens, T.; Noel, N. K.; Steiner, U.; Snaith, H. J. Lessons Learned: From Dye-Sensitized Solar Cells to All-Solid-State Hybrid Devices. *Adv. Mater.* **2014**, n/a–n/a.

(11) Deschler, F.; Price, M.; Pathak, S.; Klintberg, L. E.; Jarausch, D.-D.; Higler, R.; Hüttner, S.; Leijtens, T.; Stranks, S. D.; Snaith, H. J.; et al. High Photoluminescence Efficiency and Optically Pumped Lasing in Solution-Processed Mixed Halide Perovskite Semiconductors. *J. Phys. Chem. Lett.* **2014**, 1421–1426.

(12) Wojciechowski, K.; Saliba, M.; Leijtens, T.; Abate, A.; Snaith, H. J. Sub-150 °C Processed Meso-Superstructured Perovskite Solar Cells with Enhanced Efficiency. *Energy Environ. Sci.* **2014**, *7*, 1142–1147.

(13) Snaith, H. J.; Abate, A.; Ball, J. M.; Eperon, G. E.; Leijtens, T.; Noel, N. K.; Stranks, S. D.; Wang, J. T.-W.; Wojciechowski, K.; Zhang, W. Anomalous Hysteresis in Perovskite Solar Cells. *J. Phys. Chem. Lett.* **2014**, 1511–1515.

(14) Pathak, S. K.; Abate, A.; Leijtens, T.; Hollman, D. J.; Teuscher, J.; Pazos, L.; Docampo, P.; Steiner, U.; Snaith, H. J. Towards Long-Term Photostability of Solid-State Dye Sensitized Solar Cells. *Adv. Energy Mater.* **2014**, n/a–n/a.

* Denotes equal contribution authorships

Table of Contents

Chapter 1

Introduction

1.1

Background and Motivation

Whether it be for large scale power supply or personal transportation, combustion of fossil fuels has been an extremely low cost and easily accessible energy source for over a century. Over the last few decades, however, it has become accepted that some of the most pressing problems facing modern society as a whole stem from our continued and increasing reliance on fossil fuels as our primary energy source[1,2]. Indeed, the supply of fossil fuels is limited and being rapidly depleted, while our demand for energy is only increasing with a rising global population and rapid industrial growth around the world. Even if we continue to discover new sources of fossil fuels, the impact of fossil fuel emissions on the global climate cannot be ignored. The emission of greenhouse gases, an unavoidable consequence of fossil fuel combustion, has led to rising global temperatures. If current trends continue, global temperatures will continue to rise with disastrous consequences on weather patterns and the frequency of coastal flooding, natural ecosystems, and the future of human society as it is now[1–3].

As a consequence, developing renewable, cheap, and clean energy sources has become paramount for society to continue its energy consumption unhindered. Of the available alternatives to fossil fuels, solar energy is the most abundant. And of the methods with which to convert solar irradiation to useable energy, photovoltaic devices are some of the most promising, directly converting incoming photons to electrical power. In fact, the current global energy demand could be met by covering

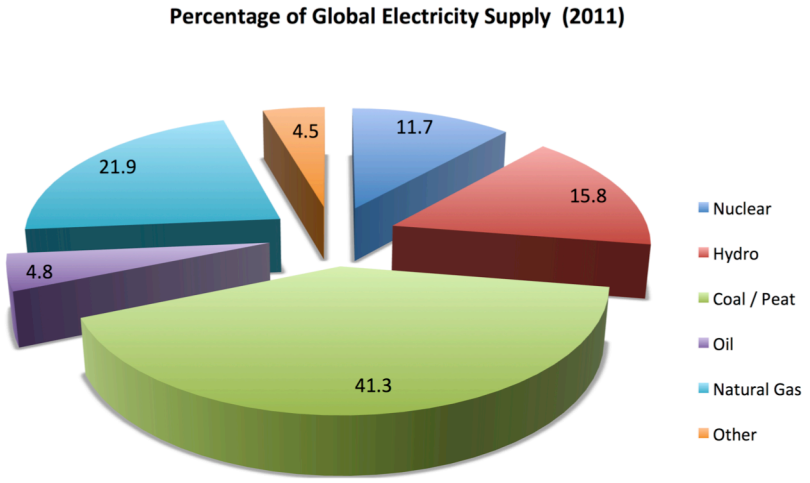

Figure 1.1. Pie chart of the sources of global electricity production in 2011. Other, including photovoltaic, wind, and hydrothermal power, only accounted for less than 5 % of all energy supply. Data derived from the International Energy Agency[3].

just 0.4 % of the Earth's available surface area with 15 % efficient photovoltaic devices.

The most efficient photovoltaic solar cells to date are based on crystalline, inorganic semiconductors such as Silicon or Gallium Arsenide. The best performing of such devices have reached impressive power conversion efficiencies (PCE) over 28 %, already approaching the maximum theoretical efficiency limit of 31 – 33 % for single junction devices, known as the Shockley-Queisser limit[4]. Devices with PCEs over 37 % have also been obtained by preparing multi- junction solar cells comprised of layers of different inorganic semiconductors[5]. Such high performances seem to easily meet the efficiency requirements for a large scale switch to photovoltaic energy production. The drawback to this class of solar cells, however, is their reliance of high quality inorganic semiconductor films. This requires expensive and energy intensive processing. As a result, long financial and energy payback times are limiting widespread adoption of such photovoltaic devices.

Solution processed semiconductors have emerged as highly promising materials for use in a wide range of optoelectronic devices such as field effect transistors (FETs), light emitting diodes (LEDs), and photovoltaic devices. Devices comprising solution processed semiconductors benefit from tunable, cheap and easily accessible materials that allow for low-cost and readily scalable processing such as reel-to-reel printing. As such, photovoltaics comprised of these materials

should sidestep the financial and energetic costs associated with photovoltaics made of the aforementioned conventional crystalline inorganic semiconductors.

It is then not surprising that solution processed photovoltaics have become a subject of intense research. One of the most promising of solution processed photovoltaic technologies is the sensitized solar cell (SSC), developed in its current form in 1991 by Brian O'Regan and Michael Grätzel[6]. Separating the fundamental processes of light absorption, charge separation, and charge collection in separate material components, sensitized solar cells offer a unique chance to separately study and tailor the fundamental processes of solar energy conversion. As a result, dye sensitized solar cells have reached impressive PCEs of over 12 % using only low cost materials and processing techniques[7]. In addition to dyes, solution processed inorganic absorbers, particularly organometal trihalide perovskite absorbers, have recently attracted a great deal of attention for use in solid state sensitized solar cells (ssSSCs) with similar operating mechanisms as traditional dye sensitized solar cells[8–11]. Such solar cells have rapidly surpassed the performance of traditional dye sensitized solar cells, boasting PCEs over 16 %, and show promise to reach even higher performances in the upcoming years.

1.2

Goals of the Thesis

With dye and perovskite sensitized solar cells rapidly approaching efficiencies suitable for commercial adoption, one of the major challenges remaining to be solved is the question of their stability under prolonged exposure to sunlight. Indeed, the industry standard of 25 year lifetimes under full solar illumination must be met if sensitized solar cells are to be considered a viable alternative to the current generation of crystalline inorganic photovoltaics. With this in mind, the current thesis focuses only on solid state sensitized solar cells (ssSSCs), with no liquid components that could leak or be corrosive.

Since their inception in 1998 by Bach and Grätzel[12], dye sensitized ssSSCs have been the focus of much research attention, but have still fallen short of their

potential[13]. This is due to an inability to make ssSSCs thick enough to absorb a large fraction of incident light[14]. While several suggestions for improvements have been made, little progress has been made with regard to power conversion efficiency. The working principles of ssSSC operation will be presented in Chapter 2, along with a general description of solution processed semiconductors.

One likely reason for the poor performances of ssSSCs is that the processes of charge transport and collection in the ssSSCs have not been completely understood, and may well be limited by the use of low mobility organic semiconductors as one of the charge transporting layers. The main charge transporting layers ssSSCs are comprised of titanium dioxide and organic semiconductors, which can be either conjugated polymers or aromatic small molecules. Organic semiconductors are different from crystalline inorganic semiconductors; rather than being comprised of closely packed atoms held together by strong covalent bonds in a repetitive crystal lattice, they are composed of many individual polymer chains or single molecules held together by relatively weak Van Der Waals forces. Hence, organic semiconductors do not form continuous energy bands such as conduction bands and valence bands. Instead, the electron wavefunction overlap for the lowest and highest occupied molecular orbitals (LUMO and HOMO respectively) only extends for several monomer units in conjugated polymers, and there is no true long range electronic delocalization in the case of films made of small molecules. As a result, electronic states are more localized, slowing charge transport and also increasing the likelihood for electrons in the HOMO level of many organic semiconductors to interact with atmospheric oxygen to form charge transfer complexes and oxidize the semiconductor.

This will form the basis for the first two scientific Chapters of this thesis. Chapter 4 will discuss the interaction of the hole transporting organic semiconductor with oxygen, and the importance thereof on charge transport in ssSSCs. In particular, Chapter 4 will demonstrate that p-doping the organic hole transporter is absolutely essential to efficient device performance, and that this can be accomplished by the use of lithium salts and oxygen. To further quantify the balance between electron and hole transport in ssSSCs, a novel technique is developed in Chapter 5: transient mobility spectroscopy. This technique makes it possible to determine the charge

carrier mobility as a function of charge carrier density in solar cell architecture, making it uniquely valuable to study charge transport in ssSSCs. Using this technique, the nature of charge transport in both inorganic and organic charge transporting layers in ssSSCs is elucidated, leading to an improved understanding of the material properties that are required of the organic hole transporter to be able to improve ssSSC performance. The understanding gained in Chapters 4 and 5 yields new insights into why it has proven impossible to make thick ssSSCs capable of absorbing large fractions of incident light. The conclusion drawn is that higher mobility, and especially transparent, organic hole transporters are essential to realize dye sensitized ssSSCs with high light harvesting efficiencies.

Rather than make solar cells thicker to absorb more light, it is also possible to use more highly absorbing sensitizers. Organometal trihalide perovskites have recently emerged as promising absorbers for ssSSCs, allowing thin devices to reach remarkable performances[9,15]. Chapter 6 of this thesis discusses ssSSCs using this absorber, and exploits its unique properties to study device architectures that are quite different from that in classic ssSSCs. Insight is gained into the working mechanisms of the most high performance perovskite sensitized ssSSCs, particularly with regards to charge transport and collection, yielding clear directions towards future improvements.

Having outlined pathways to making both more efficient dye sensitized and perovskite sensitized ssSSCs, it is important to consider the question of their stability under prolonged exposure to working conditions. While this question becomes increasingly important as device performances are becoming increasingly competitive, surprisingly little research has been published on the topic. As discussed above, oxygen is likely to interact with the organic hole transporting layers used in ssSSCs. Titanium dioxide also readily interacts with water and oxygen in the environment through defect sites at the crystal surfaces, changing the material's defect chemistry. Many of these reactions are photoinduced, making them relevant to solar cell operating conditions. While such behaviour has been well characterized for pure titanium dioxide in a variety of forms (single crystal, nanocrystaline, or thin film), few studies have been carried out to understand the impact on ssSSCs. Since changes at the oxide's surface may well play an important role in charge separation,

trapping, and charge collection in sensitized solar cells, understanding the impact of the atmosphere, under working conditions, will be essential to realizing stable ssSSCs with long working lifetimes under operating conditions.

Using the understanding of charge transport mechanisms in ssSSCs gained in Chapters 4, 5, and 6, as well as the new technique developed in Chapter 5, Chapter 7 presents the first thorough understanding of the rapid degradation of ssSSCs under full solar illumination. The mesoporous TiO_2 layer is identified as being unstable to ultraviolet light exposure, with the resulting degradation being dependent on the atmospheric composition. This presents a major hurdle to eventual employment for large-scale and long-term power generation. Having identified the mechanism behind this rapid degradation, two methods are presented that appear to solve the problem. By changing the device architecture and removing the mesoporous TiO_2 altogether, stable photo-current of 1000 hrs is demonstrated, paving the road to commercialization.

Hence, this thesis is aimed first at understanding the mechanisms of charge carrier transport in ssSSCs. This is then used to understand limiting factors in ssSSC performance and stability. The result is that pathways to both improved performance and stability are clearly highlighted by the end of the thesis.

1.3

References

(1) Oreskes, N. *Science* **2004**, *306*, 1686.

(2) Anderson, K.; Bows, A. *Philos. Trans. A. Math. Phys. Eng. Sci.* **2011**, *369*, 20.

(3) Adrian, G.; Agency, I. E. *Key World Energy Statistics*; 2013; Vol. 2013, pp. 1–82.

(4) Shockley, W.; Queisser, H. J. *J. Appl. Phys.* **1961**, *32*, 510.

(5) Green, M. A.; Emery, K.; Hishikawa, Y.; Warta, W. *Prog. Photovoltaics Res. Appl.* **2011**, *19*, 84.

(6) O'Regan, B.; Grätzel, M. *Nature* **1991**, *353*, 737.

(7) Yella, A.; Lee, H.-W.; Tsao, H. N.; Yi, C.; Chandiran, A. K.; Nazeeruddin, M. K.; Diau, E. W.-G.; Yeh, C.-Y.; Zakeeruddin, S. M.; Grätzel, M. *Science (80-.).* **2011**, *334*, 629.

(8) Hodes, G. *Science* **2013**, *342*, 317.

(9) Lee, M. M.; Teuscher, J.; Miyasaka, T.; Murakami, T. N.; Snaith, H. J. *Science (80-.).* **2012**, *338*, 643.

(10) Kojima, A.; Teshima, K.; Shirai, Y.; Miyasaka, T. *J. Am. Chem. Soc.* **2009**, *131*, 6050.

(11) Kim, H.-S.; Lee, C.-R.; Im, J.-H.; Lee, K.-B.; Moehl, T.; Marchioro, A.; Moon, S.-J.; Humphry-Baker, R.; Yum, J.-H.; Moser, J. E.; Grätzel, M.; Park, N.-G. *Sci. Rep.* **2012**, *2*.

(12) Bach, U.; Lupo, D.; Comte, P.; Moser, J. E.; Weissortel, F.; Salbeck, J.; Spreitzer, H.; Grätzel, M. *Nature* **1998**, *395*, 583.

(13) Snaith, H. J. *Adv. Funct. Mater.* **2009**, NA.

(14) Hardin, B. E.; Snaith, H. J.; McGehee, M. D. *Nat. Photonics* **2012**, *6*, 162.

(15) Heo, J. H.; Im, S. H.; Noh, J. H.; Mandal, T. N.; Lim, C.-S.; Chang, J. A.; Lee, Y. H.; Kim, H.; Sarkar, A.; NazeeruddinMd, K.; Grätzel, M.; Seok, S. Il. *Nat Phot.* **2013**, *7*, 486.

Chapter 2

Background*

*Much of the information provided in this section is just a basic introduction to semiconductor properties and solar cell physics, and the reader is referred to the standard texts by Sze et al[1] and Nelson et al[2] for further information.

2.1

Semiconductors

Semiconductors form the basic building blocks of photovoltaic cells. Figure 2.1 depicts the energetic differences for electrons in metals, semiconductors, and n-doped semiconductors. Metal atoms, being readily ionisable, form crystalline materials with highly delocalized and mobile electrons. This is depicted in Figure 2.1 by the presence of many filled and unfilled electronic states with very similar energies. The Fermi level (E_F) is defined as the energy at which there is a 50 % probability of filling an electronic state, regardless of whether a state exists or not.

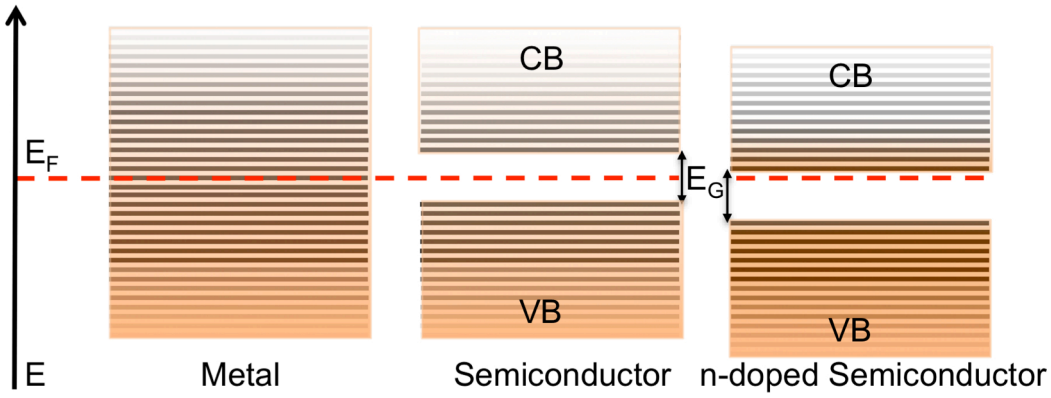

Figure 2.1. The difference between available electronic states is demonstrated for metals, intrinsic semiconductors, and n-doped semiconductors. The lines represent available states, while darker orange shading signifies filled states and lighter shading signifies empty states. In metals, the Fermi level (E_F) is in the middle of a continuum of states, such that there are many filled states at the Fermi energy. In a semiconductor, E_F is in the middle of a forbidden band, the bandgap (E_G), and there are no filled states in the CB in the absence of thermal or light excitation. In n-doped semiconductors, E_F is just below the CB, and the CB is filled with an electron density dependent on the doping level.

Hence the Fermi level in a metal is positioned in the middle of a continuum of electronic states and the band is typically half filled. In metals, electrons can be readily excited between states, leading to a high concentration of mobile carriers even at low temperatures. A semiconductor, however, is defined as having two bands of such electronic states, separated by an energy gap termed the band gap. These bands are termed the valence band (VB) and conduction band (CB), with the fermi level in the middle of the gap as shown in Figure 2.1.

Only electrons in the conduction band (and hence an energy greater then the bandgap) are free to move through the material. An electron vacancy, treated as a positively charged equivalent to an electron and termed a "hole", only moves in the valence band. If no energy is supplied to the material, then there will be no electrons in the conduction band and no holes in the valence band, so that a semiconductor is inherently an insulator. If the material absorbs energy in the form of light or heat, the now mobile electrons in the CB and associated holes in the VB lead to the material becoming conductive. Upon thermal or light induced excitation to the excited state bands, the excitation-induced population of electrons and holes in the CB and VB must be the same. As a result, the Fermi level of intrinsic semiconductors is in the middle of the bandgap and the thermal population of electrons in the CB follows fermi-dirac statistics. Photovoltaic devices rely on the transfer of the energy in light to the electrons in the semiconductor, generating mobile charges in the CB and VB. If the electrons and holes can be collected at opposite electrodes, a photocurrent is generated.

Since semiconductors are generally insulating in the absence of some excitation, they are not generally useful for electronics. Electrons and holes can, however, be added to the CB and VB, respectively, by selective n or p-type doping. The case of an n-doped semiconductor is depicted in Figure 2.1. Here, a new component with electronic states just shallow of the CB of the host material is incorporated at a low concentration, and the thermally ionized electrons populate the CB, raising the Fermi level to be near the CB[1]. The high population of mobile charges in doped semiconductors means that the materials support an electrical current upon application of an electric field; they have become conductive. The conductivity (σ) of the material is directly related to the number of mobile charges

and their mobility (μ_n and μ_p for electron and hole mobilities respectively) by the simple relation

$$\sigma = q\{(N_D + n)\mu_n + (N_A + p)\mu_p\} \quad (2.1.1)$$

where N_D and N_A are the electron and hole doping densities respectively, n and p are the thermal or photo-induced electron and hole populations, respectively, and q is the elementary charge. Silicon, the most commonly employed inorganic semiconductor, is often n-doped by addition of group V elements such as phosphorous which can donate a valence electron. It is p-doped by group III elements such as Boron which are electron deficient in the lattice[1].

Similar to inorganic crystalline semiconductors, the relatively strong covalent bonds that hold organic molecules together ensure that a large quantum of energy is required to excite an electron. Aromatic organic molecules consist of alternating double and single bonds (termed conjugation), forming molecular π orbitals by overlap of parallel p_Z atomic orbitals. This is depicted in Figure 2.2 for the simplest conjugated organic polymer: polyacetylene. Here, the electron cloud is delocalized

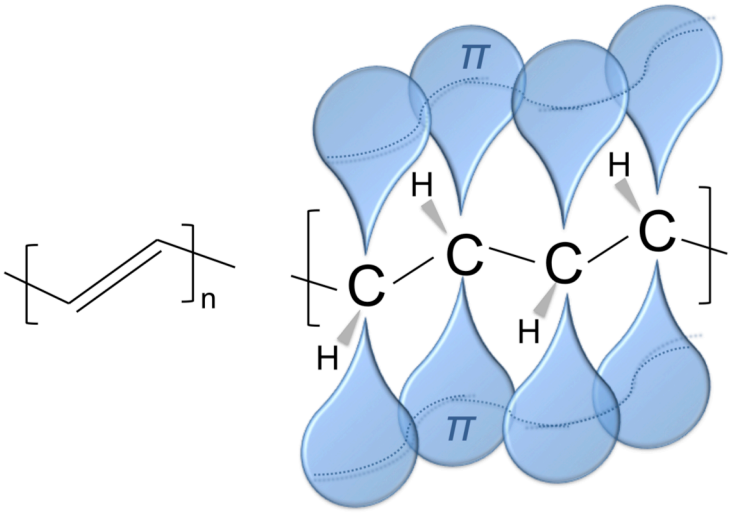

Figure 2.2. The trans-polyacetylene monomer is depicted on the left, while the right illustration demonstrates the overlap of atomic p orbitals, forming delocalized π bonds.

throughout the molecular π orbital, similar to what happens in the electronic bands in inorganic crystalline semiconductors. Strong phonon coupling in organics results in the formation of polarons, so that the delocalization only extends for several monomers in conjugated polymers, and in the case of small molecules naturally only extends to delocalization within the molecule[3–5]. As such, long-range delocalization in energetic bands is not possible in organic semiconductors. Instead, excited electrons and holes reside in the Lowest Occupied and Highest Unoccupied Molecular Orbitals (LUMO and HOMO), respectively. These are also referred to as the groundstate bonding (π) and excited state anti-bonding (π^*) molecular orbitals and the forbidden energy gap between them arises just as does the bandgap in inorganic semiconductors.

The lack of complete long-range delocalization of the electron wavefunction affects charge carrier transport in organic semiconductors. Here, charges cannot be considered as free, as they are directly related to an oxidized (holes) or reduced (electrons) state of the molecule or polymer fragment. To move through a matrix of small molecules, charge must "hop" from the molecular orbital of one molecule to the next, a process that requires an activation energy. The situation is similar in conjugated polymers because the delocalization does not extend uniformly along the entirety of the polymer chain, and certainly not between different chains, so that charge must navigate a varied energetic landscape[3–5]. As a result, the charge carrier mobility in organic semiconductors (< 10 $cm^2\ V^{-1}\ s^{-1}$)[6] tends to be significantly lower than in inorganic crystalline semiconductors (> 1000 $cm^2\ V^{-1}\ s^{-1}$)[7] and depends strongly on processing conditions and film formation.

Charge transport in systems with low electronic coupling between states can be described by Marcus theory.[5,8] Here, changes in Gibbs free energy (ΔG^0) as well as conformational changes must be considered. The charged and neutral states of the organic semiconductors have differing conformations, so that the intramolecular reorganization energy involved in going from one to the other is non negligible. The same is true for intermolecular interactions, where the interaction between a charged and neutral molecule is different than between two neutral molecules. Hence, a reorganization energy (λ_R) must be considered to predict the likelihood for charge transfer. For charge transfer to occur, the wavefunction overlap between the

two states must be minimized; ie vibrational coupling of the acceptor molecule to a geometry more similar to the donor geometry may be required if λ_R is large. Since the probability of charge transfer then depends not just on the change in Gibb's free energy, but also on λ_R and the available thermal (vibrational) energy, the electron transfer rate (k_{ET}) can be expressed via a modified Arrhenius expression as

$$k_{ET} = Ae^{-\frac{(\lambda_R+\Delta G^0)^2}{4\lambda K_B T}} \qquad (2.1.2)$$

where A and λ are factors related to the electronic coupling and reorganization energy of the system and K_B is the Boltzmann constant[5,9]. The rate of charge transfer is directly proportional to the charge carrier mobility in these systems. When considering charge transport within an organic semiconductor film, $\Delta G^0 = 0$, so that only the reorganization energy is important. The above expression makes it evident that charge transport in such materials must be highly temperature dependent, since a large enough thermal energy must be provided to allow charge transfer between states[5,9,10].

2.2

Principles of Photovoltaic Devices

The processes of power generation in photovoltaic devices can be split into three fundamental steps, as listed below.

1. Light absorption and excited state generation
2. Charge separation
3. Charge collection

The bandgap, described in Section 2.1, dictates light absorption in all semiconductors. Only light with energy equal to, or greater than, the bandgap can be absorbed to excite an electron from the groundstate to the CB (or LUMO in organic

semiconductors) and leave a hole in the VB (or HOMO in organic semiconductors). Hence, the absorption onset, or lowest energy of light absorbed, of a semiconductor is equal in energy to the bandgap. This is depicted in Figure 2.3, where we show the overlap of the solar irradiation incident upon the earth and the absorption onsets for three classes of materials used in photovoltaic devices. Specifically, the onsets are provided for the commonly used semiconductor silicon,[11] an organic indolene dye used in this study (termed D102),[12] and a hybrid organic-inorganic semiconductor $CH_3NH_3PbI_{3-x}Cl_x$ (the "x" is still under investigation) of the perovskite crystal structure (henceforth simply termed "perovskite")[13]. In terms of light absorption, the ideal is naturally to absorb all the sunlight in the solar spectrum. This would, however, require an infinitesimally small bandgap, so that the energy gained by photo-excited electrons would be infinitessimily small. Hence, there is a trade-off in terms of the total number of excited electrons that can be generated (related directly to the photo-current in a photovoltaic device) and their potential energy, (related to the photo-voltage of the device and the electrical potential at which these electrons are extracted and used to do work). It is possible to demonstrate, as did Shockley and Queisser[14], that the ideal bandgap for photovoltaic power conversion, assuming low energetic losses, is between 1.1 and 1.5 eV. It is evident from Figure 2.3 that silicon has an ideal bandgap, the perovskite is slightly blue-shifted from the ideal absorption onset, whereas the D102 dye is far from ideal.

Knowledge of the bandgap only is not enough to predict the fraction of photons absorbed by a material under solar illumination. It is also important to know the absorption coefficient of a material at a given energy of light. The prerequisite for light to be absorbed is that the photons have a higher energy than the bandgap. Optical transitions can, however, have differing probabilities of occurring, depending on the transition's oscillator strength, related to the transition dipole moment. This is also wavelength dependent and determines the absorption (or light extinction) coefficient at a given wavelength. The amount of incoming light that is absorbed is often referred to as the optical density (O.D.) of a material at a given wavelength. The O.D. is defined by

$$O.D. = -\log\left(\frac{I}{I_0}\right) \quad (2.2.1)$$

Where I and I_0 are the transmitted and incident light hitting the material, respectively. The O.D. is related to the concentration of absorbing species (C), the light path length (d) through the material, and its extinction coefficient (ε_A) by Beer Lambert's law:

$$\frac{I}{I_0} = 10^{-O.D.} = 10^{-Cd\varepsilon_A} \quad (2.2.2)$$

In solid films, this can be simplified by defining an extinction coefficient in terms of the film thickness rather than the concentration, and the absorption of a film is directly related to the film thickness. Once one knows the full absorption spectrum of an absorber, it is possible to estimate the maximum attainable (ignoring

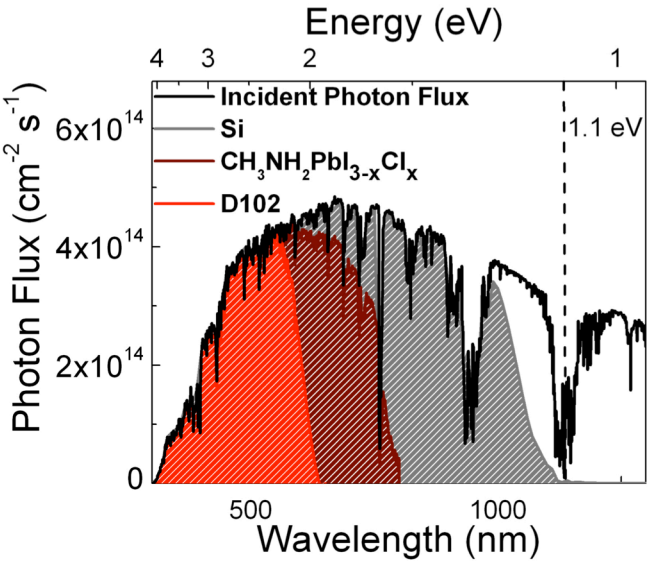

	Photocurrent (mA cm-2)
Si	41
$CH_3NH_3PbI_{3-x}Cl_x$	23
D102	13

Figure 2.3. The incident photon flux at AM 1.5 illumination is depicted along with the absorbed photon fluxes for Si, $CH_3NH_2PbI_{1-X}Cl_X$ perovskite, and D102 absorbers in commonly employed architectures. Optical path lengths of 150 µm, 500 nm, and 1.5 µm were considered for Si, $CH_3NH_2PbI_{1-X}Cl_X$ perovskite, and D102 respectively. The table on the right depicts the maximum photocurrent that could be generated for the different absorbers assuming 100 % charge generation and collection efficiencies.

reflections, and assuming perfect dissociation and collection of photo-excitations) photocurrent of the corresponding solar cells under standard solar illumination at air mass 1.5 (AM1.5). Using the O.D. of the film of material used in the solar cell, one can integrate the number of photons collected per second over the entirety of the solar spectrum to yield the maximum possible coulombs of collected charge as the photocurrent (mA cm^{-2}) of the solar cell. This analysis is presented in Figure 2.3 for the organic indolene dye D102, the organometal trihalide perovskite used in this study, and the standard photovoltaic absorber Si, and demonstrates the importance of being able to extend the absorption of the solar cell into the near infra red (NIR) region of the solar spectrum.

Once electrons are photo-excited, they remain coulombically attracted to the corresponding hole. Such a correlated electron-hole pair is termed an exciton, and can have varying binding strength and delocalization range depending on the material of interest. The binding energy of an excitonic species is predominantly determined by the dielectric constant of the material, where higher dielectric constants mean that the electric field between negative and positive poles of the exciton is more effectively "screened" by the material. Such correlated species must be separated so that electrons and holes can move independently and a photocurrent can flow in a photovoltaic device[15–18]. The excitonic species can be separated by provision of energy greater than its binding energy such as an electric field, heat, or by charge transfer to a lower lying separated state across an interface with another material[15–18]. This charge separation step imposes a limit on the photovoltage that can be obtained for a given absorber, and energy cascade systems are often employed to drive charge separation at the cost of photovoltage[19–21]. Organic absorbers such as polymers and dyes used in solution processed photovoltaic devices typically have low dielectric constants (~ 3) and exhibit high binding energies (> 100 mev),[2,22] such that photo-generated species tend to exist as excitons at room temperature in the absence of an electric field or interface interactions. Inorganic crystalline absorbers such as Si or GaAs have high dielectric constants and hence only free charges tend to exist at room temperature[23,24].

As a result, the optimum photovoltaic device architectures are very different for these two classes of materials. Organic absorbers tend to benefit from

architectures composed of two or more interconnected components with high interfacial surface areas to facilitate exciton dissociation, and where holes and electrons will reside in the donor and acceptor species respectively. The resulting populations of holes and electrons, being spatially separated and in different materials, then also benefit from increased lifetimes (> 100s ns) as compared to the excitonic species itself (< 1ns)[22,25].

Once separated, electrons and holes must be collected at appropriate contacts to actually generate a photocurrent. Charge carriers move through a combination of drift and diffusion currents as expressed below[2].

$$J_l = q(n\mu_n + p\mu_p)E + q(D_n \frac{dn}{dx} + D_p \frac{dp}{dx}) \quad (2.2.3)$$

Here, J_l is the photocurrent, E is the electric field across the material in the direction of current flow, D is the diffusion constant, n and p are the photo-generated electron and hole concentrations, and x is the position along the direction of current flow. D can be related to the carrier mobility (μ) by the Einstein relation, which says that

$$D = \mu K_B T \quad (2.2.4)$$

where T is the temperature and K_B is Boltzmann's constant. Si and GaAs photovoltaic devices generally rely on drift current to collect the charge and are engineered so that large internal fields helps to drive charge, whereas photovoltaic devices incorporating ionic additives and high dielectric constant materials will be dominated by diffusion effects[2,26,27]. Here, it is essential to use selective contacts, so that only electrons are transferred to the contact at the anode, and only holes at the cathode. If the charge transfer rate at the contact interface is faster than the charges can move (as is generally the case in successful solar cell architectures), the density of carriers at the interface with the contact can be considered as 0. A gradient in

charge density must then exist in opposite directions for electrons and holes, leading to effective diffusion of carriers to the selective contacts[2,28,29]. If charge extraction is the only way of removing photo-generated carriers from the device, then the photocurrent will be independent of the carrier mobility: a low mobility will result in a build up of *n* and *p* and eq. 2.2.3 shows that both drift and the diffusion currents will remain unchanged.

One must also consider, however, that the photo-generated species do not have infinite lifetimes, so that there are several competing pathways that limit the photocurrent in real photovoltaic devices. Indeed, the primary loss pathway in photovoltaic devices is simply recombination of CB electrons and VB holes, and this can occur within the absorber, across the interface between a donor and acceptor material, or even at the contacts. Here, the photo-excitation is lost as heat or light (in a process termed photoluminescence), returning the absorber to its initial ground state.

Solution processed materials, while cheaper, do suffer from the fact that film formation and crystallization is relatively poorly controlled, leading to defects in crystal structure[20,30–32]. These often take the form of vacancies, dislocations, and grain boundaries. They can also form at the interface between two materials such as the electrical contact in a photovoltaic device. Such defects result in the formation of a low energy state within the forbidden gap of the semiconductor, termed a trap state. Because the defects are linked to local changes in crystal structure or molecular packing, these states are localized. Electrons in the CB are readily trapped in such electron traps, and holes are trapped in hole traps. Shallowly trapped carriers can still be thermally excited out of the trap states, but such a trapping – detrapping mechanism tends to heavily limit the effective carrier mobility and is heavily temperature and charge density dependent[10,32–34]. Deeply trapped carriers cannot be thermally detrapped and are effectively immobilized. Such trapping processes, by limiting the rate at which carriers can be extracted, favour the recombination loss pathways, and heavily influence the attainable photocurrents in photovoltaic devices[2,35].

The events that contribute to photocurrent extraction from a photovoltaic device are depicted in Figure 2.4a for the case of a Si solar cell[2]. Such devices benefit from a built-in field to aid rapid charge extraction. This is accomplished by contacting *n*-doped and *p*-doped pieces of Si wafer in a planar heterojunction. Since the two pieces have high densities of free carriers of the opposite polarity, they will diffuse to the interface between the materials and recombine to match the Fermi levels in the materials at the interface. As the carriers from the two wafers recombine, they leave behind ionized dopant atoms. This leads to the formation of a

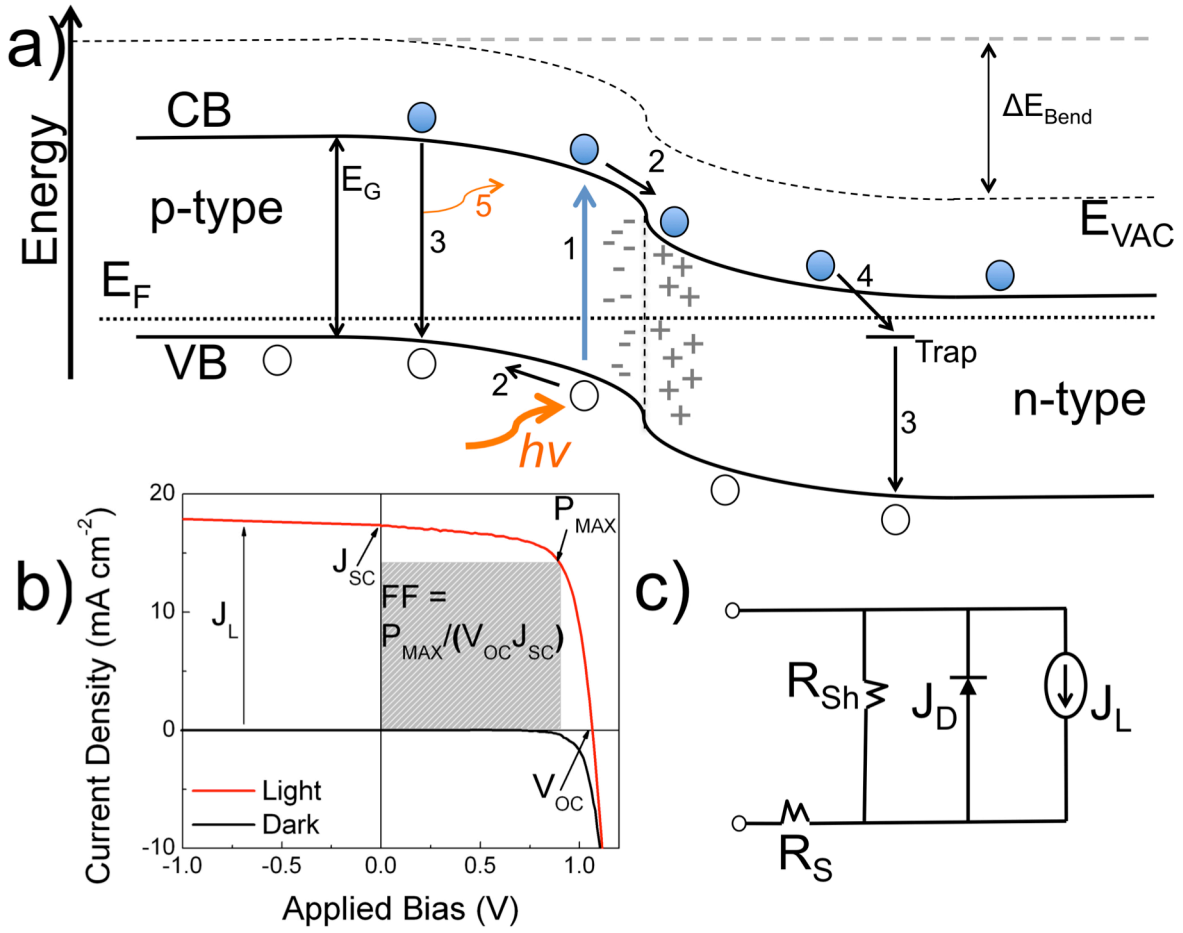

Figure 2.4. (a) Schematic representation of an Si p-n junction photovoltaic device. The Energy bands are bending because the doping densities in the two materials have generated a depletion region with an associated built-in field (ΔE_{Bend}). The most important steps that contribute to solar cell operation are also enumerated: (1) light absorption and charge generation, (2) drift of electrons and holes towards their respective electrons, (3) recombination of electrons and holes which may be followed by light emission (5), and (4) charge trapping followed by (3). (b) Shows representative dark and light J-V curves, which are offset by the photo-induced current (J_L). The figures of merit are also pointed out. (c) Equivalent circuit of a photovoltaic device. This consists of a photocurrent source (J_L) in parallel with a diode as described by the ideal diode equation. R_{SH} represents a shunt resistance (also in parallel), which should be high to minimize leakage current, while R_S is the series resistance of the device, which should be low to maximize the FF of the device.

depletion region, where all the doping induced free carriers have recombined, and which is half positively (*n*-type side of the junction) and half negatively (*p*-type side of the junction) charged. The depletion region will continue to grow until the electric field from the charged interfacial regions prevents diffusion of more free carriers. Hence, the doping density determines the magnitude and depth of the built-in field in such devices, which are termed diodes.

Upon photo-generation of excess free charge, electrons are rapidly swept "downhill" in energy towards the *n*-type layer and holes are swept the opposite direction. To stop current from flowing, an electric field equal and opposite to the built-in field must be externally applied. This is known as the open circuit voltage of the device, and is determined by the offset in quasi Fermi levels of electrons and holes. Application of the reverse field injects carriers into the device in the opposite direction from that used to do work, and these carriers must recombine at the *p*-*n* junction. Such reverse, or dark, current is present in all photovoltaic devices at any electrical bias, and is minimized by choice of selective contacts and by removing recombination pathways. The dark current density in such diodes can be described by the ideal diode equation:

$$J = J_S(e^{\frac{qV_A}{K_BT}} - 1) \qquad (2.2.5)$$

where V_A is the bias applied across the contacts and J_S is a prefactor related to the recombination dynamics, which will change for any given system.

Upon photo-excitation, the current density – voltage (J-V) relationship will take on a form very similar to that described by eq. 2.2.5, but with a constant offset due to the photocurrent. Figure 2.4b plots representative dark and light J-V curves for photodiodes such as those that make up Si photovoltaic devices. This sort of diode structure and the importance of the built-in field is not directly applicable to the operation of SSCs, where ionic additives, high dielectric constants of some of the materials, and complex architectures result in the devices being diffusion mediated[36]. Since the ideal diode model primarily describes recombination currents as a function

of bias, the J-V characteristics of SSCs can still be roughly modelled by an adapted ideal diode equation, where an ideality factor is included in the exponential term primarily to accommodate the differences in recombination mechanisms. In an ideal solar cell, the J-V curve would be almost square in shape, where the current density is constant until the open circuit voltage is reached. In reality, series resistance and recombination losses begin to limit the current as the applied bias increases. Hence, the J-V curve no longer follows the ideal diode equation, and can be more accurately modelled by the equivalent circuit in Figure 2.4c, where a diode is placed in parallel with a (photo-generated) current source and a shunt resistor (representing leakage current), with a resistor in series to represent resistive losses[2,37]. The leakage current is different from the recombination current described by the ideal diode equation, and is due to factors such as pinholes, poor selective contacts, and other issues with the device architecture rather than inherent properties of the semiconductors used.

Figure 2.4b highlights the merit parameters used to quantify photovoltaic device performance: the short circuit current (J_{SC}), the open circuit voltage (V_{OC}), the fill factor (*FF*), and finally the power conversion efficiency (*PCE* or η). The J_{SC} is the current extracted from the device when no external field is applied, and should be the same as the photocurrent described above. The maximum power point is determined at the point where the product of J and V is maximized, and the *PCE* is then the ratio of the power produced at the maximum power point (P_{MPP}) with the incident light irradiance (P_{Inc}) .

$$PCE = \frac{P_{MPP}}{P_{Inc}} \tag{2.2.6}$$

The ratio of the *PCE* and the theoretically ideal performance $J_{SC} \times V_{OC}$ is defined as the *FF*.

$$FF = \frac{PCE}{J_{SC} \times V_{OC}} \tag{2.2.7}$$

Depending on the solar cell architecture, the FF will be limited by inherent recombination dynamics, low shunt resistances, or high series resistances and gives an idea of how close the photovoltaic device is functioning to the ideal.

2.3

Principles of Solid-State Sensitized Solar Cell Operation

SSCs, developed in their current form by O'Regan and Grätzel in 1991[21], can be described by the three basic operating principles of photovoltaic devices of light absorption, charge separation, and charge collection. In traditional SSCs, however, these steps are all performed by material components specifically designed to perform just one of the functions. In a standard SSC, a solution processed inorganic semiconductor such as TiO_2 acts as electron acceptor and transporter. TiO_2 is chosen because of its suitable electron mobility and CB energy level. TiO_2, however, with a bandgap of 3.2 eV, cannot absorb visible light, limiting the photocurrent that could be obtained by this material alone. To extend the light absorption of the composite, the TiO_2 is sensitized by a light absorbing pigment such as a dye or solution processed inorganic absorber[38–40]. Upon light absorption, the electron in the sensitizer's

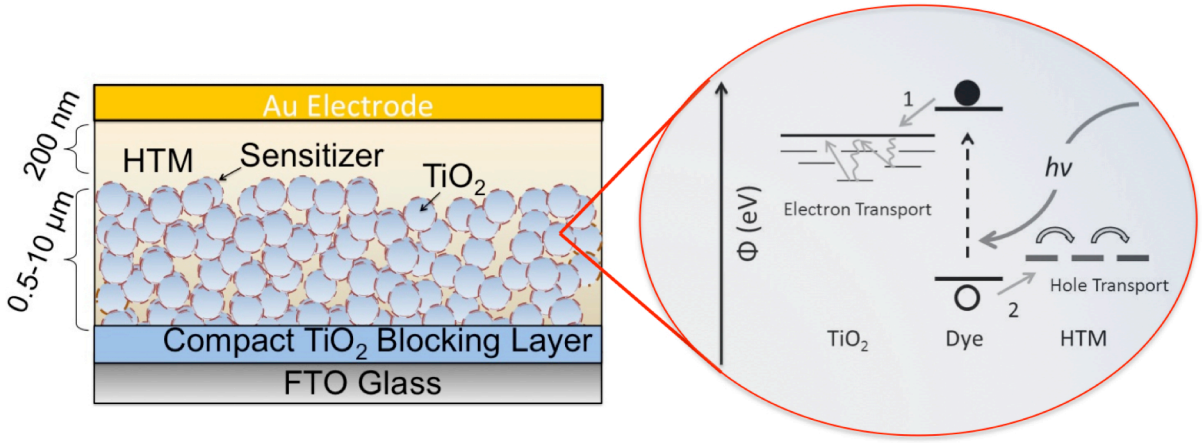

Figure 2.5. Schematic of a SSC. Fluorine-doped Tin Oxide (FTO) is the bottom, electron-collecting electrode, and this has been made electron selective by deposition of a compact TiO_2 layer (approx. 50 nm). The mesoporous TiO_2 layer can range from 0.5 – 10 µm in thickness, depending on the absorption strength of the sensitizer, and whether a liquid (towards thicker devices) or solid state (thinner devices) HTM is employed. A capping layer of HTM of 200 nm is typical for solid state SSCs, while it is common for several µm of HTM to separate the mesoporous TiO_2 layer from the cathode in SSCs utilizing liquid electrolytes. A diagram depicting the events following light absorption in a SSC employing a solid state HTM is displayed on the right: (1) the excited electron is injected into the TiO_2 CB in less than 1 ps, where it is transported towards the anode via a trap limited diffusion mechanism, as described in Section 2.3.2. The hole (2) is transferred to the HTM within 1 ns and is transported towards the cathode via the hopping mechanism described in Section 2.1 and 2.3.3.

excited state can be transferred to the CB of the TiO_2. The dye is regenerated by a hole transport material (HTM) in the form of a liquid electrolyte redox electrolyte or a solid state semiconductor[21,41].

One disadvantage of this system is that typically only a monolayer of pigment can be employed as the light absorber while still ensuring efficient charge separation at the TiO_2 and HTM interfaces, limiting the O.D. of the system in planar configuration. The introduction of a mesoporous TiO_2 layer composed of a network of 25 nm nanoparticles with 25 nm pore size allowed for the effective surface area for pigment sensitization to be increased 100-fold[42]. This provided the breakthrough necessary for SSCs to become competitive in terms of PCEs. Figure 2.5 depicts a schematic for a standard dye sensitized solar cell (DSSC), where the HTM layer can be either a liquid redox couple such as the Iodide/tri-Iodide redox couple ($3I^- \leftrightarrow I_3^-$), or a solid organic HTM such as Spiro-MeOTAD. The compact TiO_2 layer at the anode minimizes leakage current between the HTM and FTO anode. The schematic also depicts the steps of light absorption, electron transfer, hole regeneration and charge transport pathways, that will be discussed in more detail in the subsequent sections. DSSCs employing liquid electrolytes such as the $3I^- \leftrightarrow I_3^-$ redox couple or the $Co^{(II/III)}$tris(bipyridyl)–based redox couple[43] have reached impressive *PCE*s over 12 %, but suffer from the fact that the electrolytes tend to be corrosive and the devices susceptible to leakage. More fundamentally, the overpotential required to drive the redox couples limits the maximum attainable photovoltages of the devices[44]. Solid state HTMs based on small organic molecules such as Spiro-MeOTAD seek to resolve these issues, and should allow for higher photovoltages and hence *PCE*s to be attained[44]. For this reason, this work focuses solely on solid-state SSCs (ssSSCs) from this point onwards.

2.3.1
Charge Generation

Light absorption in the sensitizing dye promotes electrons to the dye excited state. From there, they can either decay back to the ground state, or undergo charge

transfer at the TiO_2 interface. Photoluminescence and transient absorption studies have demonstrated that while the excited state lifetime of commonly used dyes tends to be on the order of 10s of ns, the electron transfer (or injection) to TiO_2 occurs on the time scale of 1 ps, meaning that there are negligible losses at this charge separation step[45]. Following electron transfer, the dye is regenerated on the time scale of 100s of ps by the Spiro-MeOTAD HTM[46], rapidly outcompeting recombination with electrons in TiO_2 (μs –ms timescale). The result is that absorbed photons induce a build up of electrons in the mesoporous TiO_2 layer and of holes in the HTM with near 100 % efficiency.

For electron and hole transfer to occur so efficiently, however, the sensitizers are designed such that the energetic offsets between the LUMO level and the TiO_2 CB as well as the HOMO level and HTM oxidation potential provide large driving forces of around 300 and 100-200 meV respectively. This limits the maximum attainable photovoltage of the DSSCs to well below the bandgap of the absorber itself, such that photovoltaic devices of this type are inherently incapable of approaching the Shockley-Queisser limit. In addition to this, ionic additives such as Li-TFSI are added to the system[47], decreasing the surface potential of TiO_2 by lithium ion intercalation at the surface. This leads to increased electron transfer rates, but at the cost of lower photovoltages. The effects of additives such as Li-TFSI will be described in full in Chapter 4.

2.3.2
Electron Collection in the Mesoporous TiO_2 Anode

Once the electrons and holes have been successfully separated, electrons in the TiO_2 must be collected at the anode, while holes in the HTM must be collected at the cathode. The disordered nature of the TiO_2 nanoparticle network, the high dielectric constant of TiO_2, and the large amount of ionic additives in the HTM, mean that any built-in field due to an offset in the electrode workfunctions has little effect

on charge collection in SSCs[26,36,48]. Instead, charges must diffuse to the appropriate contact, as discussed in Section 2.2 and Eq 2.2.3.

As described in Section 2.2, solution processed semiconductors such as the mesoporous TiO_2 nanoparticle network employed in SSCSs exhibit very large trap densities. In mesoporous TiO_2, these are electron traps, varying in energy from 1 eV to just below the CB, and are primarily due to surface defects such as oxygen vacancies, grain boundaries, and poor electronic contact between nanoparticles[27,36,49]. The result is that the density of electronic states in the TiO_2 deviates far from that of an ideal semiconductor, and is dominated by an exponential tail of sub gap states[50]. This is depicted in Figure 2.6, for a working device, where the V_{OC} (directly related to the electron quasi Fermi level, and hence level of trap filling in the TiO_2) is plotted against the capacitance, which is directly related to the density of states (DOS)[51]. Details for how such measurements are made are presented in Chapter 3. The influence of a distribution of shallow traps on charge carrier mobility has already been described in Section 2.2, and makes it clear that the high density of sub gap states must limit electron diffusion in SSCs. In fact, the effective electron mobility in these mesoporous films has been demonstrated to be as low as 10^{-5} cm^2 V^{-1} s^{-1} [42,52]at low charge densities, several orders of magnitude lower than the mobility in bulk crystalline TiO_2 of 10 cm^2 V^{-1} s^{-1} [53,54].

In the photovoltaic device, diffusion is limited by detrapping events with probability (P) related to the depth of the trap (E_Δ) relative to the CB energy, so that

$$P(E) \propto e^{-\frac{E_\Delta}{K_B T}} \qquad (2.2.8)$$

As a result, electrons in deeper traps will be detrapped less frequently, and will spend less of their lifetime as mobile charges in the CB. Hence, the electron mobility in TiO_2 is heavily dependent on the electron density. In particular, as excitation intensity increases, deeper sub gap states are progressively filled, raising the quasi Fermi level for electrons, so that a high fraction of the photogenerated charge can be

rapidly detrapped from relatively shallow sites[27,31,55]. This raises both the effective mobility and the steady state population of non-trapped electrons (CB electrons). The influence of such traps on electron injection, recombination pathways, and charge density dependent electron transport will be an important topic throughout this thesis.

2.3.3
Hole Hopping in the HTM

The use of solid state HTMs should allow for more stable SSCs while also minimizing the loss in potential. Still, ssSSCs using sensitizing dyes have fallen short of their promise, never approaching the *PCE*s (7.2 vs 12.3 %) of their liquid electrolyte counterpart[43,56]. One of the primary differences between the liquid electrolytes and solid state HTMs is that ionic screening slows the electron (in TiO_2) and hole (in HTM) recombination in liquid electrolytes[57,58]. While the LiTFSI additive used in ssSSCs provides some screening, the recombination dynamics in ssSSCs tend to be several orders of magnitude faster (0.1 – 1 ms) than in SSCs with liquid electrolytes (10-100s ms)[57,58]. As a result, rapid charge transport becomes essential to ensure that charge is collected before it can recombine. The low hole mobility of small molecule HTMs such as Spiro-MeOTAD (structure in Figure 2.7) has often been touted as the reason for the poor performance of ssSSCs[41,59,60].

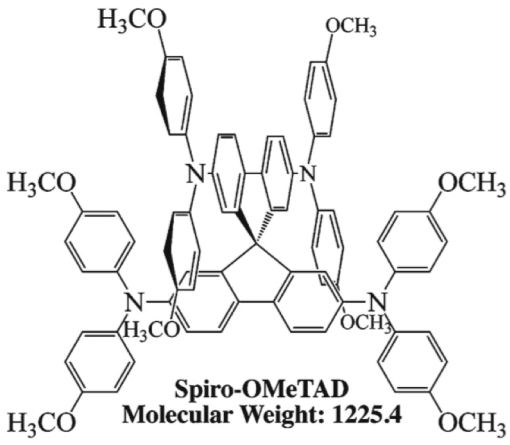

Figure 2.7. Chemical tructure of the commonly employed HTM Spiro-MeOTAD. Chemical name: 2,2',7,7'-tetrakis(N,N-di-*p*-methoxypheny-amine)-9,9'-spirobifluorene. This HTM will be employed for all studies in this thesis.

As discussed in Section 2.1, hole mobilities in films of small molecule HTMs are inherently low because the HOMO is delocalized within a single molecule only. Hole mobilities as low as 10^{-5} cm^2 V^{-1} s^{-1} [61] have reported for Spiro-MeOTAD, and this has sparked a debate about hole transport limiting device performance. It was proposed that such a low mobility limits the charge diffusion length and hence photocurrent in solar cells[62]. As a result, a great deal of research effort has focused on the development of high mobility HTMs ($>10^{-3}$ cm^2 V^{-1} s^{-1})[62–69]. Polymers have been considered to be especially promising due to their superior hole mobilities; notable examples include in-situ polymerized PEDOT, P3HT or PCPDTBT[64,65,67]. Still, the "low mobility" Spiro-MeOTAD has remained the gold standard in ssDSSCs. Indeed, by varying the molecular structure and associated hole mobilities of a range of HTMs, Kroeze *et al*. demonstrated that the hole mobility of the HTM has little effect on the short circuit photocurrent of the solar cells when the widely employed *t*bp and Li-TFSI additives were used[62]. Indeed, the addition of Li-TFSI was shown to dramatically improve the conductivity of Spiro-MeOTAD, which was proposed to be due to a smoothing of the potential landscape[70]. Snaith *et al*. also compared the conductivities of Spiro-MeOTAD and TiO_2 in ssSSCs in-situ, and suggested that the hole conduction in an operational dye sensitized solar cell is significantly faster than electron conduction through the TiO_2[71]. Chapter 4 of this thesis explores the role of LiTFSI on solar cell performance and hole transport in particular. Chapter 5, by use of a novel technique, then explores and fully resolves the role of hole transport through HTMs in ssSSCs and how it affects the balanced charge collection of working devices.

2.3.4
Thickness Limitation

One of the primary drawbacks of ssSSCs is that the optimized device thickness is only ~ 2 μm, far less than the absorption depth even when using dye sensitizers with high extinction coefficients[69,72,73]. The attainable photocurrents are then far

lower than in the liquid electrolyte counterpart, where thicknesses over ~ 10 μm are easily achieved. The inability to make thicker ssSSCs has been ascribed to poor pore filling of the HTM inside the pores, preventing efficient charge transfer and collection[69,72–75]. Recent work, however, has demonstrated that high pore filling fractions can be achieved for devices up to 5 μm thick, suggesting that this cannot be the limiting factor[76]. Still, increasing the device thickness does not result in increases in photocurrent.

Another common explanation is that slow hole transport limits the diffusion length in thicker devices to less than 5 μm. Snaith et. al. have however demonstrated this not to be the case, reporting diffusion lengths of over 15 μm[72]. By studying the charge transport and p-doping characteristics of the HTM in Chapters 4 and 5, this thesis will present new insight into the thickness limitations based on the requirement for HTM doping and an associated parasitic absorption.

A very simple solution is of course to use a higher extinction coefficient sensitizer. Such a sensitizer has recently emerged in the form of an organometal trihalde perovskite, $CH_3NH_3PbI_{3-x}Cl_x$[13,40,77]. This material, with a wide absorption spectrum, is capable of generating high photocurrents in devices thinner than 1 μm[77], so that the thickness limitation has essentially been resolved for this class of photovoltaic devices. Chapter 7 discusses the mechanisms of charge transport and recombination in ssSSCs devices based on this perovskite absorber and how these are dependent on the fraction of perovskite filling the TiO_2 mesopores.

2.4

SSC Stability

While competitive *PCE*s are starting to be reached, it will ultimately be the stability, i.e. the lifetime under operation, that will determine whether these device platforms are just interesting photovoltaic concepts or viable technologies. Solar cell stability is a measure of whether a given technology can withstand long-term exposure to the conditions relevant to solar cell use, such as high illumination, temperature, or humidity exposure. This is essential to ensure that the solar panels

will be functional long enough to offset their financial and energetic investment costs. Indeed, lifetimes of over 25 years have become the industry standard for currently commercial photovoltaic panels.

In order to achieve sufficient stability to withstand 25 years under illumination, sensitizers must be able to complete over 10^8 turnovers before decomposing[78]. This is in principle realistic for ruthenium-based dyes, as determined by spectroscopic studies[45], because ultrafast electron injection out-competes degradation mechanisms. In terms of full device stability, SSCs employing the Iodide/tri-Iodide redox couple have exhibited stable performances for over 1000 hours, while stable photocurrents were observed for 10,000 hours by choosing hydrophobic dyes, and excluding water from the electrolyte[79,80].

Surprisingly, very little has been published on the long-term stability of ssSSCs, despite the fact that they have been lauded as a fundamentally more stable technology than SSCs employing liquid redox electrolytes. In the few studies that do mention long-term stability, factors such as ultraviolet light (UV) exposure, type of encapsulation, and continuous versus intermittent solar irradiation are often not clearly described, even though they can have profound effects on the stability of solar cells employing solid-state hole transporters[56,77,81–83]. UV cut-off filters are often employed, but the exact nature of the effect of UV light on solar cell stability is not yet well understood. Atmospheric interactions of the mesoporous TiO_2 anode with under illumination has remained largely unstudied, despite the fact that TiO_2 is known to be an effective photo-catalyst through its interaction with the atmosphere[84–86]. This occurs via surface defects, which are known to play an important role in charge trapping and recombination in ssSSCs[37,50]. Chapter 6 of this thesis deals with degradation mechanisms that dominate upon the first several hours of illumination, placing particular importance on the influence of UV light on the stability of the mesoporous TiO_2 anode.

2.5 References

(1) Sze, S. M. *Semiconductor Devices: Physics and Technology*; 2006; p. 568.

(2) Nelson, J. *The Physics of Solar Cells*; 2004; Vol. 57, p. 384.

(3) Burroughes, J. H.; Bradley, D. D. C.; Brown, A. R.; Marks, R. N.; Mackay, K.; Friend, R. H.; Burns, P. L.; Holmes, A. B. Light-emitting diodes based on conjugated polymers. *Nature*, 1990, *347*, 539–541.

(4) Clarke, T. M.; Durrant, J. R. *Chem. Rev.* **2010**, *110*, 6736.

(5) Coropceanu, V.; Cornil, J.; da Silva Filho, D. A.; Olivier, Y.; Silbey, R.; Brédas, J.-L. *Chem. Rev.* **2007**, *107*, 926.

(6) Holliday, S.; Donaghey, J. E.; McCulloch, I. *Chem. Mater.* **2013**, *26*, 647.

(7) Sze, S. M.; Irvin, J. C. Resistivity, mobility and impurity levels in GaAs, Ge, and Si at 300°K. *Solid-State Electronics*, 1968, *11*, 599–602.

(8) Marcus, R. A. *Rev. Mod. Phys.* **1993**, *65*, 599.

(9) Brédas, J. L.; Calbert, J. P.; da Silva Filho, D. A.; Cornil, J. *Proc. Natl. Acad. Sci. U. S. A.* **2002**, *99*, 5804.

(10) Blom, P. W. M.; de Jong, M. J. M.; van Munster, M. G. *Phys. Rev. B* **1997**, *55*, R656.

(11) Green, M. A.; Emery, K.; Hishikawa, Y.; Warta, W.; Dunlop, E. D. *Prog. Photovoltaics Res. Appl.* **2012**, *20*, 12.

(12) Schmidt-Mende, L.; Bach, U.; Humphry-Baker, R.; Horiuchi, T.; Miura, H.; Ito, S.; Uchida, S.; Grätzel, M. *Adv. Mater.* **2005**, *17*, 813.

(13) Lee, M. M.; Teuscher, J.; Miyasaka, T.; Murakami, T. N.; Snaith, H. J. *Science (80-.).* **2012**, *338*, 643.

(14) Shockley, W.; Queisser, H. J. *J. Appl. Phys.* **1961**, *32*, 510.

(15) Mikhnenko, O. V.; Azimi, H.; Scharber, M.; Morana, M.; Blom, P. W. M.; Loi, M. A. Exciton diffusion length in narrow bandgap polymers. *Energy & Environmental Science*, 2012, *5*, 6960.

(16) Sebastian, L.; Weiser, G.; Bässler, H. *Chem. Phys.* **1981**, *61*, 125.

(17) Koch, S. W.; Kira, M.; Khitrova, G.; Gibbs, H. M. *Nat. Mater.* **2006**, *5*, 523.

(18) Terao, Y.; Sasabe, H.; Adachi, C. *Appl. Phys. Lett.* **2007**, *90*, 103515.

(19) Blom, P. W. M.; Mihailetchi, V. D.; Koster, L. J. A.; Markov, D. E. *Adv. Mater.* **2007**, *19*, 1551.

(20) Brabec, C. J.; Gowrisanker, S.; Halls, J. J. M.; Laird, D.; Jia, S.; Williams, S. P. *Adv. Mater.* **2010**, *22*, 3839.

(21) O'Regan, B.; Grätzel, M. *Nature* **1991**, *353*, 737.

(22) Brabec, C.; Dyakonov, V.; Scherf, U. *WILEY-VEH* **2008**, *ISBN 978-3*, 554.

(23) Aspnes, D. E.; Studna, A. A.; Kinsbron, E. *Phys. Rev. B* **1984**, *29*, 768.

(24) Blakemore, J. *J. Appl. Phys.* **1982**, *53*, R123.

(25) Hwang, I. W.; Moses, D.; Heeger, A. J. *J. Phys. Chem. C* **2008**, *112*, 4350.

(26) Bisquert, J. *J. Phys. Chem. B* **2004**, *108*, 2332.

(27) Van de Lagemaat, J.; Frank, A. J.; Lagemaat, J. Van De. *J. Phys. Chem. B* **2001**, *105*, 11194.

(28) Nelson, J. *Phys. Rev. B* **1999**, *59*, 15374.

(29) Snaith, H. J.; Gratzel, M. *Adv. Mater.* **2006**, *18*, 1910+.

(30) Sirringhaus, H. *Adv. Mater.* **2005**, *17*, 2411.

(31) Anta, J.; Nelson, J.; Quirke, N. Charge transport model for disordered materials: Application to sensitized TiO2. *Physical Review B*, 2002, *65*.

(32) Pasveer, W. F.; Cottaar, J.; Tanase, C.; Coehoorn, R.; Bobbert, P. A.; Blom, P. W. M.; De Leeuw, D. M.; Michels, M. A. J. *Phys. Rev. Lett.* **2005**, *94*, 206601.

(33) Tanase, C.; Meijer, E. J.; Blom, P. W. M.; de Leeuw, D. M. *Phys. Rev. Lett.* **2003**, *91*, 216601.

(34) Eppler, A. M.; Ballard, I. M.; Nelson, J. In *Physica E: Low-Dimensional Systems and Nanostructures*; 2002; Vol. 14, pp. 197–202.

(35) Bisquert A Salvador, P, J. Z. *J. Phys. Chem. B* **2002**, *106*, 8782.

(36) Bisquert, J. *J. Phys. Chem. C Lett.* **2007**, *111*, 17163.

(37) Fabregat-Santiago, F.; Bisquert, J.; Cevey, L.; Chen, P.; Wang, M.; Zakeeruddin, S. M.; Grätzel, M. *J. Am. Chem. Soc.* **2008**, *131*, 558.

(38) Nazeeruddin, M. K.; Péchy, P.; Renouard, T.; Zakeeruddin, S. M.; Humphry-Baker, R.; Comte, P.; Liska, P.; Cevey, L.; Costa, E.; Shklover, V.; Spiccia, L.; Deacon, G. B.; Bignozzi, C. A.; Grätzel, M. *J. Am. Chem. Soc.* **2001**, *123*, 1613.

(39) Im, S. H.; Lim, C. S.; Chang, J. A.; Lee, Y. H.; Maiti, N.; Kim, H. J.; Nazeeruddin, M. K.; Gr??tzel, M.; Seok, S. Il. *Nano Lett.* **2011**, *11*, 4789.

(40) Kojima, A.; Teshima, K.; Shirai, Y.; Miyasaka, T. *J. Am. Chem. Soc.* **2009**, *131*, 6050.

(41) Bach, U.; Lupo, D.; Comte, P.; Moser, J. E.; Weissortel, F.; Salbeck, J.; Spreitzer, H.; Grätzel, M. *Nature* **1998**, *395*, 583.

(42) O'Regan, B. C.; Lenzmann, F. *J. Phys. Chem. B* **2004**, *108*, 4342.

(43) Yella, A.; Lee, H.-W.; Tsao, H. N.; Yi, C.; Chandiran, A. K.; Nazeeruddin, M. K.; Diau, E. W.-G.; Yeh, C.-Y.; Zakeeruddin, S. M.; Grätzel, M. *Science (80-.).* **2011**, *334*, 629.

(44) Snaith, H. J. *Adv. Funct. Mater.* **2009**, NA.

(45) Tachibana, Y.; Moser, J. E.; Gratzel, M.; Klug, D. R.; Durrant, J. R. *J. Phys. Chem.* **1996**, *100*, 20056.

(46) Bach, U.; Tachibana, Y.; Moser, J.; Haque, S. A.; Durrant, J. R.; Grätzel, M. *J. Am. Chem. Soc.* **1999**, *121*, 7445.

(47) Kruger, J.; Plass, R.; Cevey, L.; Piccirelli, M.; Grätzel, M.; Bach, U. *Appl. Phys. Lett.* **2001**, *79*, 2085.

(48) Grätzel, M. *Inorg. Chem.* **2005**, *44*, 6841.

(49) Hagfeldt, A.; Boschloo, G.; Sun, L.; Kloo, L.; Pettersson, H. *Chem. Rev.* **2010**, *110*, 6595.

(50) Bisquert, J.; Zaban, a; Salvador, P. *J. Phys. Chem. B* **2002**, *106*, 8774.

(51) Docampo, P.; Guldin, S.; Stefik, M.; Tiwana, P.; Orilall, M. C.; Hüttner, S.; Sai, H.; Wiesner, U.; Steiner, U.; Snaith, H. J. *Adv. Funct. Mater.* **2010**, *20*, 1787.

(52) Petrozza, A.; Groves, C.; Snaith, H. J. *J. Am. Chem. Soc.* **2008**, *130*, 12912.

(53) Tiwana, P.; Docampo, P.; Johnston, M. B.; Snaith, H. J.; Herz, L. M. *ACS Nano* **2011**, *5*, 5158.

(54) Tiwana, P.; Parkinson, P.; Johnston, M. B.; Snaith, H. J.; Herz, L. M. *J. Phys. Chem. C* **2009**, *114*, 1365.

(55) Frank, A. J.; Kopidakis, N.; Lagemaat, J. Van De. Electrons in nanostructured TiO2 solar cells: Transport, recombination and photovoltaic properties. *Coordination Chemistry Reviews*, 2004, *248*, 1165–1179.

(56) Burschka, J.; Dualeh, A.; Kessler, F.; Baranoff, E.; Cevey-Ha, N.-L.; Yi, C.; Nazeeruddin, M. K.; Grätzel, M. *J. Am. Chem. Soc.* **2011**, *133*, 18042.

(57) Snaith, H. J.; Schmidt-Mende, L. *Adv. Mater.* **2007**, *19*, 3187.

(58) Hardin, B. E.; Snaith, H. J.; McGehee, M. D. *Nat. Photonics* **2012**, *6*, 162.

(59) Kroeze, J. E.; Hirata, N.; Schmidt-Mende, L.; Orizu, C.; Ogier, S. D.; Carr, K.; Gratzel, M.; Durrant, J. R. *Adv. Funct. Mater.* **2006**, *16*, 1832.

(60) Yanagida, S.; Yu, Y.; Manseki, K. *Acc. Chem. Res.* **2009**, *42*, 1827.

(61) Poplavskyy, D.; Nelson, J. *J. Appl. Phys.* **2003**, *93*, 341.

(62) Kroeze, J. E.; Hirata, N.; Schmidt-Mende, L.; Orizu, C.; Ogier, S. D.; Carr, K.; Grätzel, M.; Durrant, J. R. *Adv. Funct. Mater.* **2006**, *16*, 1832.

(63) Yang, L.; Xu, B.; Bi, D.; Tian, H.; Boschloo, G.; Sun, L.; Hagfeldt, A.; Johansson, E. M. J. *J. Am. Chem. Soc.* **2013**, *135*, 7378.

(64) Grancini, G.; Santosh Kumar, R. S.; Abrusci, A.; Yip, H.-L.; Li, C.-Z.; Jen, A.-K. Y.; Lanzani, G.; Snaith, H. J. *Adv. Funct. Mater.* **2012**, *22*, 2160.

(65) Abrusci, A.; Ding, I. K.; Al-Hashimi, M.; Segal-Peretz, T.; McGehee, M. D.; Heeney, M.; Frey, G. L.; Snaith, H. J. *Energy Environ. Sci.* **2011**, *4*, 3051.

(66) Yang, L.; Cappel, U. B.; Unger, E. L.; Karlsson, M.; Karlsson, K. M.; Gabrielsson, E.; Sun, L.; Boschloo, G.; Hagfeldt, A.; Johansson, E. M. J. Comparing spiro-OMeTAD and P3HT hole conductors in efficient solid state dye-sensitized solar cells. *Physical Chemistry Chemical Physics*, 2012, *14*, 779.

(67) Liu, X.; Zhang, W.; Uchida, S.; Cai, L.; Liu, B.; Ramakrishna, S. *Adv. Mater.* **2010**, *22*, E150.

(68) Zhang, W.; Cheng, Y.; Yin, X.; Liu, B. *Macromol. Chem. Phys.* **2011**, *212*, 15.

(69) Leijtens, T.; Ding, I. K.; Giovenzana, T.; Bloking, J. T.; McGehee, M. D.; Sellinger, A. *ACS Nano* **2012**, *6*, 1455.

(70) Snaith, H. J.; Grätzel, M. *Appl. Phys. Lett.* **2006**, *89*, 262114.

(71) Snaith, H. J.; Grätzel, M. *Adv. Mater.* **2007**, *19*, 3643.

(72) Snaith, H. J.; Humphry-Baker, R.; Chen, P.; Cesar, I.; Zakeeruddin, S. M.; Grätzel, M. *Nanotechnology* **2008**, *19*, 424003.

(73) Ding, I. K.; Tétreault, N.; Brillet, J.; Hardin, B. E.; Smith, E. H.; Rosenthal, S. J.; Sauvage, F.; Grätzel, M.; McGehee, M. D. *Adv. Funct. Mater.* **2009**, *19*, 2431.

(74) Melas-Kyriazi, J.; Ding, I. K.; Marchioro, A.; Punzi, A.; Hardin, B. E.; Burkhard, G. F.; Tétreault, N.; Grätzel, M.; Moser, J.-E.; McGehee, M. D. *Adv. Energy Mater.* **2011**, *1*, 407.

(75) Ding, I.-K.; Melas-Kyriazi, J.; Cevey-Ha, N.-L.; Chittibabu, K. G.; Zakeeruddin, S. M.; Grätzel, M.; McGehee, M. D. *Org. Electron.* **2010**, *11*, 1217.

(76) Docampo, P.; Hey, A.; Guldin, S.; Gunning, R.; Steiner, U.; Snaith, H. J. *Adv. Funct. Mater.* **2012**, n/a.

(77) Kim, H.-S.; Lee, C.-R.; Im, J.-H.; Lee, K.-B.; Moehl, T.; Marchioro, A.; Moon, S.-J.; Humphry-Baker, R.; Yum, J.-H.; Moser, J. E.; Grätzel, M.; Park, N.-G. *Sci. Rep.* **2012**, *2*.

(78) Kohle, O.; Grätzel, M.; Meyer, A. F.; Meyer, T. B. *Adv. Mater.* **1997**, *9*, 904.

(79) Kroon, J. M.; Bakker, N. J.; Smit, H. J. P.; Liska, P.; Thampi, K. R.; Wang, P.; Zakeeruddin, S. M.; Grätzel, M.; Hinsch, A.; Hore, S.; Würfel, U.; Sastrawan, R.; Durrant, J. R.; Palomares, E.; Pettersson, H.; Gruszecki, T.; Walter, J.; Skupien, K.; Tulloch, G. E. *Prog. Photovolt Res. Appl.* **2007**, *15*, 1.

(80) Hinsch, A.; Kroon, J. M.; Späth, M.; Roosmalen, J. A. M. van; Bakker, N. J.; Sommeling, P. M.; Burg, N. P. G. van der; Kinderman, R.; Kern, R.; Herber, J.; Schill, C.; Schubert, M.; Meyer, A.; Meyer, T.; Uhlendorf, I.; Holzbock, J. In *16th European Photovoltaic Solar Energy Conference and Exhibition*; 2000; Vol. 1702, pp. 1–7.

(81) Burschka, J.; Pellet, N.; Moon, S.-J.; Humphry-Baker, R.; Gao, P.; Nazeeruddin, M. K.; Grätzel, M. *Nature* **2013**, *499*, 316.

(82) Wang, M.; Moon, S.-J.; Xu, M.; Chittibabu, K.; Wang, P.; Cevey-Ha, N.-L.; Humphry-Baker, R.; Zakeeruddin, S. M.; Grätzel, M. *Small* **2010**, *6*, 319.

(83) Chen, C.-Y.; Wang, M.; Li, J.-Y.; Pootrakulchote, N.; Alibabaei, L.; Ngoc-le, C.-H.; Decoppet, J.-D.; Tsai, J.-H.; Grätzel, C.; Wu, C.-G.; Zakeeruddin, S. M.; Grätzel, M. *ACS Nano* **2009**, *3*, 3103.

(84) Ni, M.; Leung, M. K. H.; Leung, D. Y. C.; Sumathy, K. A review and recent developments in photocatalytic water-splitting using TiO2 for hydrogen production. *Renewable and Sustainable Energy Reviews*, 2007, *11*, 401–425.

(85) Dulub, O.; Batzilln, M.; Solovev, S.; Loginova, E.; Alchagirov, A.; Madey, T. E.; Diebold, U. *Science* **2007**, *317*, 1052.

(86) Wendt, S.; Schaub, R.; Matthiesen, J.; Vestergaard, E. K.; Wahlström, E.; Rasmussen, M. D.; Thostrup, P.; Molina, L. M.; Lægsgaard, E.; Stensgaard, I.; Hammer, B.; Besenbacher, F. *Surf. Sci.* **2005**, *598*, 226.

Chapter 3

Methods

3.1

Solid-State Sensitized Solar Cell Preparation

ssSSCs were prepared according to a standard procedure[1,2]. All solvents used in this work were reagent grade and anhydrous.

3.1.1
Mesoporous TiO_2 Anode

Fluorine-doped Tin Oxide (FTO) substrates (15 $\Omega\,cm^{-1}$, Pilkington) were etched with zinc powder and HCl (2 M in de-ionized water) to give the desired electrode patterning. The substrates were cleaned consecutively with Hellmanex (2 v % in de-ionized water), de-ionized water, acetone, and ethanol. The last traces of organic residues were removed by a 10 min oxygen plasma cleaning step. The FTO sheets were subsequently coated with a compact layer of TiO_2 (50 - 100 nm) by aerosol spray pyrolysis deposition at 300 °C, using air as the carrier gas. The solution used for spraying was composed of Titanium Isopropoxide in Ethanol at a 1:10 volume ratio. This layer is essential to minimize leakage current between the FTO anode and the solid-state hole transporter[3].

0.2-2 μm thick mesoporous TiO_2 films (as specified for each chapter) were then deposited by screen-printing (150 # thread count mesh) a commercial paste (Dyesol 18NR-T) diluted in terpineol, with a typical ratio of 3:1 by volume yielding 2 μm films. The TiO_2 films were slowly (45 minute ramp) heated to 500 °C and allowed to sinter for 30 min in air. The samples were immersed into 0.015 M $TiCl_4$ aqueous solution for 45 min at 70 °C, and then heated to 500 °C for another sintering step of

45 min. This step has been shown to be beneficial to current generation, although the exact mechanism is not yet completely understood. It has been proposed that the treatment increases the roughness of the nanoparticles, increasing the surface area for dye uptake. It has also been claimed to decrease the surface potential of the TiO_2 to facilitate electron injection and slow recombination processes[4].

3.1.2 Dye Sensitization

After cooling to 70 °C, the substrates were sensitized with dye absorbers. The substrates are kept at a temperature above 70 °C prior to immersion in the dye solution to minimize water adsorption. When using the organic dye D102, the substrates were immersed in a 0.5 mM ((5-{1,2,3,3a,4,8b-hexahydro-4-[4-(2,2-diphenylvinyl)phenyl]-cyclopeanta[b]indole-7-ylmethylene} - 4 - oxo - 2 - thioxo-thiazolidin - 3 -yl)acitic acid) (D102), dye solution (in 1:1 mixture of acetonitrile and tert-butyl alcohol) for one hour. In the case where the ruthenium complex dye C106 was used, the substrates were immersed in a 1 mM solution of NaRu(4,4-bis(5-(hexylthio)thiophen-2-yl)-2,2-bipyridine) (4-carboxylic acid-4-carboxylate-2,2-bipyridine) $(NCS)_2$ (C106) in 1:1 acetronitrile:tert-butanol mixture for 18 hours.

3.1.3 $CH_3NH_3PbI_{3-x}Cl_x$ Perovskite Sensitization

Perovskite precursor (methylammonium iodide) synthesis has been described elsewhere[5]. The perovskite was deposited on 200-700 nm (as specified in Chapters 6 and 7) mesoporous TiO_2 anodes by spin coating (speed 2,000 r.p.m., ramp 2,000 r.p.m. s^{-1}, time 60 s) a 20, 30 or 40 wt % (as specified in Chapters 6 and 7) solution of methylammonium iodide and $PbCl_2$ (3:1 molar ratio) in dimethyl formamide (DMF). The substrate was then heated to 100 °C for 45 min in an oven in air.

Mesosuperstructured Solar Cells

Mesosuperstructured solar cells (MSSCs) have recently received a great deal of attention[5,6], and are mesoporous-TiO_2 free. Here, the compact TiO_2 layer is deposited in the same was as for the ssSSCs, but an inert mesoporous Al_2O_3 scaffold is deposited by spin coating (speed 2,500 r.p.m., ramp 2,500 r.p.m. s^{-1}, time 60 s) a colloidal dispersion of 50 nm Al_2O_3 nanoparticles (Sigma-Aldrich, product number 702129) in isopropanol (1:2 by volume), followed by drying at 150 °C for 10 min, giving a 400-nm scaffold. The perovskite precursor solution (40 w %) was then spin coated (2000 rpm, 60 s) on top and dried as for the perovskite sensitized solar cells.

3.1.3 HTM Infiltration

After the dyed films were rinsed in acetonitrile, the 2,2′,7,7′-tetrakis-(*N*,*N*-di-*p*-methoxyphenylamine)9,9′-spirobifluorene (Spiro-MeOTAD, ordered from Lumtech) hole conductor matrix was applied by spin coating at 1000 rpm for 60 s in air. The solutions for spin coating consisted of Spiro-MeOTAD dissolved in anhydrous chlorobenzene (reagent grade) at 10 or 15 v % (as specified for the different experiments), assuming a density of Spiro-MeOTAD of 1 g cm^{-3}. 10 % v yields a 200 nm capping layer of HTM, while 15 % v gives a 700 nm capping layer of Spiro-MeOTAD on top of the mesoporous TiO_2 layer. In the case of perovskite sensitized or mesosuperstructured solar cells, 10 v % spiro-MeOTAD was spin coated at 2000 rpm for 60 s in air after allowing the substrate to cool for one minute after removal from the oven. Tert-butyl pyridine (*t*bp) was added to the solutions at a concentration of 80 mM. Lithium bis(trifluoromethylsulfonyl)imide salt (LiTFSI) (170 mg ml^{-1} in acetonitrile) was added to achieve the molar equivalent of 20 mol % relative to Spiro-MeOTAD, unless otherwise stated. After drying for at least 3 hours, back contacts were applied by thermal evaporation of 200 nm of silver using a shadow mask to define the electrode pattern.

3.2

Sample Preparation for Conductivity Measurements

In order to measure the conductivity of the charge transporting layers *in-situ*, devices for measuring conductivity were prepared almost identically to the way in which the full solar cells were prepared. Here, however, the different layers were deposited on glass rather than on a conducting electrode, no compact TiO_2 layer was employed, and the evaporated electrode pattern was generally in the two-point probe configuration, unless otherwise specified. Electrodes were either deposited directly on glass, so that the TiO_2 nanoparticles made good contact to the electrodes (for measuring TiO_2 electron conductivity), or on top of an HTM capping layer of 100-200 nm (for measuring HTM hole conductivity). This allows for measurement of either only the electron or only the hole conductivities, as has been previously demonstrated[7]. Note that no HTM is employed when measuring electron conductivity. More details are provided in Chapter 5. The electrode design was that of two inter-digitated electrodes with a 6.5 cm channel width (perpendicular to direction of the field), a 300 μm channel length, and a channel height dependent on the layer thickness, but typically 1-2 μm. Here, the electrode area was so large that contact resistance was negligible, as verified by performing 4-point probe and frequency dependent impedance measurements.

For monitoring the conductivity of polymers in blend morphology, solutions of 20 mg ml^{-1} of polymer in chlorobenzene, with 5-10 weight % of Phenyl-C61-butyric acid methyl ester ($PC_{60}BM$) were spin coated at 1000 r.p.m on glass substrates (after they had been cleaned in an oxygen plasma for 5 minutes). The deposition was performed in a nitrogen filled glovebox. The polymers used were: Poly(3-hexylthiophene-2,5-diyl) (P3HT), and Poly[2,6-(4,4-bis-(2-ethylhexyl)-4*H*-cyclopenta [2,1-*b*;3,4-*b*′]dithiophene)-*alt*-4,7(2,1,3-benzothiadiazole)] (PCPDBT). These polymers were also used as HTMs in the SSC architecture, at 20 mg ml^{-1}, spin coated at 1000 r.p.m on the dye sensitized TiO_2 substrates.

In the 4-point probe configuration, two thin (200 μm), straight electrodes were spaced evenly between two larger (1 mm) straight electrodes 6 mm apart, and with 1 cm channel width (perpendicular to electric field). The inner electrodes, with

2mm spacing, were placed only within the bottom 2 mm of the channel. Potential was applied to the outer electrodes, and the current measured. The potential drop across the inner electrodes was then measured and this was used to establish the contact resistance. More details about the measurements are given in the measurements section below.

3.3

Electrical Characterization

3.3.1
Solar Cell Characterization

For measuring the device merit parameters, solar-simulated AM 1.5 sunlight was generated with an ABET solar simulator (Xe lamp source) calibrated to give 100 mW cm^{-2} using an NREL-calibrated KG5 filtered silicon reference cell. The exact lamp power at the device measurement point was verified with the reference diode at the start of every set of measurements. J-V curves were recorded with a sourcemeter (Keithley 2400, USA) integrated with a desktop computer and a labview program developed in our laboratory. The merit parameters were calculated as described in Section 2.2. The active area of the devices was controlled by placing a metal aperture mask on the back of the device. This has been demonstrated to be essential for measuring accurate current densities, as it eliminates contributions from lateral charge collection[8].

3.3.2
Conductivity Measurements

In 2-point probe measurements, an electrical bias was simply applied across the in-plane contacts and the current measured as a function of bias, using a Keithley

sourcemeter (2400, USA). If the resulting I-V traces are linear and pass through the origin, the slope can be taken as the reciprocal of the sample resistance (R). This can be readily converted to conductivity (σ) by the simple relation below

$$\sigma = \frac{l}{Rwt} \tag{3.3.1}$$

where *w*, *l*, and *t* are the channel width (perpendicular to current flow), channel length (in direction of current flow), and film thickness respectively.

Because the contact between the metal electrode and semiconductor sample may not be ideal, the contact resistance between the gold electrode and active material may influence the total resistance of the sample. It is useful to perform 4-point probe measurements (geometry described in Section 3.2) to determine the exact contact resistance between the materials as a function of electrode area. Here, a sourcemeter (as before) is used to apply a bias across the two outer electrodes through the force channel. The two inner electrodes are connected to the sense channel of the sourcemeter, and the potential dropped across these two is monitored as a function of total applied bias. Since the distance between the two inner

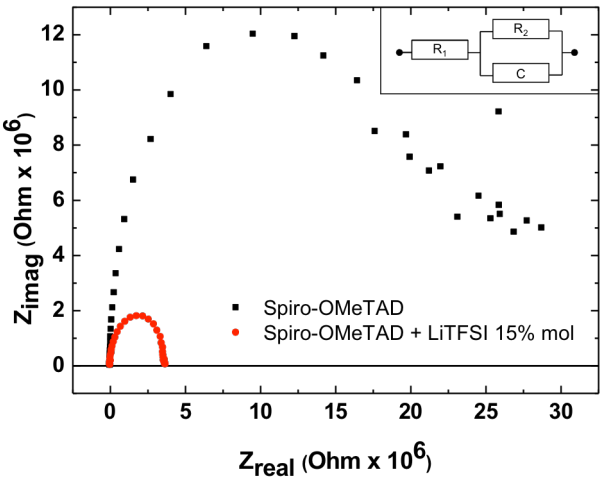

Figure 3.1. Representative Nyquist plots of 2-point probe conductivity samples using neat Spiro-MeOTAD and LiTFSI-doped Spiro-MeOTAD, in the device architecture described in Section 3.2. The inset depicts the equivalent circuit used to fit the data and extract the sample resistance and contact resistance.

electrodes is exactly $\frac{1}{3}$ of the total channel width, the potential dropped across the sample, not including the contact resistance, is simply 3 times that measured by the sense channel on the sourcemeter. Having measured the current flow through the sample, and knowing the potential dropped across the sample, it is trivial to calculate the actual sample resistance and contact resistances. Knowing the contact resistance for these samples, the contact resistance in the 2-point probe configuration can be extrapolated by taking into account the electrode area. In all architectures studied in this thesis, the contact resistance was too low to be measured.

Another method for determining the contact resistance directly in the 2-point probe setup is by performing impedance spectroscopy using a standard impedance analyser and potentiostat setup commercially available from Autolabs. Nyquist plots are taken at frequencies from 10 Hz–1 MHz of the impedance spectra, and fit to a simple equivalent circuit consisting of an element due to the contact resistance in series with an RC (in parallel) component, as depicted in Figure 3.1, where the inset depicts the equivalent circuit used. R_1, R_2, and C are the contact resistance, sample resistance, and sample capacitance respectively.

Figure 3.1 simply shows the data for two representative samples, where the contact resistances were determined to be 1 KOhm as opposed to 0.1-1000 MOhms for the sample resistances. The contact resistance is clearly negligible compared to the sample resistance. Similar data was found for all device architectures and doping levels used in this thesis, meaning that the 2-point probe configuration does not suffer from contact resistance effects. This is not surprising, as the materials used here are known to have very low mobilities, such that the sample resistance through the long channel will always be very high compared to the contact resistance. The same conclusions were drawn from the 4-point probe data, where the contact resistances were too small to be determined via our setup.

3.3.2
Determining Transport and Recombination Lifetimes in ssSSCs

Understanding the charge transport and recombination lifetimes in ssSSCs is essential to understanding loss mechanisms in the solar cells, as discussed in Section

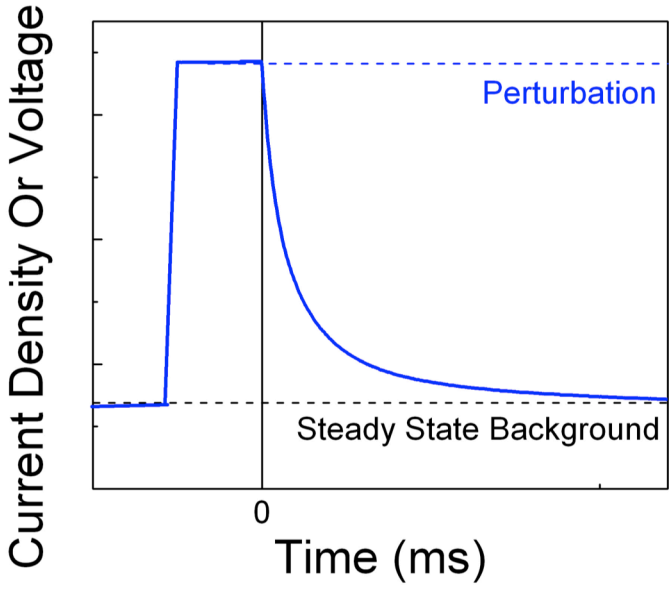

Figure 3.2. Example of a photo-current of photo-voltage perturbation measurement. The steady state signal (from controlled background illumination) is perturbed by a small (10 %) and short square LED pulse. The decay back to the steady state background signal is monitored and fit to an exponential function to extract the lifetime.

2.3. Accordingly, O'Regan *et al.* have developed a method by which to measure these parameters as a function of background illumination intensity, simply by monitoring small photocurrent and photovoltage perturbations caused by light emitting diode (LED) light pulses[9]. Through this method, it is possible to accurately determine the relevant timescales as a function of charge density within the solar cell, and hence to understand whether charge collection efficiency may be limiting a given system.

The basic principle of the measurements is that a constant white light background of controlled intensity (1-100 mW cm^{-2}) is perturbed by a short pulse of light of less than 10 % of the background intensity. A small perturbation is used so that it does not significantly influence the steady state dynamics of the system, and the timescales extracted from the perturbation can be associated with the background illumination level. To determine the charge transport lifetime, the solar cell is held at short circuit, and the J_{SC} response to the perturbation is recorded on an oscilloscope. The decay back to the steady state current is then fitted to a single exponential function to yield the relevant lifetime. In the situation where charge collection out competes recombination mechanisms, this lifetime is associated to the removal of excess charge (from the perturbation) from the device by collection at the electrodes. If the solar cell being tested exhibits very fast recombination rates,

however, this J_{SC} decay lifetime can be affected not just by current extraction, but also by recombination. To distinguish the two, the identical measurement is performed, but now the current is kept constant by use of a sourcemeter, so that the light perturbation must take the form of a voltage rise and subsequent decay. The voltage decay at constant current then corresponds to the time in which the charges recombine. Knowing the recombination lifetime (τ_R) under the same conditions as the total J_{SC} decay lifetime (τ_{JSC}) allows one to calculate the charge transport lifetime (τ_T) through the relation below.

$$\tau_T = \frac{1}{\frac{1}{\tau_{Jsc}} - \frac{1}{\tau_R}} \tag{3.3.2}$$

One can then approximate the charge collection efficiency (η_C) as a ratio of the rate of charge collection vs all the total decay pathways. This has been demonstrated to be viable at estimated collection efficiencies over 70 %[10].

$$\eta_C = \frac{\frac{1}{\tau_T}}{\frac{1}{\tau_T} + \frac{1}{\tau_R}} \tag{3.3.3}$$

This analysis is performed at many light biases to see the dependence on the charge densities, and to better understand the mechanisms of charge transport and recombination in ssSSCs. To estimate the charge density due to the background white light bias, the background light is simply turned off, and the current decay is integrated to yield the total steady state charge density that present in the system under constant illumination.

The charge densities at a given light bias will be very different at short circuit than at open circuit. For this reason, the recombination lifetime at open circuit is equally important for understanding the recombination mechanisms in a given ssSSC. Here, identical measurements are taken as for that done to determine the

short circuit recombination lifetime, but the current is held to 0 (the cell is held at open circuit).

Aside from monitoring charge collection and recombination lifetimes, it can also be informative to determine the density of states (DOS) in a material such as TiO_2, where the density and surface potential of surface states can be influenced by surface treatments, dye chemistry, and atmospheric effects. An example DOS was given for TiO_2 in a ssSSC using D102 as the dye in Figure 2.6. Again, a small light perturbation is added on top of a steady background illumination. Now, holding the cell at open circuit, the voltage perturbation (ΔV) is recorded. Then, keeping the experimental parameters identical but holding the cell as short circuit, the current perturbation is integrated to give the amount of charge injected by the perturbation (ΔQ). Now at a given background light intensity (and corresponding steady state V_{OC}), it is possible to determine the capacitance, C and to determine the DOS[11].

$$C = \frac{\Delta Q}{\Delta V} \tag{3.3.4}$$

3.3

Spectroscopy

3.3.1
Absorption Measurements

Absorbance measurements of films were taken using a commercial spectrophotometer (Varian Cary 300 UV - Vis, USA) with an internally coupled integrating sphere (Labsphere, USA). Within the sphere is an integrated photomultiplier tube that detects the light. Samples were mounted at the entrance of the sphere, with a diffuse reflector mounted on an 8° wedge at the exit port. Baseline measurements were performed on mesoporous TiO_2 samples on glass, the same as the substrates used for the samples.

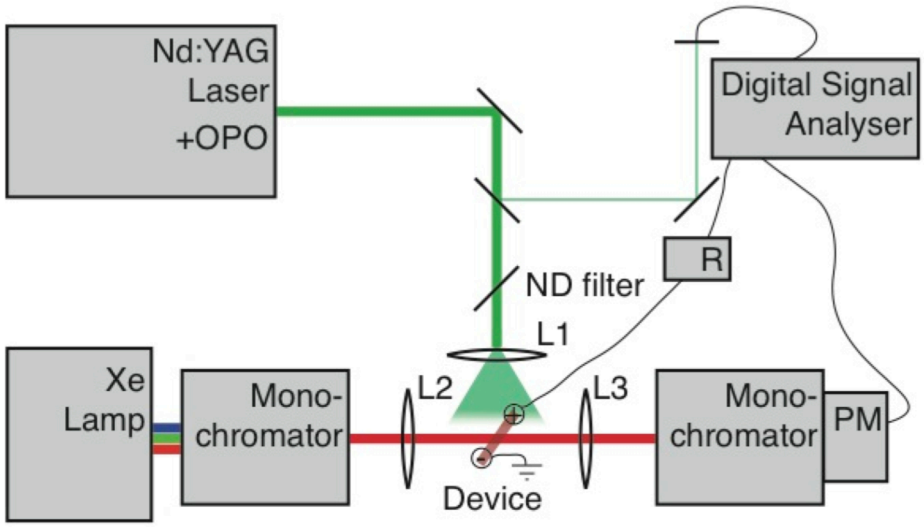

Figure 3.3. Schematic depiction of the transient absorption setup used in this thesis. Excitation wavelength of 550 nm, at a pulse intensity of 50 μJ cm^{-2} and 10 Hz repetition rate was generated by an Nd:YAG laser and tuned by an optical parametric oscillator (OPO) and used unless otherwise specified. The monochromated probe light was detected by a photo-multiplier tube (PM) detection system and relayed to an oscilloscope which was triggered by a photodiode. The device can be electrically connected to the oscilloscope via a variable resistor (R) to monitor photo-induced electrical changes.

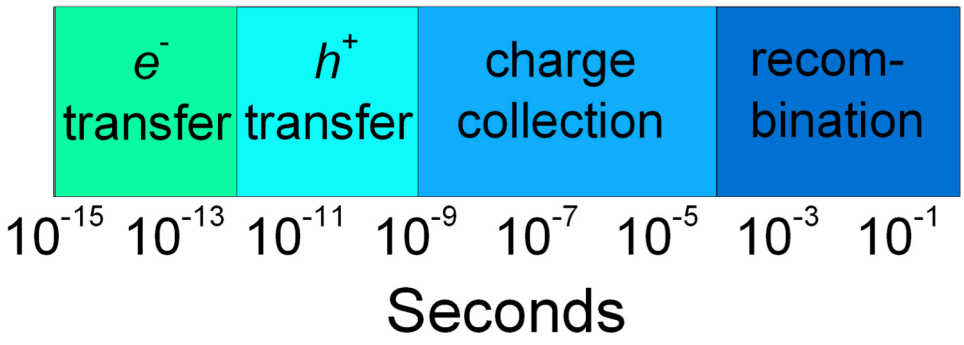

Figure 3.4. Schematic depiction of the 4 main photo-induced processes as a function of time after the excitation: electron transfer the dye to TiO_2, hole transfer to HTM, charge collection at the electrodes at short circuit, and recombination processes. In reality, these processes do overlap somewhat in timescales and depends on device architecture, but the depiction corresponds quite closely to the timescales on which the events tend to occur.

3.3.2
Transient Absorption Spectroscopy (TAS)

The Nobel Prize in Chemistry 1967 was awarded to Manfred Eigen, Ronald George Wreyford Norrish, and George Porter "for their studies of extremely fast chemical reactions, effected by disturbing the equilibrium by means of very short pulses of energy". Here, a photo-induced reaction's progress can be monitored by recording the change in a sample's absorption as a function of time after the initial photo-excitation. This is termed transient absorption spectroscopy (TAS). With improvements in laser technology, broadband light generation, and optical delay tables, the technique has since been developed to enable resolution of events on time scales from 10^{-12} - 1 seconds. The different excited states and charged states of materials used in photovoltaic devices, including ssSSCs, have distinct absorption spectra. As a result, this technique is readily applicable to study all of the processes described in Section 2.3 for ssSSCs. Figure 3.4 gives a schematic depiction of the time scales of the four main processes of electron injection, hole transfer to the HTM, charge collection at short circuit, and recombination[1,12]. Although the processes are depicted as solid blocks in the schematic, there is more overlap of time scales in reality, and the blocks are merely a representation of the typical timescales over which most of these events occur. In this thesis, the focus is primarily on events occurring after the initial electron and hole transfer to TiO_2 and HTM respectively; ie recombination events occurring on the µs – ms time scale. The setup is depicted in

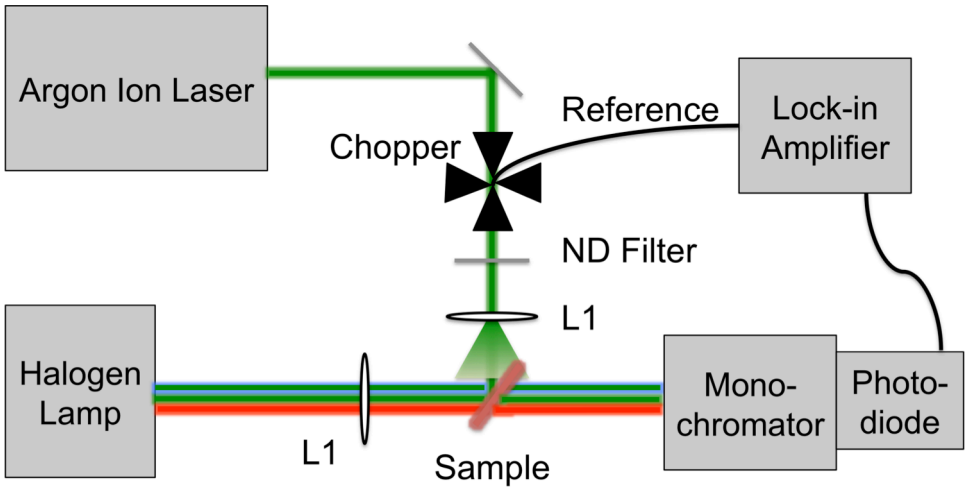

Figure 3.5. Steady state photo-induced absorption (PIA) setup used in this thesis. Excitation wavelength was 514 nm at a power of 50 mW cm^{-2} produced by a tunable argon ion laser unless otherwise specified, which was modulated by an optical chopper. The lock-in amplifier was phased to the signal of the chopped laser beam, while the probe light was generated by a halogen lamp.

Figure 3.3. In the setup used here, an Nd:YAG laser is coupled to an automatically controlled optical parametric oscillator (OPO), which provides the ability to tune the excitation wavelength. The repetition rate of the system is 10 Hz. On its path towards the sample, the beam is split so that a small fraction of the light is transmitted onto a quick Si photodiode that functions as the trigger for the oscilloscope (Digital Signal Analyzer). Using a lens, the excitation can be focused or defocused at the sample. A Xenon lamp, coupled to a monochromator, provides a constant monochromatic probe beam that passes through the same spot as the excitation pulse. After passing through the sample, the light is again monochromated and then detected by a photo-multiplier (PM). The signal is then relayed to the oscilloscope. Electrical connections can be made to the sample as desired. For transient conductivity measurements, the sample geometry was that of the 2-point probe configuration, and the electrodes were placed in series with a voltage source and the oscilloscope (more details in Chapter 5).

3.3.3.
Quasi Steady State Photo-Induced Absorption Spectroscopy

Photo-induced absorption (PIA) spectroscopy can be a useful technique to determine which photo-induced species are dominant under steady-state illumination conditions in a given solar cell architecture. Here, a continuous wave (cv) laser beam is modulated by an optical chopper and used to modulate the photo-excitation of the sample. A constant probe beam is transmitted through the sample, and its intensity monitored by a photodetector. The photo-induced changes in transmission (T) tend to be very small ($\Delta T/T < 10^{-3}$) so that they are very difficult to detect. To overcome this problem, the signal is fed to a lock-in amplifier set to the same frequency and phase as the photo-excitation modulation. In this way, very small changes can be accurately monitored.

The setup used for these measurements was similar to that depicted in Figure 3.2 for the TAS setup, and is depicted in Figure 3.5. A tunable cw Argon ion laser was used as excitation source, an optical chopper placed between the laser and the sample, the probe beam was provided by a halogen lamp, the light was monochromated after the sample, and a lock-in amplifier (Stanford Instruments) was used rather than an oscilloscope to analyze the signal. To ensure that the steady state populations were monitored, a slow chopping frequency of 23 Hz was chosen. This frequency choice means that the predominant species for the samples tested were the separated charge species with lifetimes of μs-100s of ms.

3.3.4
^{7}Li-Nuclear Magnetic Resonance

^{7}Li solid state NMR spectra were recorded at 155.45 MHz on a Bruker Avance II spectrometer equipped with a 4 mm MAS probe. A π/2 pulse width of 4.5 μs was used, with a relaxation delay of 120 s and a spinning speed of 8-10 kHz. Chemical shifts are referenced to external $LiCl_{(aq)}$ 1 M. These measurements were performed

by Roberto Avolio and Maria E. Errico at the Institute of Polymer Chemistry and Technology (ICTP), National Research Council of Italy.

3.3.5
Fourier Transform InfraRed Spectroscpy

Fourier Transform-InfraRed (FTIR) spectra were collected on a Bio-Rad FTS-6000 FTIR spectrometer fitted with a Mercury-Cadmium-Telluride detector using a DuraSamplIR II diamond ATR accessory. Each spectrum is the result of 50 co-added scans at a resolution of 1 cm^{-1} and are displayed as $A = -\log_{10}(\frac{R}{R_0})$ where R_0 is a blank spectrum of the accessory. These measurements were performed by Ian J. McPherson in the Department of Inorganic Chemistry at Oxford University.

3.4
Scanning Electron Microscopy

Scanning electron microscopy (SEM) images were taken on cross-sections of ssSSCs. The cross-sections were prepared by first scribing a small scratch on the active layer with a diamond-tipped pen, cooling with liquid nitrogen, and then breaking the sample along the scratch. The SEM machine used was a commercially available Hitachi S4300 field emission SEM.

.

3.5

References

(1) Bach, U.; Lupo, D.; Comte, P.; Moser, J. E.; Weissortel, F.; Salbeck, J.; Spreitzer, H.; Grätzel, M. *Nature* **1998**, *395*, 583.

(2) Abrusci, A.; Ding, I. K.; Al-Hashimi, M.; Segal-Peretz, T.; McGehee, M. D.; Heeney, M.; Frey, G. L.; Snaith, H. J. *Energy Environ. Sci.* **2011**, *4*, 3051.

(3) Snaith, H. J.; Gratzel, M. *Adv. Mater.* **2006**, *18*, 1910+.

(4) O'Regan, B. C.; Durrant, J. R.; Sommeling, P. M.; Bakker, N. J. *J. Phys. Chem. C* **2007**, *111*, 14001.

(5) Lee, M. M.; Teuscher, J.; Miyasaka, T.; Murakami, T. N.; Snaith, H. J. *Science (80-.).* **2012**, *338*, 643.

(6) Ball, J. M.; Lee, M. M.; Hey, A.; Snaith, H. J. *Energy Environ. Sci.* **2013**.

(7) Snaith, H. J.; Grätzel, M. *Adv. Mater.* **2007**, *19*, 3643.

(8) Snaith, H. J. How should you measure your excitonic solar cells? *Energy & Environmental Science*, 2012, *5*, 6513.

(9) O'Regan, B. C.; Lenzmann, F. *J. Phys. Chem. B* **2004**, *108*, 4342.

(10) Sivaram, V.; Kirkpatrick, J.; Snaith, H. *J. Appl. Phys.* **2013**, *113*, 063709.

(11) Docampo, P.; Guldin, S.; Stefik, M.; Tiwana, P.; Orilall, M. C.; Hüttner, S.; Sai, H.; Wiesner, U.; Steiner, U.; Snaith, H. J. *Adv. Funct. Mater.* **2010**, *20*, 1787.

(12) Bach, U.; Tachibana, Y.; Moser, J.; Haque, S. A.; Durrant, J. R.; Grätzel, M. *J. Am. Chem. Soc.* **1999**, *121*, 7445.

Chapter 4

Lithium Salts as p-Dopants in Solid State Sensitized Solar Cells

The work presented in this chapter has been published in:

(1) *Abate, A.; *Leijtens, T.; Pathak, S.; Teuscher, J.; Avolio, R.; Errico, M. E.; Kirkpatrik, J.; Ball, J. M.; Docampo, P.; McPherson, I.; et al. Lithium Salts as "Redox Active" P-Type Dopants for Organic Semiconductors and Their Impact in Solid-State Dye-Sensitized Solar Cells. *Phys. Chem. Chem. Phys.* **2013**, *15*, 2572–2579.

*These two authors contributed equally.

(2) Agrawal, S.; Leijtens, T.; Ronca, E.; Pastore, M.; Snaith, H.; De Angelis, F. Modelling the Effect of Ionic Additives on the Optical and Electronic Properties of a Dye-Sensitized TiO2 Heterointerface: Absorption, Charge Injection and Aggregation. *J. Mater. Chem. A* **2013**, *1*, 14675–14685.

4.1

Context and Summary

Lithium salts have been shown to dramatically increase the conductivity in a broad range of polymeric and small molecule organic semiconductors, including the HTM used in ssSSCs, Spiro-MeOTAD. Still, the mechanism explaining this effect has remained a mystery. Similarly, the importance of the commonly employed LiTFSI salt on ssSSC performance has not been thoroughly understood. In this chapter, a p-doping mechanism is unveiled, where Li^+ p-dopes Spiro-MeOTAD in the presence of oxygen. After establishing the lithium doping mechanism, the role of LiTFSI in ssSSCs is fully unravelled for the first time, and is demonstrated to be essential to minimizing series resistance losses in the solar cells. The doping mechanism consumes Li^+, which poses a problem, since the lithium salt is required at the dye-sensitized heterojunction to enhance charge generation and slow charge recombination rates. This compromise highlights that new additives are required to maximize the performance of ssSSCs. The doping mechanism is dependent on

atmospheric conditions and may continue to be active for far longer than just the device preparation time. This poses a question as to the viability of such additives for the long-term stability of ssSSCs.

4.2

Introduction

One of the original scientific breakthroughs for organic solids was the ability to modulate their electrical conductivity using chemical doping, and hence demonstrate their semiconducting properties[1]. Similar to inorganic semiconductors, doping intentionally introduces chemical impurities into the organic semiconductors for the purpose of adjusting material properties to the specific application; *e.g.*, triphenylamine-based organic semiconductors have been p-doped with Co(III) complexes and Sb salts in ssSSCs[2,3] and tetracyano-quinoline derivatives in organic light emitting diodes (OLEDs)[4]. Both applications benefit from the introduction of a p-doped transport layer since it reduces the charge transport resistance in series with the p-n junction[2,3,5–7] and helps to achieve Ohmic contacts[8,9]. Generally, chemical p-doping agents tend to be comprised of molecules with relatively high electron affinities, often in the form of metal-organic complexes or organic resonance structures, which can generate unpaired electrons in the organic matrix by means of stable charge transfer complexes[10–12]. The overall result of such doping is a significant increase in the concentration of free holes in the HOMO, with an associated enhancement in conductivity, especially at high concentrations[13–15].

Recently, lithium salts have been reported to enhance the conductivity in a range of polymeric organic semiconductors[16,17]. Xia *et al.* found that lithium salts enhance the hole transport in polythiophene derivatives[18]. They discussed the effect of different anions without considering the role of the Li^+ ion itself. LiTFSI has also been shown to dramatically increase the conductivity and hole mobility in small molecule organic semiconductors, such as Spiro-MeOTAD[7]. To explain the effect of increased conductivity and apparent increase in mobility, it was previously suggested that the ionic species in the organic matrix smooth the potential

landscape, increasing the probability of intra-molecular charge transfer[7,15]. The resultant 5 - 10 fold measured increase in hole mobility was then used to rationalize the observed 100 fold increase in conductivity. The LiTFSI additive was considered redox inactive, and initial UV-Vis absorption measurements showed no signature of oxidized hole transporter in solution[7]. For this reason, the hole density was not considered to be significantly affected by addition of LiTFSI, leaving at least an order of magnitude increase in conductivity unaccounted for.

ssSSCs incorporating molecular or polymeric hole-transporters employ lithium salts as additives to the organic phase[17,19,20]. It was considered that the primary role is to force a negative shift in the surface potential of the TiO_2, favouring forward electron-transfer from the photoexcited tethered dye[21], as well as retardation of recombination processes by ionic screening[22]. Optimizing the additive concentration according to this knowledge led to a step increase in performance[22]. Nevertheless, the influence of the lithium salts in the ssSSCs is wide ranging,[7,21–27] and despite many studies on the subject, the full role in ssSSCs has remained somewhat of a mystery. In particular, the role of LiTFSI on charge transport in working ssSSCs has never been fully explored.

4.3

p-Doping and Conductivity

The first aim of this study was to understand the effect of lithium salts addition on the charge transport in organic semiconductors, and particularly on LiTFSI and Spiro-MeOTAD. Figure 4.1 displays the dependence of the Spiro-MeOTAD conductivity on the LiTFSI content. The method employed has been previously described for measuring the effective Spiro-MeOTAD conductivity in conditions similar to device operation[28] and is described in detail in Chapter 3. A strong trend is evident, where the conductivity increases from a very low 3×10^{-8} up to 3×10^{-5} S cm^{-2} with increasing LiTFSI content. Notably, the conductivity reaches the maximum at the LiTFSI content usually employed in

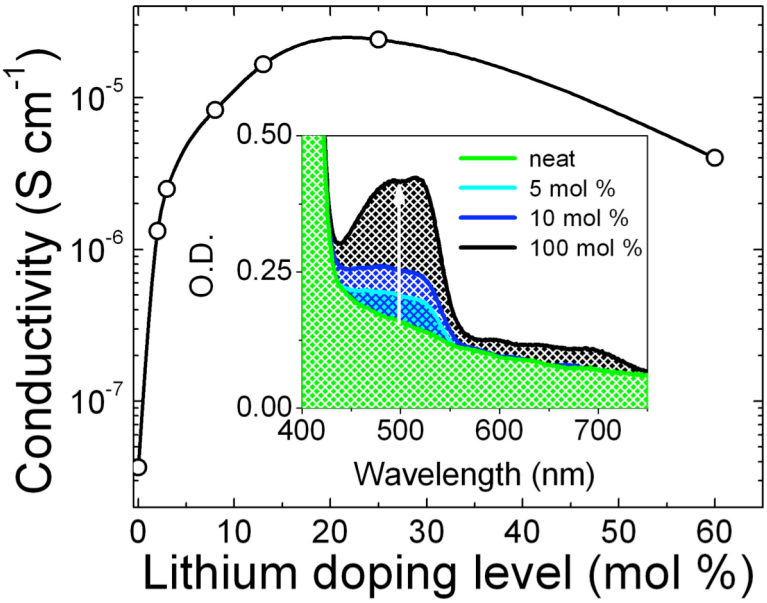

Figure 4.1. Spiro-MeOTAD conductivity and UV-Vis absorption spectra (inset) as a function of the LiTFSI content with respect to Spiro-MeOTAD concentration. These films were left for 78 hours in air, in the dark, before measurement. The solid-line is simply to aid the eye.

ssSSCs (12 – 30 mol %)[2,19], suggesting that this effect on the hole conduction may be important in the device performance.

So far, this remarkable increase in conductivity has been exclusively ascribed to the electrostatic charge of the ionic species added into the organic matrix[7,18]. In particular, it was claimed that the addition of LiTFSI does not induce charge transfer complexes, and extra addition of chemical p-dopants is necessary to oxidize the Spiro-MeOTAD[2,7,19]. However, the UV-Vis absorption spectra of mesoporous TiO_2 films infiltrated with Spiro-MeOTAD (inset in Figure 4.1) show the clear growth of an absorption band around 520 nm as the concentration of LiTFSI is increased, which is indicative of a Spiro-MeOTAD oxidized state (p-doping)[2,29]. The absorption increment with the LiTFSI content suggests that the salt could be involved in the oxidation of Spiro-MeOTAD.

Organic semiconductors, including triphenyl amines such as spiro-MeOTAD, are readily oxidized by atmospheric oxygen, leading to p-doping by the formation of a charge transfer complex[30–32]. To shed light on the doping mechanism, a time series of the conductivity measurements in different experimental conditions (atmosphere and salt content) was performed. Figure 4.2a shows the absorbance of the oxidized

Spiro-MeOTAD probed at 520 nm as a function of time for a range of LiTFSI contents. The rate of Spiro-MeOTAD oxidation seems to increase with LiTFSI concentration, while the final degree of oxidation achieved scales approximately linearly with increasing LiTFSI concentration. This allows one to conclude that LiTFSI does not participate as a catalyst, but as a reagent being consumed while the reaction progresses.

4.4

Mechanism: the Roles of Oxygen and Li^+

It is well known that in the primary processes of photo-oxidation, molecular oxygen plays the role of p-dopant[30,33–36]. To probe whether oxygen is involved in the oxidation of Spiro-MeOTAD, devices were prepared to measure conductivity in oxygen-free conditions with and without the addition of a standard amount (10 mol % with Spiro-MeOTAD) of LiTFSI. Figure 4.2b shows that for devices fabricated with and without LiTFSI, but never exposed to air, the conductivity of Spiro-MeOTAD is approximately the same. This observation confirms that the electrostatic effect of the ionic species[7] alone is not sufficient to explain the increase in conductivity, and indeed raises the question as to whether the "smoothing of the potential landscape" from the presence of the $TFSI^-$ counterion has a significant influence at all. Once exposed to air, the sample with LiTFSI shows a rapid increase in conductivity of over two orders of magnitude to reach the same final conductivity value as previously determined for films made in air. The completion of this process for the same LiTFSI content moreover seems to occur on a similar timescale as what is observed in Figure 2a and is not reversible when the sample is placed back in oxygen-free conditions, as the conductivity remains at 8×10^{-6} S cm^{-1} after 78 hours in a nitrogen environment. On the other hand, the sample without LiTFSI (neat Spiro-MeOTAD) has a generally constant conductivity over time, allowing us to conclude that both LiTFSI and oxygen play a central role in the doping mechanism, and that the observed phenomenon is distinct from the long-known oxygen doping mechanism[30,33–36]. The slight decrease in conductivity for the samples containing no

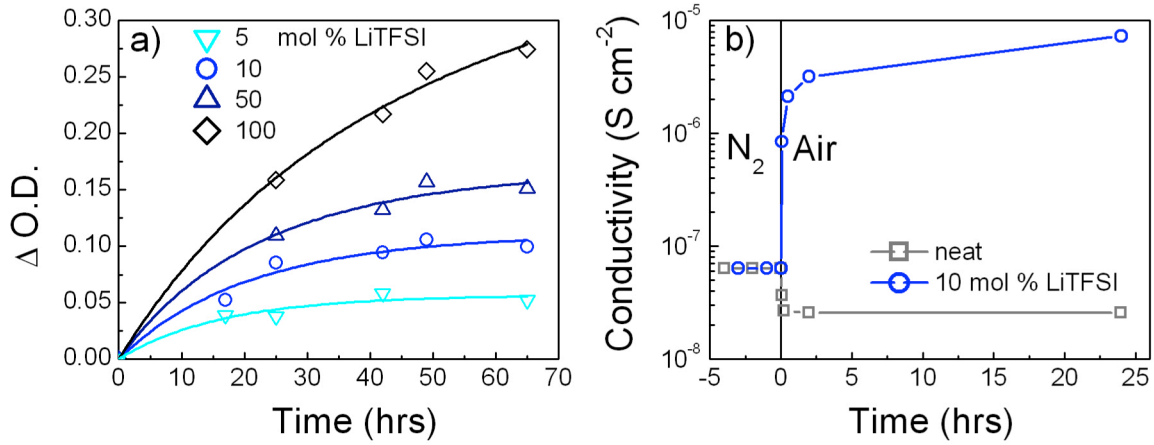

Figure 4.2. Characteristics of Spiro-MeOTAD with different LiTFSI content in air and in nitrogen atmosphere. (a) Variation of optical density probed at 520 nm in Spiro-MeOTAD infiltrated TiO_2 films as a function of time in air. The legend gives the mol % of LiTFSI with respect to Spiro-MeOTAD. (b) The effective conductivity of Spiro-MeOTAD (infiltrated into dye sensitized TiO_2) as a function of time, before (in nitrogen) and after exposure to air. The improved conductivity of the doped spiro-MeOTAD does not change from 8×10^{-6} S cm^{-1} after being placed back in an oxygen free atmosphere (N_2) for 78 hours, suggesting that the change is irreversible. Similar effects were observed when infiltrating mesoporous SiO_2 films with Spiro-MeOTAD, reaching conductivities of 3×10^{-6} S cm^{-1} under pure oxygen atmosphere.

LiTFSI could be explained by the fact that the TiO_2 nanoparticles used in our devices have been shown to contain Ti^{3+} cations at the surface due to the presence of oxygen vacancies[37,38]. Oxygen adsorbs to these sites, forming O_2^-, a powerful reducing agent. We postulate that these surface bound superoxide molecules may act as hole traps to reduce the overall HTM mobility when the samples are in an O_2 – containing atmosphere. A possible contribution of the other air components (mainly water) as well as the TiO_2 itself was excluded by performing a similar experiment in pure oxygen on spiro-MeOTAD infiltrated mesoporous SiO_2 films. The conductivities did not reach quite the same values as those in the dye sensitized TiO_2 (3 vs 8×10^{-6} S cm^{-1}), but it is difficult to compare, as the nanoparticle sizes, and hence exposed HTM surface area and HTM pore filling fractions, will differ in the two geometries with likely influences on reaction rates.

In order to identify the reaction products, solid-state spectrochemical analyses were performed on materials in conditions similar to device operation. Figure 4.3a shows the ^7Li NMR of LiTFSI and Spiro-MeOTAD with LiTFSI (10 mol %) spectra recorded in the solid-state[39,40]. At the concentration commonly employed in ssSSCs[2], LiTFSI is perfectly solubilised in the Spiro-MeOTAD film as evidenced by relatively narrow lines under magic angle spinning, which suggest a weak

homonuclear coupling[41]. The spectrum of the doped Spiro-MeOTAD film, detected immediately after the preparation, contains a single ^{7}Li resonance, slightly shifted from the bulk LiTFSI signal due to the different chemical environment. Interestingly, after oxidation occurs (12 hrs in air), two different ^{7}Li resonances are recorded. This indicates a change in the coordination of Li atoms with the formation of complexes[42] which are likely to involve oxygen and the Spiro-MeOTAD molecules. In particular, the downfield peak (0.02 ppm) is shifted towards the range of lithium-oxygen species (3.3 ppm for Li_2O, 0.3 ppm for Li_2O_2 as determined experimentally and plotted in Figure 4.3c). The narrow line width indicates a molecular dispersion of these species rather than an organization in crystalline structures[43]. Direct comparison to the

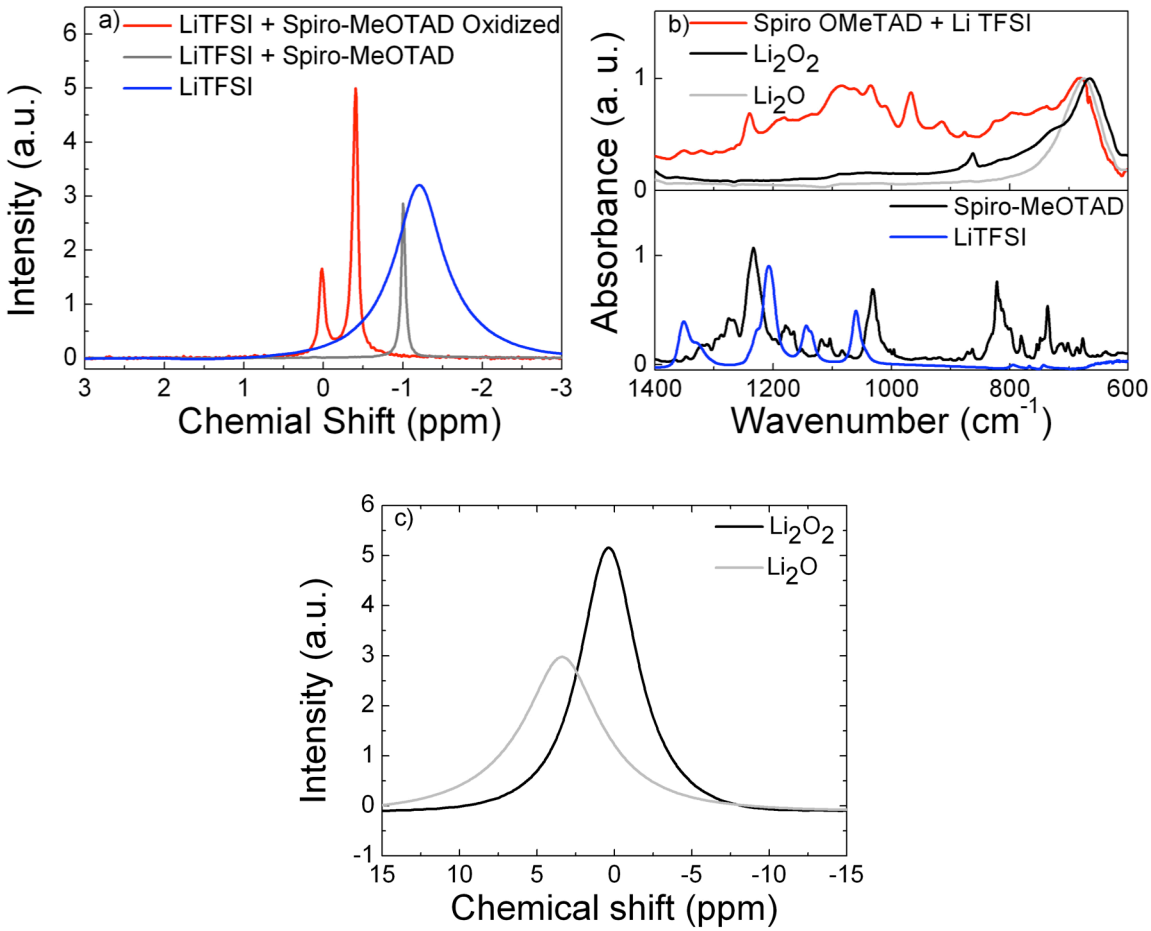

Figure 4.3. (a) Solid state ^{7}Li NMR of neat LiTFSI and Spiro-MeOTAD with the addition of 10 mol % LiTFSI collected immediately after the preparation and after 12 h left in air (the LiTFSI spectrum after 12 h in air is not reported being substantially the same). (b) ATR-FTIR spectra of the powder extracted from the oxidized Spiro-MeOTAD + LiTFSI sample (which we postulate to contain Li_xO_y), compared with the Li_2O and Li_2O_2 (top graph) and the spectra of the starting material (bottom graph). (c) Solid state ^{7}Li NMR of commercial Li_2O_2 and Li_2O powders. ^{7}Li NMR spectra were taken by Roberto Avolio and Maria E. Errico at the Institute of Polymer Chemistry and Technology (ICTP), National Research Council of Italy, and ATR-FTIR spectra were taken by Ian J McPherson at the Inorganic Chemistry Laboratory, University of Oxford. The NMR data was primarily analyzed by Antonio Abate in the Physics Department at the University of Oxford.

reference Li_2O and Li_2O_2 species is unfortunately not possible here because of the difference in local environment.

In order to further investigate the reaction products, Spiro-MeOTAD (with 10 mol % LiTFSI) films were dissolved in anhydrous chlorobenzene / dimethyl sulfoxide to extract the formed oxides. When the solution is left in the dark and nitrogen for several days, a white powder precipitates. The filtered solid was washed with anhydrous chlorobenzene to remove any remaining organic components and dried in air. Figure 4.3b shows the attenuated total reflectance FTIR (ATR-FTIR) spectra of the collected powder. The absorption profile is clearly different from the starting materials, and a large peak appears at 682 cm^{-1}. Similar peaks are observed in the IR spectra of Li_2O and Li_2O_2 and can be ascribed to Li-O vibrational stretching modes[44].

The data presented above can be used to draw qualitative conclusions concerning the mechanism that drives the lithium salts and oxygen to be effective p-dopants (when employed together) for organic semiconductors. The low ionization potential of Spiro-MeOTAD and the high electron affinity of the molecular oxygen leads to a weakly bound donor-acceptor complex, which can result in an effective electron transfer to the oxygen molecule, as illustrated in equation 4.1[45,46]. This can be accelerated by light induced excitation. As observed by the UV-Vis spectra and conductivity measurements, the concentration of oxidized Spiro-MeOTAD (Spiro-MeOTAD$^+$ O_2^-) is negligible in the absence of LiTFSI. However, the addition of the Li^+ changes the equilibrium of equation 1 in the direction of the oxidized Spiro-MeOTAD by consuming O_2^- as described in equation 4.2[44,47–49].

$$\text{Spiro-MeOTAD} + O_2 \leftrightarrow \text{Spiro-MeOTAD}^{\bullet+}\ O_2^- \qquad (4.1)$$

$$\text{Spiro-MeOTAD}^{\bullet+}\ O_2^- + Li^+\ TFSI^- \rightarrow \text{Spiro-MeOTAD}^{\bullet+}\ TFSI^- + Li_xO_y \qquad (4.2)$$

where Li_xO_y stands for lithium oxide complexes, which can be tentatively identified as Li_2O or Li_2O_2 from the ATR-FTIR and ^7Li NMR data presented in Figure 4.3. The

formed Spiro-MeOTAD radical cation (Spiro-MeOTAD$^+$ TFSI$^-$) is weakly bound by the highly delocalized charge on the TFSI$^-$ anion, which results in an effective generation of mobile holes on the organic matrix. According to the proposed mechanism, it is most likely that the oxygen radicals will form LiO_2 upon exposure to Li^+ ions, which readily decomposes to Li_2O_2[44,47].

4.5

Influence on Charge Generation and Collection

In order to determine the impact of the lithium doping mechanism on ssSSCs performance, a series of devices with different LiTFSI content were prepared, using the D102 indolene dye sensitizer. Figure 4.4 shows the device figures-of-merit for each LiTFSI concentration. Confirming what was observed in the literature[23], there is a strong improvement in the short-circuit photocurrent (J_{sc}) and fill factor (*FF*), while the open circuit voltage (V_{oc}) decreases with the increased LiTFSI content. Notably, however, the short-circuit photocurrent begins to decrease as the LiTFSI content is

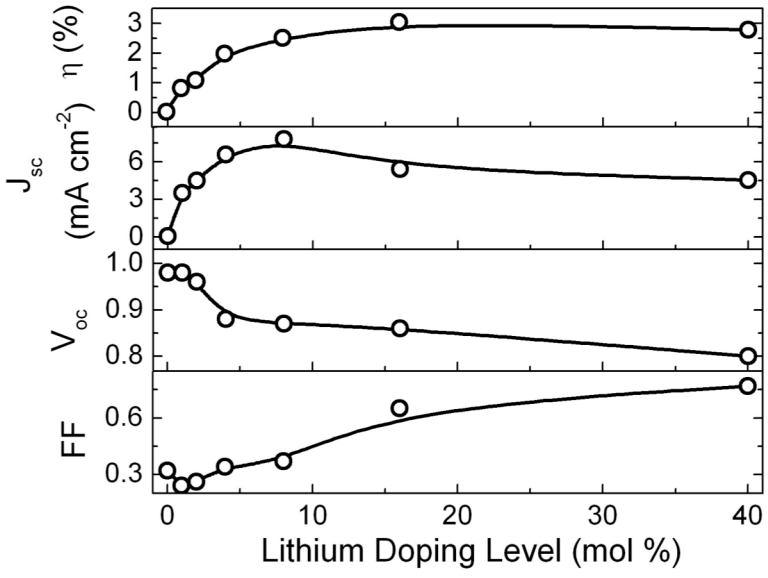

Figure 4.4 Device performance parameters, efficiency (η), short-circuit current (J_{sc}), open-circuit voltage (V_{oc}) and fill factor (*FF*), as function of the LiTFSI content, extracted from current voltage curves of ssSSCs employing D102 as the sensitizer measured under AM1.5 simulated sun light of 100 mW cm $^{-2}$ equivalent solar irradiance. Each point is representative of the four devices prepared per LiTFSI content, where the *t*bp concentration is kept constant at the standard concentration of 80 mM. The TiO_2 layer was 2 µm thick while the HTM capping layer was 700 nm to stress the impact of HTM conductivity on device performance.

increased beyond 10 mol % (with respect to Spiro-MeOTAD), although the *FF* continues to improve giving an optimal performance around 20 mol % LiTFSI to Spiro-MeOTAD. This suggests that LiTFSI has a broad impact on a number of processes occurring in the solar cells, which are possibly working in opposite senses. The ground state absorption in the dye-sensitizer (Figure 4.5) and the electron transfer efficiency from the photoexcited dye into the TiO_2 are strongly influenced by the presence of LiTFSI. This has been observed before for this specific dye, and has been assigned to a change in the local polarity of the hole-transporter medium in the vicinity of the dye[20,21]. Additionally, LiTFSI has also been shown to affect the charge dynamics at the TiO_2 – Spiro-MeOTAD – dye interface as well as electron transport in the TiO_2[24,50,51].

The influence of LiTFSI on the groundstate absorption of the D102 dye is remarkable, as demonstrated by the large red shift in absorption in Figure 4.5. This red shift indicates a change in the excited state of the dye as a result of interaction with LiTFSI. This effect was investigated via combined experimental and theoretical (Density Functional Theory) work, and the reader is refered to the resulting publication for an in depth description[52]. Briefly, it was found that the excited state of the D102 dye is significantly altered by the formation of stable dye/additive complexes. Moreover, the $TFSI^-$ anion was found to be inert, while cations such as Li^+

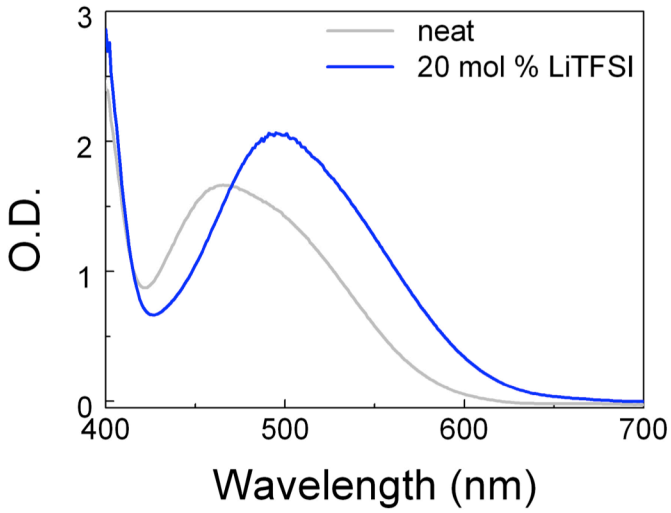

Figure 4.5. UV-vis absorption of D102 sensitized 2 µm thick mesoporous TiO_2 infiltrated with spiro-MeOTAD (with the standard *t*bp additive) incorporating 0 and 20 mol % LiTFSI. The spectra were taken immediately after spin coating to ensure that there is no contribution from the oxidized spiro-MeOTAD absorption.

and 1-Ethyl-3-methylimidazolium ($EMIM^+$) formed stable complexes, resulting in red shifts of the absorption spectrum. Interaction with cations was also predicted to result in improved coupling of the dye LUMO with TiO_2 CB states, facilitating electron transfer and explaining the remarkable improvement of J_{SC} in Figure 4.4 with LiTFSI content. This work highlighted that the dye-to-TiO_2 electron transfer rate is not only improved by the Li^+ induced negative (away from vacuum level) shift in TiO_2 surface potential, but is also improved by increased electronic coupling between two states. This effect is likely to be especially dominant in organic sensitizers with strong dipole moments such as D102, where molecular orbitals can be readily influenced by the polarity of the surroundings. Ruthenium complex dyes, however, are likely to be much less sensitive to interaction with charged species because they are themselves highly symmetric stable complexes composed of several charged species. Chapter 5 will demonstrate that a ruthenium complex dye (C106) is far less sensitive to the presence of Li^+ cations in terms of charge generation.

Disentangling the compounding effects of the lithium salts on the different interfaces and specifically its influence on charge collection is challenging. To quantify the influence of LiTFSI in more detail, transient photo-voltage and photo-current decay measurements were performed on the ssSSCs with different LiTFSI content. From these transient measurements, it is possible to extract estimates for the density of states in the TiO_2, recombination lifetime, charge collection lifetime and charge collection efficiency[53,54]. This has been discussed in detail in Chapter 3. For the devices studied here, the density of states in the TiO_2 (DOS, Figure 4.6a) becomes shallower (shifting further from vacuum) and broader as LiTFSI is added, which is consistent with Bai *et al.*[25], and is attributed to a downwards (away from vacuum) shift in TiO_2 conduction band potential. The slight broadening of the DOS has also been explained as the result of an increased number of trap states due to Li^+ intercalation into the TiO_2, where local positive charges will act as electron traps[25,55–58]. The trend observed for the DOS is consistent with the fact that the V_{oc} decreases with increasing lithium content while maintaining a constant concentration of *t*BP. Figure 4.6b shows the charge transport lifetime measured at short-circuit in the devices, which decreases with increasing LiTFSI content, in contrast to the trend in hole-conductivity in the Spiro-MeOTAD. This is not surprising, since Fabregat-

Santiago *et al.*[26] have established by impedance modelling that at the low charge densities observed at short-circuit conditions, the slow multi-trapping electron transport processes in TiO_2 limits the charge collection rate from the device. The addition of LiTFSI slows electron transport through TiO_2 as the lithium-induced surface traps broadens the DOS (as observed in Figure 4.6a) so that electrons are trapped in deeper sites, and that the detrapping rate and overall electron diffusivity are reduced[59]. This is consistent with the observations here, where a broader density of sub band gap states has increased the average trap depth at any given charge density, and not just induced a shift in surface potential. At first sight then, this trend of reduced transport rates with increasing LiTFSI content would appear to contradict a beneficial, or indeed significant influence of increasing conductivity of Spiro-MeOTAD with increasing LiTFSI content.

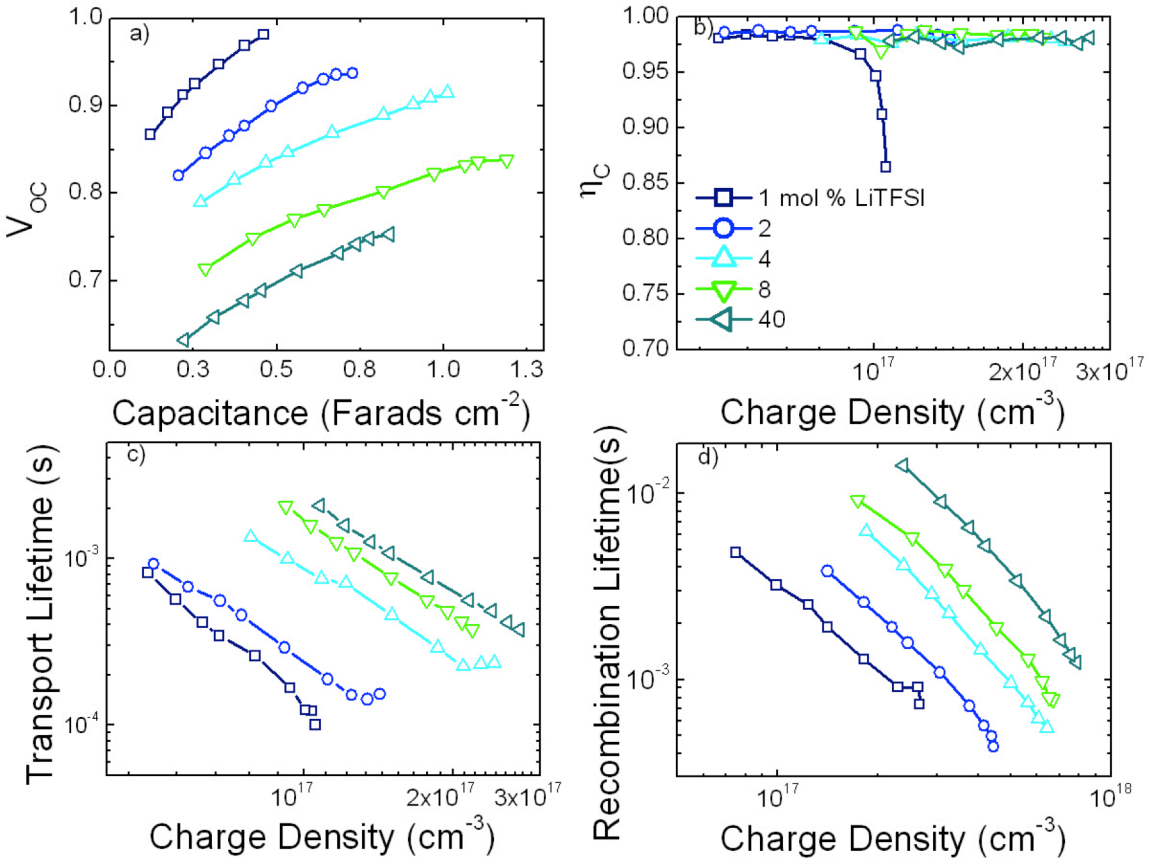

Figure 4.6. (a) Capacitance against voltage measurements for cells containing a range of LiTFSI contents. (b) Transport lifetimes at short circuit conditions, (c) recombination lifetimes at open circuit conditions and (d) the charge collection efficiency (η_C) as a function of charge density for the same devices as presented in Figure 4.4.

In addition to the slowing transport rate, the charge recombination rates appear to be similarly slowed by the addition of LiTFSI. The decrease in recombination rate has been observed before[22], and is usually attributed to the shallower DOS (leading to less driving force for electron transfer to Spiro-MeOTAD$^+$ cations as predicted by Marcus theory) as well as a "screening" of the Coulomb attraction between holes in the Spiro-MeOTAD and electrons in the TiO_2 by the high ion content[60]. For a solar cell to collect charge efficiently, the absolute rates for charge collection or recombination are unimportant, but the relative magnitude of each, and specifically much slower recombination than transport is important. The charge collection efficiency, estimated by the ratio of the transport rate over the sum of transport and recombination rates, can be found in Figure 4.6d. For most concentrations of LiTFSI the collection efficiency is 98 %, indicating close to perfect compensation of slowing down recombination rates to slowing down transport rates. At very low LiTFSI content (1 mol %), there is a very rapid decrease in charge collection efficiency with charge density. This is mainly due to a significant decrease in the electron lifetime at short-circuit conditions. This suggests that the electron-hole attraction at higher charge density cannot be effectively screened by the low ion content at the TiO_2 interface. This, together with the aforementioned influence of lithium ions on electron injection efficiency from dye to TiO_2[20,52,61] clearly explains the extremely large jump in measured J_{SC} (Figure 4.4) upon addition of a small quantity of LiTFSI. It must be noted, however, that the photocurrent generated decreases upon addition of more than 10 mol % LiTFSI, although the charge collection efficiency remains high. This suggests that addition of excess LiTFSI, and resulting high levels of oxidized Spiro-MeOTAD may actually hinder regeneration of the hole in the dye after electron injection. This could be the result of having fewer neutral Spiro-MeOTAD molecules in the vicinity of the dye and available for charge transfer, or because of an influence of high LiTFSI content on HTM pore infiltration. Further work is required to fully understand this photocurrent reduction. It must also be pointed out that based on the above results, the oxidation reaction discussed in Section 4.4 does not appear to reach completion within the timescale of device preparation and testing; ie the LiTFSI content in the HTM matrix is not completely depleted. This is especially evident when the effects of LiTFSI content on charge

collection and the TiO_2 DOS are considered in Figure 4.6, and may be the result of irreversible Li^+ intercalation into the TiO_2.

Hence, as far as charge generation and charge collection at short-circuit are concerned, it appears that a relatively low concentration of LiTFSI would be preferable. However, from the device results we observe a continuous increase in fill factor with increasing LiTFSI content, which results in the optimum concentration for efficiency being much higher that that optimised for photocurrent alone. The fill factor may be affected by series resistance losses, recombination losses at the higher charge densities experienced at forward bias, or most likely a combination of both. Based on the constantly high charge collection efficiencies of devices with optimized LiTFSI content, regardless of charge density, it seems reasonable that the charge collection efficiency will not drop dramatically at forward bias. It appears then, that a significant factor in the changing fill factors may be a change in series resistance.

4.6

Minimizing Series Resistance Losses

The fill factor of ssSSCs is determined by many factors, one of the most important of which can be the series resistance due to poor charge transport properties of the hole transporter. Although the transport at short-circuit is limited by slow electron diffusion through the TiO_2, the charge density in the film increases considerably under forward bias conditions close to the maximum power point and open-circuit. This significantly increases the effective diffusion coefficient and conductivity in the TiO_2 due to the filling of the exponential tail of trap states. Transport is then likely to be limited by hole migration through the Spiro-MeOTAD whose hole conduction is not expected to have such a strong charge density dependence when doped[26].

To specifically quantify this effect of lithium doping on the Spiro-MeOTAD on the current-voltage characteristics, we have fitted the device current-voltage curves using a one-diode model to extract the series resistance and the power losses at the maximum power point as function of the LiTFSI content (Figure 4.7)[26]. Here, the

current voltage curves were fitted numerically using the standard diode model described in Chapter 2 and setting the ideality factor to 2, using the least mean squares method on the whole J-V curve and fixing the open circuit voltage and short circuit current to match the experimental values. We note that the extracted series resistance follows a very similar trend to the conductivity of Spiro-MeOTAD, confirming that the hole transport is limiting the charge conduction in the devices at higher applied bias. This fits well with deduction by Fabregat-Santiago *et al.* from impedence spectroscopy on similar devices[26]. Indeed, it is possible to estimate an "effective" charge transport series resistance due to Spiro-MeOTAD as a function of lithium content. Here, it was approximated that 50% of the charge in the ssSSCs is generated within the first 500 nm of the devices due to the high extinction coefficient of the D102 dye used (see absorption spectra for 2 μm thick films of D102 sensitized TiO_2 films in Figure 4.5). The mean distance for holes to be collected at the silver electrode was taken to be equal to the remainder of the active area thickness (500 nm) plus the capping layer thickness (700 nm). The area through which the charge is transported is 0.09 cm^2 as defined by the solar cell mask aperture. These dimensions were used together with the resistivities of Spiro-MeOTAD at different doping concentrations to give the total resistance that could be expected through an ohmic series resistance to hole transport. The estimated values for series resistance are plotted in Figure 4.7 and are in extremely good agreement with those estimated from the ideal diode fits to the *J-V* curves.

The influence of hole transport resistance on power conversion efficiency can be readily estimated. This is accomplished by simulating *J-V* curves with all parameters identical to the one-diode fits, except that the series resistance is reduced to zero. For this analysis, the relevant J-V curves were modified to emulate the situation had there been 0 Ohms of series resistance. The voltage point at each recorded current point was simply adjusted by adding $I \times R_s$ where I is the actual current (in amps) running through the 0.09 cm^2 active area of the solar cell and R_s is the series resistance as determined by the ideal diode fit. This corrected for the voltage drop to the built in series resistance in the cell. The theoretical (0 ohms R_s) maximum power point was then determined for each LiTFSI doping level and the

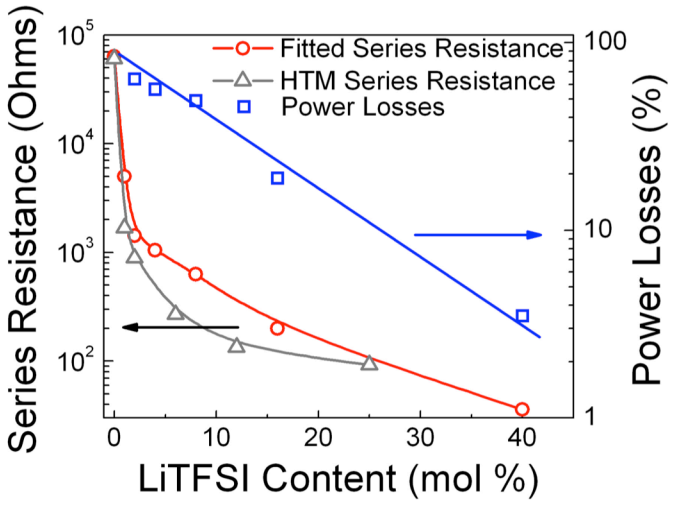

Figure 4.7. Series resistances as measured by fitting *J-V* curves to an ideal diode model (red circles), calculated series resistances from geometrical estimations using the conductivity of Spiro-MeOTAD as the only input parameter (grey triangles), and the associated power losses estimated by a simulation of the *J-V* curves without any series resistance (blue squares, right axis).

difference with the real maximum power point was taken as a percentage of the maximum theoretical power point without any series resistance.

These losses are shown in Figure 4.7, with highly significant loses for all LiTFSI contents below 16 mol %, where the losses become less than 20 %. It is evident that an effective conductivity above 10^{-5} S cm^{-1} is necessary to produce devices that are not significantly limited by a series resistance, especially once the short-circuit photocurrents are increased with next generation absorbers, and pushed towards 20 mA cm^{-2} [62,63]. In the case of LiTFSI-doped Spiro-MeOTAD, the detrimental effect of high LiTFSI concentration on the device charge transport, DOS, and charge generation results in an overall compromise for maximum power conversion efficiency. Using a higher mobility hole-transporter to enable conductivities above 10^{-4} S cm^{-1} at lower LiTFSI contents would dramatically improve the solar cell efficiency with all else being equal. It should also be pointed out that atmospheric changes in composition or temperature are likely to affect the rate and final degree of the oxidation, so that the current recipe is unlikely to be suitable for use in solar cells that are expected to maintain high performances for prolonged periods of time.

4.7

Summary and Outlook

The work presented in this chapter has made it evident that the lithium salts commonly added to organic semiconductors, specifically Spiro-MeOTAD in ssSSCs, are involved in a redox reaction, which leaves an unpaired electron in the organic matrix. The mechanism described in Section 4.4 demonstrates that the Li^+ is an efficient and stable p-dopant in the presence of oxygen. This lithium doping mechanism clarifies the dramatic increase in conductivity observed in many lithium salt – hole transporter systems, previously described in literature[7,17,64,65]. The results demonstrate that Li^+ is essential in achieving low series resistances in the solar cells, while it also facilitates photocurrent generation. The first is accomplished by oxidation of the Spiro-MeOTAD, during which lithium ions are consumed, while the latter is dependent on the availability of these ions to intercalate into the TiO_2 and influence the local polarity at the dye-sensitized heterojunction. It seems then that the current system employed in making ssSSCs is far from optimum, and that the additive is required for two opposing processes, one which consumes it and another which is dependent on its presence at the TiO_2 interface.

The lithium doping mechanism unveiled in this chapter could also explain some of the atmospheric dependencies different research groups have noted on device performance[66–68]; the atmosphere is simply reacting with organic components of the device, which can only be expected to give variable results. It should also be noted that a similar report to the one presented in this chapter was published concurrently with the work presented here by Cappel *et al.*[66], giving further support to the observed phenomena and interpretation. To move towards more stable and reproducible devices, it will be advantageous to employ different additives, one for enhancing the conductivity of Spiro-MeOTAD and another to improve charge generation at the interface. A preferable approach may even be to employ HTMs with superior hole mobilities to Spiro-MeOTAD that do not require high doping levels. This will be discussed in more detail at the end of Chapter 5, as an essential step towards achieving the fabrication of thicker ssSSCs.

4.8

References

(1) MacDiarmid, A. G. *Angew. Chem. Int. Ed. Engl.* **2001**, *40*, 2581.

(2) Burschka, J.; Dualeh, A.; Kessler, F.; Baranoff, E.; Cevey-Ha, N.-L.; Yi, C.; Nazeeruddin, M. K.; Grätzel, M. *J. Am. Chem. Soc.* **2011**, *133*, 18042.

(3) Burschka, J.; Kessler, F.; Nazeeruddin, M. K.; Grätzel, M. *Chem. Mater.* **2013**, *25*, 2986.

(4) D'Andrade, B. W.; Forrest, S. R.; Chwang, A. B.; Andrade, B. W. D. *Appl. Phys. Lett.* **2003**, *83*, 3858.

(5) Pfeiffer, M.; Leo, K.; Zhou, X.; Huang, J. S.; Hofmann, M.; Werner, A.; Blochwitz-Nimoth, J. Doped organic semiconductors: Physics and application in light emitting diodes. *Organic Electronics: physics, materials, applications*, 2003, *4*, 89–103.

(6) Leijtens, T.; Ding, I. K.; Giovenzana, T.; Bloking, J. T.; McGehee, M. D.; Sellinger, A. *ACS Nano* **2012**, *6*, 1455.

(7) Snaith, H. J.; Grätzel, M. *Appl. Phys. Lett.* **2006**, *89*, 262114.

(8) Shen, Y.; Hosseini, A. R.; Wong, M. H.; Malliaras, G. G. *Chemphyschem* **2004**, *5*, 16.

(9) Blochwitz, J.; Fritz, T.; Pfeiffer, M.; Leo, K.; Alloway, D. M.; Lee, P. A.; Armstrong, N. R. *Org. Electron. physics, Mater. Appl.* **2001**, *2*, 97.

(10) Kurata, T.; Koshika, K.; Kato, F.; Kido, J.; Nishide, H. *Chem. Commun.* **2007**, 2986.

(11) Walzer, K.; Maennig, B.; Pfeiffer, M.; Leo, K. *Chem. Rev.* **2007**, *107*, 1233.

(12) Salzmann, I.; Heimel, G.; Duhm, S.; Oehzelt, M.; Pingel, P.; George, B.; Schnegg, A.; Lips, K.; Blum, R.-P.; Vollmer, A.; Koch, N. Intermolecular Hybridization Governs Molecular Electrical Doping. *Physical Review Letters*, 2012, *108*.

(13) Fishchuk, I. I.; Arkhipov, V. I.; Kadashchuk, A.; Heremans, P.; Bässler, H. *Phys. Rev. B* **2007**, *76*, 45210.

(14) Arkhipov, V. I.; Heremans, P.; Emelianova, E. V.; Adriaenssens, G. J.; Bässler, H. *Appl. Phys. Lett.* **2003**, *82*, 3245.

(15) Arkhipov, V.; Heremans, P.; Emelianova, E.; Bässler, H. Effect of doping on the density-of-states distribution and carrier hopping in disordered organic semiconductors. *Physical Review B*, 2005, *71*.

(16) Huang, F.; Shih, P.-I.; Liu, M. S.; Shu, C.-F.; Jen, A. K. Y. *Appl. Phys. Lett.* **2008**, *93*.

(17) Abrusci, A.; Ding, I. K.; Al-Hashimi, M.; Segal-Peretz, T.; McGehee, M. D.; Heeney, M.; Frey, G. L.; Snaith, H. J. *Energy Environ. Sci.* **2011**, *4*, 3051.

(18) Xia, J.; Masaki, N.; Lira-Cantu, M.; Kim, Y.; Jiang, K.; Yanagida, S. *J. Am. Chem. Soc.* **2008**, *130*, 1258.

(19) Bach, U.; Lupo, D.; Comte, P.; Moser, J. E.; Weissortel, F.; Salbeck, J.; Spreitzer, H.; Grätzel, M. *Nature* **1998**, *395*, 583.

(20) Abrusci RSS Al-Hashimi, M Heeney, M Petrozza, A Snaith, HJ, A. K. *Adv. Funct. Mater.* **2011**, *21*, 2579.

(21) Cappel, U. B.; Smeigh, A. L.; Plogmaker, S.; Johansson, E. M. J.; Rensmo, H.; Hammarstrom, L.; Hagfeldt, A.; Boschloo, G. *J. Phys. Chem. C* **2011**, 4345.

(22) Kruger, J.; Plass, R.; Cevey, L.; Piccirelli, M.; Grätzel, M.; Bach, U. *Appl. Phys. Lett.* **2001**, *79*, 2085.

(23) Haque, S. a.; Park, T.; Xu, C.; Koops, S.; Schulte, N.; Potter, R. J.; Holmes, a. B.; Durrant, J. R. *Adv. Funct. Mater.* **2004**, *14*, 435.

(24) Tachibana, Y.; Haque, S. A.; Mercer, I. P.; Moser, J. E.; Klug, D. R.; Durrant, J. R. *J. Phys. Chem. B* **2001**, *105*, 7424.

(25) Bai, Y.; Zhang, J.; Wang, Y.; Zhang, M.; Wang, P. *Langmuir* **2011**, *27*, 4749.

(26) Fabregat-Santiago, F.; Bisquert, J.; Cevey, L.; Chen, P.; Wang, M.; Zakeeruddin, S. M.; Grätzel, M. *J. Am. Chem. Soc.* **2008**, *131*, 558.

(27) Kroeze, J. E.; Hirata, N.; Schmidt-Mende, L.; Orizu, C.; Ogier, S. D.; Carr, K.; Gratzel, M.; Durrant, J. R. *Adv. Funct. Mater.* **2006**, *16*, 1832.

(28) Snaith, H. J.; Grätzel, M. *Adv. Mater.* **2007**, *19*, 3643.

(29) Fantacci, S.; De Angelis, F.; Nazeeruddin, M. K.; Grätzel, M. *J. Phys. Chem. C* **2011**, *115*, 23126.

(30) Schafferhans, J.; Baumann, A.; Wagenpfahl, A.; Deibel, C.; Dyakonov, V. *Org. Electron. physics, Mater. Appl.* **2010**, *11*, 1693.

(31) Ouannes, C.; Wilson, T. *J. Am. Chem. Soc.* **1968**, *90*, 6527.

(32) YOUNG, R. H.; MARTIN, R. L.; FERIOZI, D.; BREWER, D.; KAYSER, R. *Photochem. Photobiol.* **1973**, *17*, 233.

(33) Anthopoulos, T. D.; Shafai, T. S. *Appl. Phys. Lett.* **2003**, *82*, 1628.

(34) Taniguchi, Y.; Miyoshi, A.; Mataga, N.; Shizuka, H.; Morita, T. *Chem. Phys. Lett.* **1972**, *15*, 223.

(35) Abdou, M. S. A.; Orfino, F. P.; Son, Y.; Holdcroft, S. *J. Am. Chem. Soc.* **1997**, *119*, 4518.

(36) Zhuo, J.-M.; Zhao, L.-H.; Png, R.-Q.; Wong, L.-Y.; Chia, P.-J.; Tang, J.-C.; Sivaramakrishnan, S.; Zhou, M.; Ou, E. C.-W.; Chua, S.-J.; Sim, W.-S.; Chua, L.-L.; Ho, P. K.-H. *Adv. Mater.* **2009**, NA.

(37) Dulub, O.; Batzilln, M.; Solovev, S.; Loginova, E.; Alchagirov, A.; Madey, T. E.; Diebold, U. *Science* **2007**, *317*, 1052.

(38) Wendt, S.; Schaub, R.; Matthiesen, J.; Vestergaard, E. K.; Wahlström, E.; Rasmussen, M. D.; Thostrup, P.; Molina, L. M.; Lægsgaard, E.; Stensgaard, I.; Hammer, B.; Besenbacher, F. *Surf. Sci.* **2005**, *598*, 226.

(39) Meyer, B. M.; Leifer, N.; Sakamoto, S.; Greenbaum, S. G.; Grey, C. P. High Field Multinuclear NMR Investigation of the SEI Layer in Lithium Rechargeable Batteries. *Electrochemical and Solid-State Letters*, 2005, *8*, A145.

(40) Furuya, K.; Ogawa, K.; Mineo, Y.; Matsufuji, A.; Okuda, J.; Erata, T. XRD studies of the insertion reaction of lithium with tin oxide and tin-based amorphous composite oxide. *Journal of Physics: Condensed Matter*, 2001, *13*, 3519–3532.

(41) MacKenzie, K. J. D.; Smith, M. E. *Multinuclear solid-state nuclear magnetic resonance of inorganic materials*; Elsevier, 2002; Vol. 6.

(42) Van Wüllen, L.; Echelmeyer, T.; Voigt, N.; Köster, T. K.-J.; Schiffmann, G. Local Li Cation Coordination and Dynamics in Novel Solid Electrolytes. *Zeitschrift für Physikalische Chemie*, 2010, *224*, 1735–1769.

(43) Mello, N. C.; Bonagamba, T. J.; Panepucci, H.; Dahmouche, K.; Judeinstein, P.; Aegerter, M. A. *Macromolecules* **2000**, *33*, 1280.

(44) Freunberger, S. A.; Chen, Y.; Drewett, N. E.; Hardwick, L. J.; Bardé, F.; Bruce, P. G. *Angew. Chemie Int. Ed.* **2011**, *50*, 8609.

(45) Kristiansen, M.; Scurlock, R. D.; Iu, K. K.; Ogilby, P. R. *J. Phys. Chem.* **1991**, *95*, 5190.

(46) Brédas, J.-L.; Beljonne, D.; Coropceanu, V.; Cornil, J. *Chem. Rev.* **2004**, *104*, 4971.

(47) Peng, Z.; Freunberger, S. A.; Hardwick, L. J.; Chen, Y.; Giordani, V.; Bardé, F.; Novák, P.; Graham, D.; Tarascon, J.-M.; Bruce, P. G. *Angew. Chemie* **2011**, *123*, 6475.

(48) Black, R.; Oh, S. H.; Lee, J.-H.; Yim, T.; Adams, B.; Nazar, L. F. *J. Am. Chem. Soc.* **2012**, *134*, 2902.

(49) Hummelshøj, J. S.; Blomqvist, J.; Datta, S.; Vegge, T.; Rossmeisl, J.; Thygesen, K. S.; Luntz, A. C.; Jacobsen, K. W.; Nørskov, J. K. *J. Chem. Phys.* **2010**, *132*, 071101.

(50) Furube, A.; Katoh, R.; Hara, K.; Sato, T.; Murata, S.; Arakawa, H.; Tachiya, M. *J. Phys. Chem. B* **2005**, *109*, 16406.

(51) Kroeze, J. E.; Hirata, N.; Schmidt-Mende, L.; Orizu, C.; Ogier, S. D.; Carr, K.; Grätzel, M.; Durrant, J. R. *Adv. Funct. Mater.* **2006**, *16*, 1832.

(52) Agrawal, S.; Leijtens, T.; Ronca, E.; Pastore, M.; Snaith, H.; De Angelis, F. *J. Mater. Chem. A* **2013**, *1*, 14675.

(53) O'Regan, B. C.; Lenzmann, F. *J. Phys. Chem. B* **2004**, *108*, 4342.

(54) Eperon, G. E.; Burlakov, V. M.; Docampo, P.; Goriely, A.; Snaith, H. J. *Adv. Funct. Mater.* **2013**, *24*, 151.

(55) Kopidakis, N.; Benkstein, K. D.; van de Lagemaat, J.; Frank, A. J. *J. Phys. Chem. B* **2003**, *107*, 11307.

(56) Tiwana, P.; Docampo, P.; Johnston, M. B.; Herz, L. M.; Snaith, H. J. The origin of an efficiency improving "light soaking" effect in SnO2 based solid-state dye-sensitized solar cells. *Energy & Environmental Science*, 2012, *5*, 9566.

(57) Tiwana, P.; Docampo, P.; Johnston, M. B.; Snaith, H. J.; Herz, L. M. *ACS Nano* **2011**, *5*, 5158.

(58) Frank, A. J.; Kopidakis, N.; Lagemaat, J. Van De. Electrons in nanostructured TiO2 solar cells: Transport, recombination and photovoltaic properties. *Coordination Chemistry Reviews*, 2004, *248*, 1165–1179.

(59) Van de Krol, R.; Goossens, A.; Meulenkamp, E. A. *J. Appl. Phys.* **2001**, *90*, 2235.

(60) Kelly, C. A.; Farzad, F.; Thompson, D. W.; Stipkala, J. M.; Meyer, G. J. *Langmuir* **1999**, *15*, 7047.

(61) Koops, S. E.; O'Regan, B. C.; Barnes, P. R. F.; Durrant, J. R. *J. Am. Chem. Soc.* **2009**, *131*, 4808.

(62) Lee, M. M.; Teuscher, J.; Miyasaka, T.; Murakami, T. N.; Snaith, H. J. *Science (80-.).* **2012**, *338*, 643.

(63) Kim, H.-S.; Lee, C.-R.; Im, J.-H.; Lee, K.-B.; Moehl, T.; Marchioro, A.; Moon, S.-J.; Humphry-Baker, R.; Yum, J.-H.; Moser, J. E.; Grätzel, M.; Park, N.-G. *Sci. Rep.* **2012**, *2*.

(64) Coropceanu, V.; Cornil, J.; da Silva Filho, D. A.; Olivier, Y.; Silbey, R.; Brédas, J.-L. *Chem. Rev.* **2007**, *107*, 926.

(65) Xia, J.; Masaki, N.; Lira-Cantu, M.; Kim, Y.; Jiang, K.; Yanagida, S. *J. Am. Chem. Soc.* **2008**, *130*, 1258.

(66) Cappel, U. B.; Daeneke, T.; Bach, U. *Nano Lett.* **2012**, *12*, 4925.

(67) Docampo, P.; Snaith, H. J. *Nanotechnology* **2011**, *22*, 225403.

(68) Weidmann, J.; Dittrich, T.; Konstantinova, E.; Lauermann, I.; Uhlendorf, I.; Koch, F. *Sol. Energy Mater. Sol. Cells* **1998**, *56*, 153.

Chapter 5

Charge Transport in Disordered Semiconductors via Transient Mobility Spectroscopy

The work presented in this chapter has been published in:

(1) Leijtens, T.; Lim, J.; Teuscher, J.; Park, T.; Snaith, H. J. Charge Density Dependent Mobility of Organic Hole-Transporters and Mesoporous TiO_2 Determined by Transient Mobility Spectroscopy: Implications to Dye-Sensitized and Organic Solar Cells. *Adv. Mater.* **2013**, *25*, 3227–3233.

(2) Crossland, E. J. W.; Noel, N.; Sivaram, V.; Leijtens, T.; Alexander-Webber, J. A.; Snaith, H. J. Mesoporous TiO_2 Single Crystals Delivering Enhanced Mobility and Optoelectronic Device Performance. *Nature* **2013**, *495*, 215–219.

(3) *Docampo, P.; *Guldin, S.; *Leijtens, T.; Noel, N. K.; Steiner, U.; Snaith, H. J. Lessons Learned: From Dye-Sensitized Solar Cells to All-Solid-State Hybrid Devices. *Adv. Mater.* **2014**

* These three authors contributed equally (statement in acknowledgements section).

5.1

Context

Due to high electronic disorder, the carrier mobility in solution-processed semiconductors tends to be highly charge density dependent. Despite this, the field of solution-processed photovoltaics has been dominated by the description of the charge transporting layers as having constant charge carrier mobilities. In addition, the solar cell architecture is also often not taken into account, despite the fact that the nanostructured geometry of ssSSCs is likely to strongly influence the charge transport properties of the charge transporting layers. In the field of ssSSCs, this has resulted in debates over which charge transporting layer (TiO_2 or HTM) is limiting the balanced charge collection in the devices, a question that had remained largely unresolved until the present work. This lack of understanding has prevented

researchers from translating their models of the device behaviour into improved efficiencies, as well as from understanding degradation pathways.

This chapter introduces a new technique, termed transient mobility spectroscopy (TMS), which employs simultaneous time resolved conductivity and absorption measurements to determine the charge density dependent mobility of several commonly employed semiconductors, in the ssSSC as well as polymer blend device structures. The findings yield new insight into the influence of the mesostructure on charge transport in organic semiconductors. The results from TMS moreover resolve the question of which charge transporting layer is limiting charge transport in optimized devices: devices are electron limited at short circuit, but hole limited at forward bias depending on the HTM hole mobility and doping level. These insights build on the previous chapter, and highlight the importance of HTM p-doping in the current state-of-the-art embodiment of ssSSCs. These findings make it possible to understand why thick (matching the optical depth of the absorber) ssSSCs have not been able to meet the expected performances. The tools developed in this chapter, together with the understanding just described, will also be invaluable when studying the degradation in charge transport pathways in ssSSCs in Chapter 7.

5.2

Introduction

Solution-processed organic semiconductors, metal oxide sol-gels and semiconductor nanoparticles are often considered very promising materials for use in light emitting diodes, transistors, and photovoltaics[1–5]. Despite the many manufacturing advantages, these materials suffer from low crystalline order, the presence of many defects and a resultantly varied potential landscape.[6–8] These properties are manifested in the material's low charge carrier mobilities, especially when compared to those in crystalline vacuum deposited inorganic semiconductors[9–12]. The presence of defects and electronic disorder results in a high density of sub gap states, such that charge transport must often occur via a trap

limited mechanism[13,14]. Charge hopping in small molecule and polymeric semiconductors, as well as trap limited diffusion in TiO_2 has already been thoroughly described in Chapter 2. In contrast to crystalline semiconductors, the charge carrier mobility in electronically disordered materials can then have a strong dependence upon the charge carrier density[6,8,15,16].

For solar cells made of these materials, such as ssSSCs and bulk heterojunction (BHJ) organic solar cells, the charge mobility is a critical parameter to understand and control. It influences important aspects of photovoltaic conversion including electron and hole separation in organics, the charge diffusion length, and series resistance losses (as described in Chapter 4)[17–20]. Furthermore, since many of these systems are not intentionally doped, the charge density may vary considerably with changing light intensity and applied electrical bias (i.e. low charge density at short-circuit and high charge density at open-circuit), making charge mobility a variable rather than a constant for any given material and photovoltaic system[7,8,13]. For transistors and light emitting diodes (LEDs), specific measurement techniques have been developed to assess the mobility under relevant working conditions. Here, the mobility can be extracted from transfer curves of field effect transistors (FETs), and from space charge limited current (SCLC) measurements in diodes[14,16,21,22]. While these techniques are applied to solar cells, specific techniques such as time-of-flight (TOF) photo-current transient and dark injection techniques have also been developed[10,22]. All have their merits, but none operate in precisely the same regime or over the same range of conditions (charge density and electric field) as exist in a solar cell under operation. In addition, the morphology in a nano to meso-structured solar cell is very different to the typical thin solid films prepared for mobility estimations via conventional techniques, introducing additional variation and uncertainty to mobility estimations. For instance, the hole mobility for poly(3-hexylthiophene) (P3HT) can vary by more than 4 orders of magnitude, depending upon the measurement method and film preparation[9,23]. Presently, the mobility in the solar cells can therefore only be estimated, and all physical analysis and subsequent modelling of current voltage characteristics are subject to a major and largely unquantifiable uncertainty.

5.3

Transient Mobility Spectroscopy

5.3.1
Method

Petrozza *et al*. have previously employed quasi-steady state photoinduced absorption spectroscopy combined with photoconductivity measurements to determine the electron mobility in dye-sensitized TiO_2[24]. In principle it is possible to determine the charge carrier mobility as a function of charge density in thin film solar cell architectures via this technique, but in practice it is a cumbersome and time-intensive experiment. Here, a new technique is introduced to facilitate the measurement of the charge carrier mobility as a function of the charge density in nano- to mesostructured photovoltaic architectures, termed "Transient Mobility Spectroscopy" (TMS). By employing TAS (described in Chaper 3) combined with time resolved photoconductivity measurements, it is possible to simultaneously measure both the photo-induced electron (hole) carrier density (n (p)), which is directly related to the magnitude of photo-induced absorption, and the conductivity (σ) of the material. This allows one to very simply calculate a mobility (μ), using

$$\mu = \frac{\sigma}{q\mathrm{n(p)}} \qquad (5.3.1)$$

over a broad range of charge densities in "one-shot". With this technique it is possible to clearly and quickly observe the charge density dependent effective mobility in polymer and molecular hole-conductors and mesoporous metal oxides within the photovoltaic operating regime and architecture.

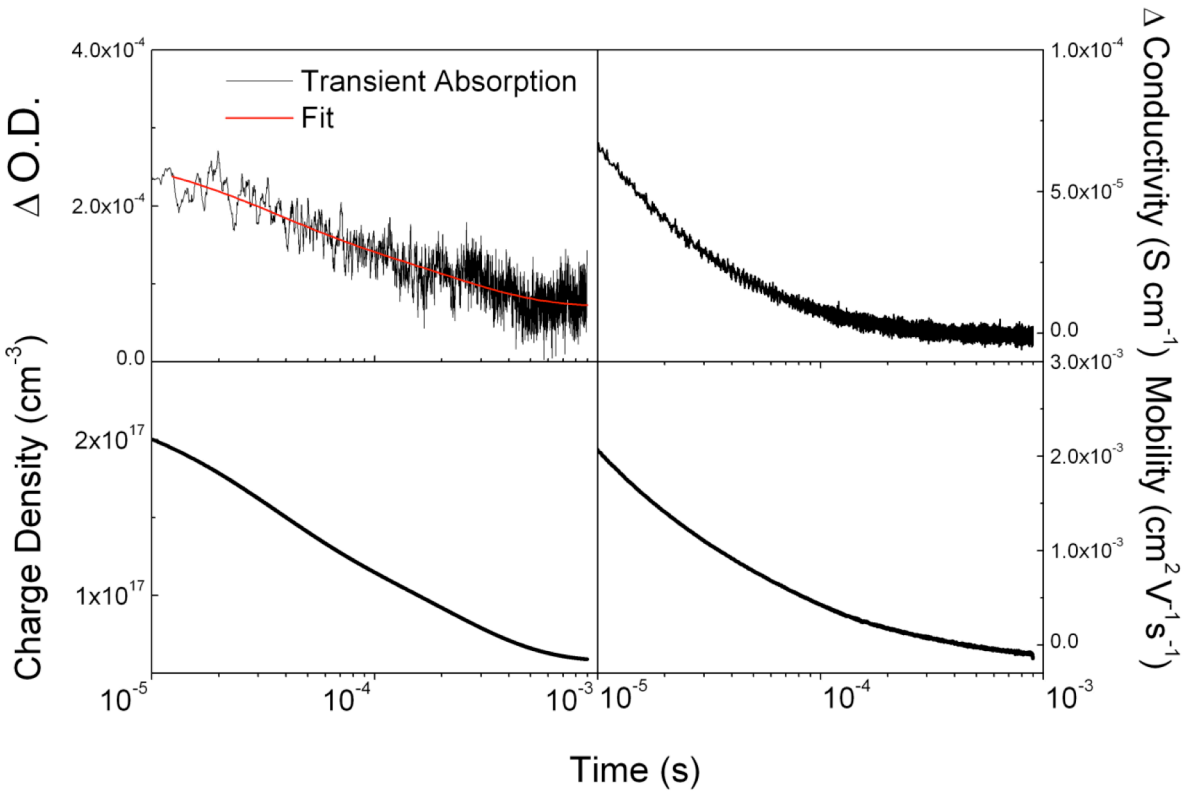

Figure 5.1. Depiction of the information gained by the method proposed here for a material with a mobility exhibiting a large charge density dependence. The TAS signal is fitted to remove the noise in the data, and then related to the charge density in the material using the extinction coefficient of the relevant charge carriers, so that the charge density is known as a function of time after the photo-excitation. The transient conductivity (after smoothing using adjacent averaging), recorded simultaneously, can then be used to calculate the mobility as a function of time, which can then of course be also considered as a function charge density.

The principles of the measurement are depicted in Figure 5.1, and are very similar to those previously proposed by Petrozza *et al.*[24]. Here, however, the measurements are time resolved, as the photoconductivity and absorption are monitored as a function of time directly after photo-excitation by a 5 ns laser excitation. Since recombination in ssSSCs tends to occur over 100s of μs, it is possible to obtain data over a range of charge density from the excitation density to zero. If a TAS probe wavelength is chosen that monitors either holes in HTM or electrons in TiO_2, the TAS signal is directly related to the photo-induced charge density. Since the photoconductivity and TAS are taken simultaneously, it is possible to know the charge density at any point along the photoconductivity decay, and Eq. 5.1 can be used to estimate the mobility at a given charge density.

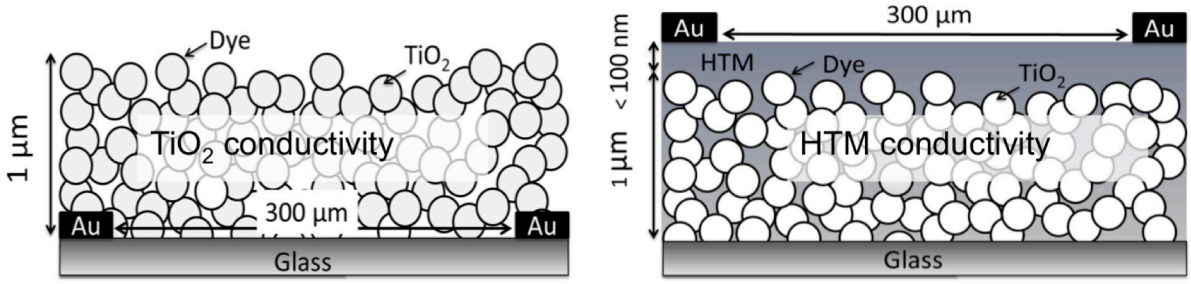

Figure 5.2. Device structure for measuring (a) electron and (b) hole conductivity in ssSSC architecture. In the case where hole transport is measured, the HTM capping layer ensures that the TiO_2 itself is not contacted, while the capping is layer is kept thin to ensure that the predominant current flow is through the active layer.

The device geometry employed for the TMS measurement is shown in Figure 5.2[25]. Typically, dye-sensitized mesoporous TiO_2 is infiltrated with p-type organic hole-transport materials. Selective contact is made to either the HTM (Figure 5.2a) by deposition of top gold electrodes, or to the TiO_2 electron transporter by deposition of gold electrodes on the glass substrate prior to printing of the mesoporous TiO_2 layer (Figure 5.2b). The devices used to measure the TiO_2 conductivity employed no HTM. This device architecture has been previously reported for estimating the conductivity in similar materials[20,24,25], and the contact resistance is negligible compared to the channel resistance for all of the materials used in this study (Chapter 3), so that the two-point probe configuration can be accurately used to estimate the bulk conductivity of the semiconductor in the active layer. The electrodes are inter-digitated to maximize the open area available for the TAS probe light transmission. It must be noted that this geometry means that the lateral conductivity is measured, but the mesostructured architecture of the ssSSCs ensures that charge transport must be isotropic.

The measurement setup is illustrated in Figure 5.3a. A suitable pump wavelength is used for photo-excitation of the sensitizing dye (550 nm) or polymer (600 nm), depending on the device architecture. As discussed in Chapter 2 and demonstrated in Figure 5.2b, the excited dye injects an electron into the TiO_2 and transfers a hole to the HTM (steps 1 and 2 in Figure. 5.3 respectively). These steps typically reach completion within 1 ns[26,27], leaving long-lived free charges with lifetimes of hundreds of microseconds to milliseconds[26,28]. In this system, light

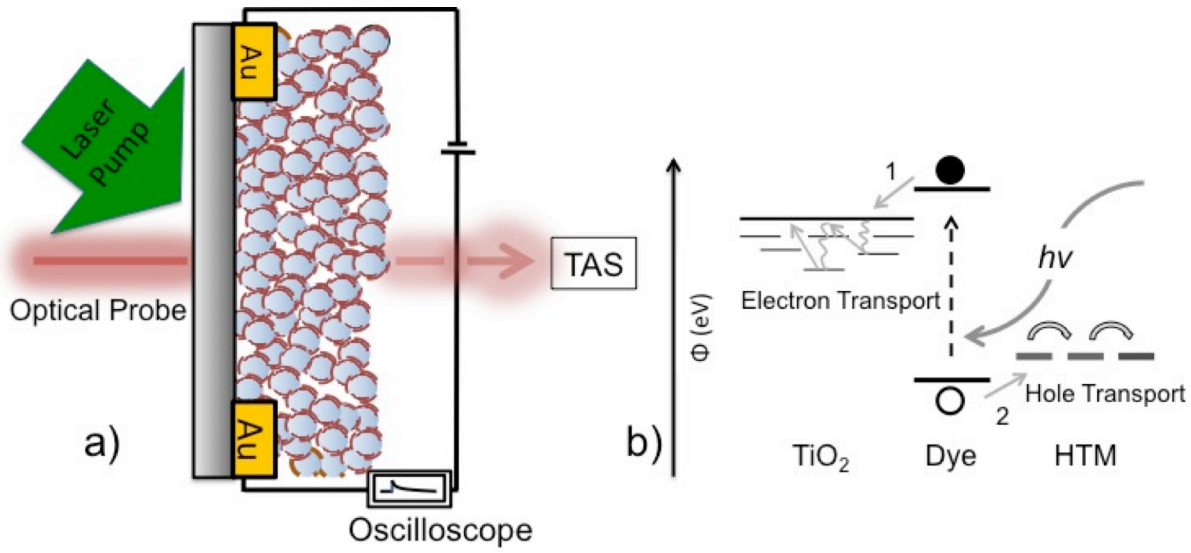

Figure 5.3. (a) Schematic of the setup used in the TMS experiments, where TAS stands for transient absorption spectroscopy and represents the optical detection system described in Chapter 3. (b) schematic of light generation, electron injection (1), and hole transfer (2), as well as charge transport in ssSSCs.

absorbing polymers have been shown to have negligible contribution to charge generation as electron injection from the polymer to the TiO_2 is inefficient[29–31]. As a result, this technique can be applied not only to Spiro-MeOTAD, but also to two light absorbing polymers, PCPDTBT and P3HT, that are commonly employed in both ssSSCs and BHJ solar cells.

5.3.2
Relating TAS signal to Charge Density

Since the oxidized states of HTMs used have characteristic absorption spectra in the visible to near infra red (NIR) region, the absorption change as a result of the laser perturbation is directly related to the density of holes in the HTMs. Where the electron conductivity in TiO_2 is measured, no HTM is used, and the absorption of the oxidized Ruthenium dye complex employed, termed C106[32], is monitored, with the assumption that every hole on the dye corresponds to one electron in the TiO_2. The C106 dye was employed because of its easily identifiable oxidized species. The oxidized HTM and dye spectra can be identified by performing quasi-steady state PIA measurements; the dominant species at the slow modulation frequency of 23 Hz are

the separated electrons and holes, so that that the PIA spectra are representative of the holes in the HTM (the electron extinction coefficient is at most ~1000 M^{-1} cm^{-1} across the wavelengths probed here)[33,34]. In the case where no HTM is employed, the electron density in TiO_2 is monitored via the hole density on the C106 dye sensitizer. PIA spectra are depicted along with the chemical structures in Figure 5.4 for all the HTMs (infiltrated into dye sensitized TiO_2) and the C106 dye in absence of HTM used in this study. The oxidized C106 dye exhibits a broad absorption feature around 700-1000 nm, the Spiro-MeOTAD exhibits the characteristic sharp peak around 520 nm as well as the broader featuers around 700 nm and further into the NIR, the PCPDTBT exhibits a ground state bleach (600-900 nm) in addition to the absorption from the polaron (900-1300 nm), as does P3HT with a ground state bleach up to 650 nm and a polaron absorption around 650-1100 nm.

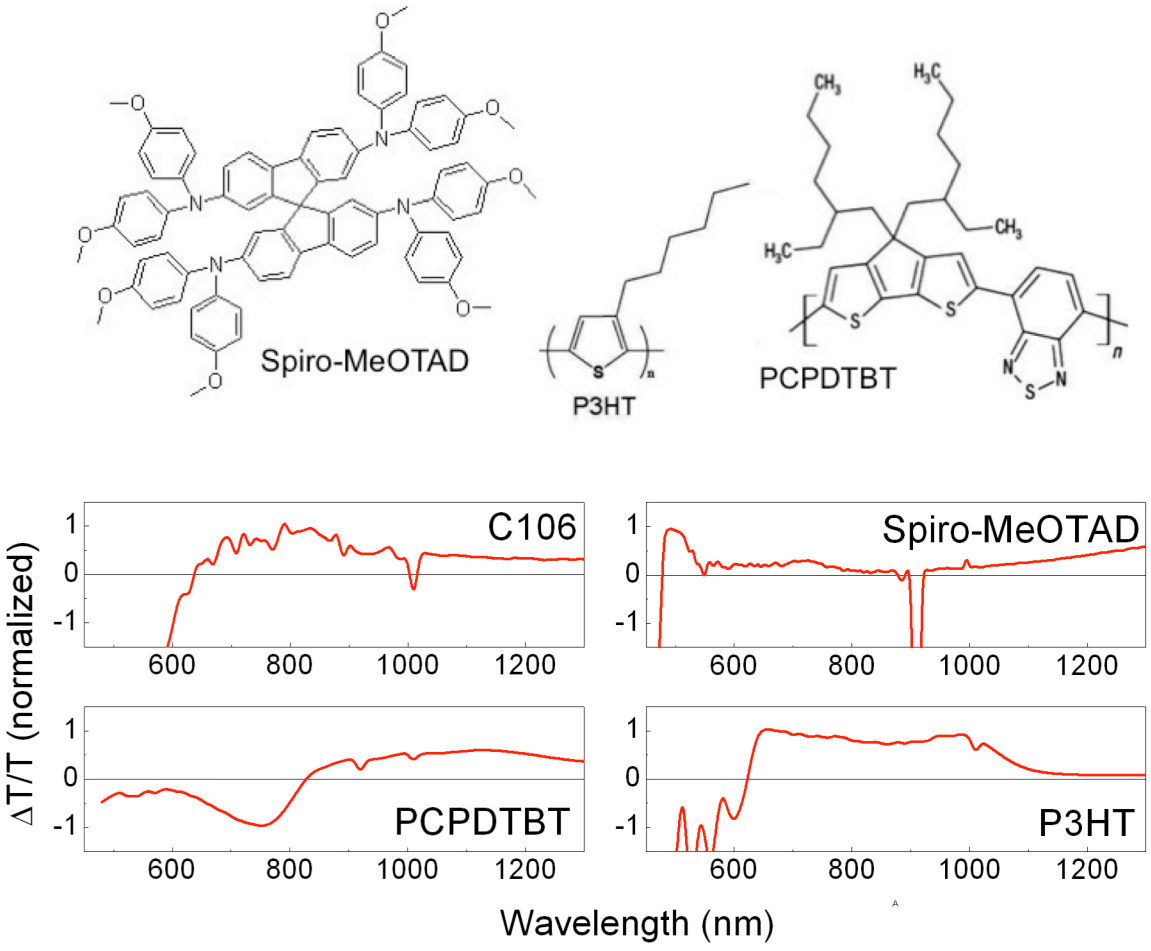

Figure 5.4. The chemical structures of the HTMs studied here are depicted above the photo-induced absorption spectra of the different HTMs in ssSSC architecture. For measuring electron transport, no HTM was used and the C106 oxidized species dominates the PIA spectrum. The samples were prepared by Jongchul Lim of the Chemical Engineering Department at Pohang University of Science and Technology, Korea.

The absence of PIA features similar to that of the oxidized C106 suggests that charge transfer from dye to HTM is complete for all the HTMs employed here, as discussed in Chapter 2. Still, to be able to accurately relate the TAS signal to charge density, the extinction coefficients of charges in ssSSCs using the different HTMs were determined experimentally. Here, simultaneous TAS and charge extraction measurements were performed at short circuit on high performance ssSSCs with semi-transparent electrodes (15 nm Au to allow enough light transmission to collect a TAS signal).

Exciting the dye sensitizer in the sample with a low intensity laser perturbation and optically probing the sample at appropriate wavelengths (where the oxidized species absorbs), it is possible to measure an absorbance change (Δ O.D.) due to the generation of separated charges in the form of oxidized HTM and dye as described in the PIA section above. The electrodes are connected in series to an oscilloscope at very low input impedance (50 Ohms), so that the device is short circuited. In this configuration, charge extraction measurements can be performed to calculate the total charge (Q) produced by the laser perturbation, while ensuring that the laser perturbation is low enough that maximum charge density after photoexcitation remains below 10^{17} cm^{-3} (fluence < 50 μJ cm^{-2}) where the charge collection efficiency is unity, as shown in Chapter 4 as well as the literature[20,35]. Example transient absorption and current extraction traces are shown in Figure 5.5. The current is integrated with time to calculate Q_M, which then gives the density of oxidized HTM or dye, depending on the system, per cm^3, which can be easily converted to a molarity. Ensuring that the collection efficiency is close to 100 % is essential in this measurement, as otherwise the integrated current will not represent all of the charge present in the system upon the initial photo-excitation. The arrow in the absorption trace shows how the maximum absorption pertubation is used to estimate the ΔA corresponding to the maximum concentration of holes in the device. Knowing the molarity (Q_M), absorbance change (ΔA) of the species being probed, and probe light path length through the sample (d), one can estimate the molar extinction coefficient (ε_A) by beer's law.

$$\Delta A = \varepsilon_A Q_M d \qquad (5.3.2)$$

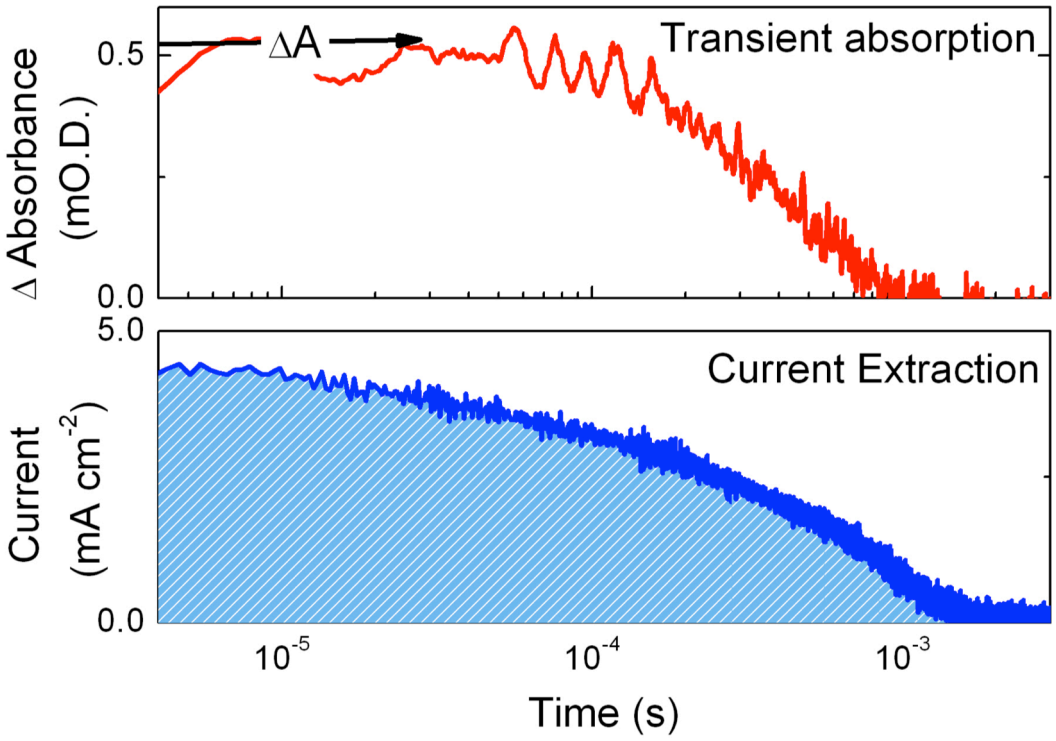

Figure 5.5. The top panel depicts an example transient absorption trace (at short circuit) of one of the solar cells used in the study, and the arrow points out the initial photo-induced absorption perturbation ΔA. Semi transparent electrodes (15 nm Au) are used to allow for significant light transmission. The bottom graph is the associated short circuit current trace. Integrating the area under the curve allows for calculation of the total charge generated within the device Q_M.

	Experimental (M^{-1} cm^{-1})	*Literature (M^{-1} cm^{-1})*
Spiro-OMeTAD$^+$ /510 nm	29,000	33,000[62]
P3HT$^+$ / 700 nm	54,000	NA
P3HT$^+$ / 980 nm	38,000	40,000[7,37]
C106$^+$ / 900 nm	NA	14,000[57]
PCPDTBT Bleach / 650 nm	39,000	NA

Table 5.1. Experimental and literature values for the extinction coefficients of the oxidized HTMs at the chosen probe wavelengths. The $C106^+$ cation could not be measured via the technique presented above, so the literature value at 900 nm was used. For PCPDTBT, the ground state bleach was used as this was the strongest feature in the PIA spectrum. For P3HT, both main absorption peaks are measured, but that at 980 nm is used for subsequent measurements.

This experiment was performed for all the HTMs used in this study. Probe wavelengths were chosen based on the PIA spectra in Figure 5.4 to ensure that a large TAS signal could be found with minimal overlap with the oxidized C106. When possible, wavelengths were chosen that are commonly used in the literature, to allow for verification of the extinction coefficients determined via the technique presented above. Table 5.1 lists the extinction coefficients for the HTMs used in this study, in ssSSC architecture, as well as the literature values at the same probe wavelengths. The values from the charge extraction experiment are notably extremely close to those available in the literature for Spiro-MeOTAD (at 510 nm) and P3HT (at 980 nm).

To measure the conductivity in the active layer during the TMS measurement, the device is connected in series with a voltage source and variable resistor (kept < 1% of the sample resistance), with an oscilloscope probing the transient voltage perturbation across the resistor, and hence transient current through the circuit.

Because the TAS measurement quantifies the change in absorbance of the sample at a given wavelength, it gives the transient photo-induced charge density Δn (Δp), but not the dark "background" charge density. The expression relating the change in conductivity due to light excitation of the sample is given in Eq. 5.3. Assuming a *charge density dependent mobility*, accurate determination of the mobility requires knowledge of the absolute charge density in the material for both light and dark conditions. The transient conductivity ($\Delta\sigma$) is defined as

$$\Delta\sigma = q\,[\mu_2 n_2\,(p_2) - \mu_1 n_1\,(p_1)] \qquad (5.3.2)$$

where μ and n (p) are the mobility and charge density before$_{(1)}$ and after$_{(2)}$ the laser perturbation. If a material has been chemically doped, as is common for the HTMs used in sDSSCs[4,20,36], n_1 will be non-negligible and difficult to determine accurately. As such, the doped materials cannot be used to accurately calculate mobilities by this method. However, in undoped materials, where $n_2 >> n_1$ such that $\Delta n(p) = n_2(p_2)$ -

$n_1(p_1) \approx n_2(p_2)$, one can simply calculate the transient mobility by the expression below.

$$\mu_2 \sim \frac{\Delta\sigma}{q\,\Delta n(p)} \tag{5.3.3}$$

The background charge density, and hence conductivity, could also be increased by "photodoping" (the photo-assisted oxidation by oxygen for example) of the organic HTM. However, the effects of photodoping of the materials used here should be negligible, since Spiro-MeOTAD, TiO_2, and PCPDTBT do not absorb strongly at the excitation wavelength of 550 nm, and the light is predominantly absorbed by the C106 sensitizer[4,29,37]. In the case of P3HT, which may compete with the dye for light absorption to form P3HT-O_2 charge transfer complexes, it has been previously shown that the hole mobility is not affected by prolonged (hours) laser light excitation between 500 and 600 nm in air. Additionally, the background conductivity was not observed to significantly increase during the measurements presented here[38].

5.4

Charge Transport in ssSSCs

The effective mobilities of the neat (undoped) materials are plotted as a function of charge density in Figure 5.6. It is only possible to extract an "effective mobility" in the sample geometry used here, where the film thickness is taken to be the entire mesoporous film and hence, the mobility extracted is that in the composite (TiO_2, HTM and air). While this will differ somewhat to the mobility of the solid neat material, this effective mobility is most relevant to charge collection during solar cell operation.

In the case of TiO_2, the mobility shows the expected strong charge density dependence, approaching 6×10^{-3} cm^2 V^{-1} s^{-1} at a charge density around 2×10^{17} cm^{-3}, agreeing with previous values from previous steady-state measurements of dye-sensitized TiO_2 around 10^{-3} cm^2 V^{-1} s^{-1} at similar charge densities[24,39]. In ssSSC architecture, the HTM mobilities also show significant dependencies on the charge carrier density, as is expected for disordered organic semi-conducting materials[8,15]. The hole mobility of Spiro-MeOTAD increases from 10^{-5} to high 10^{-4} cm^2 V^{-1} s^{-1} values with an increase in charge density to 3×10^{17} cm^{-3}. This explains the variation in hole mobility previously reported in the literature for this material, and fits well with the work done by Poplavskyy *et al*. where TOF measurents have given values within this range depending on the electric field[10,40,41]. The P3HT (in ssSSC architecture) mobility shows a comparatively smaller yet substantial charge density dependence, and displays higher mobilities of around 10^{-3} cm^2 V^{-1} s^{-1}, which corresponds to some of the lower mobility values reported in literature for this material obtained via FET measurements[23]. The mobility for P3HT in a blend architecture with only 5 % $PC_{60}BM$ is provided in the inset as a reference for an ideal configuration with a fairly constant mobility. This will be discussed in full in a subsequent section. The mobility of PCPDTBT is higher than that of Spiro-MeOTAD but lower than that of P3HT,

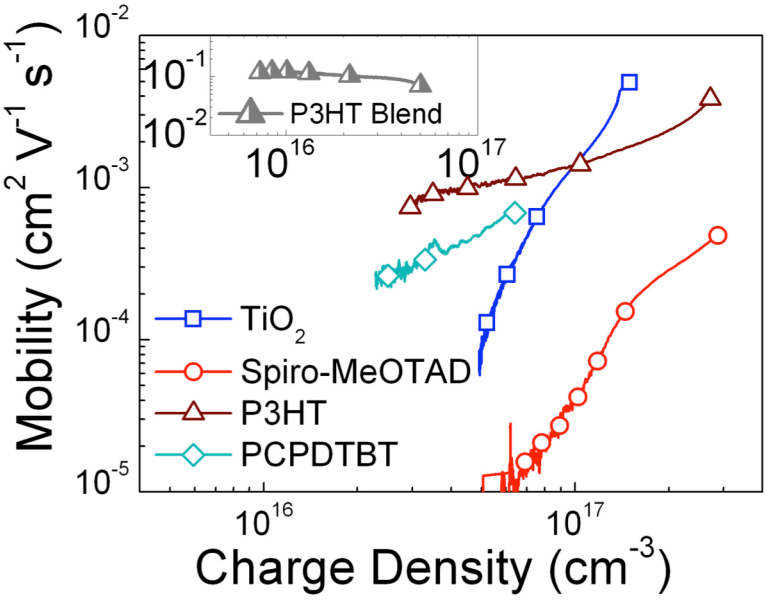

Figure 5.6. The effective mobility, derived by the TMS technique, is plotted as a function of charge density in ssSSC architecture. The inset gives the effective mobility of P3HT in an ideal morphology: a photoactive blend with only 5 weight % $PC_{60}BM$, annealed in a glovebox, as a reference with a fairly constant mobility. The samples were prepared by Jongchul Lim of the Chemical Engineering Department at Pohang University of Science and Technology, Korea.

approaching 10^{-3} cm^2 V^{-1} s^{-1} at higher charge densities, again matching the lower reported values in the literature from FET measurements[42,43]. The low values for the polymers correspond to those normally associated with films of poor crystallinity[9,23,42,43], likely due to the mesoscopic architecture, which could prevent the formation of large crystal domain sizes, and result in significantly less than 100% pore filling of the mesoporous TiO_2[37]. The above results demonstrate that the mobilities of all the materials used in this study show significant charge density dependencies in ssSSC architecture within the relevant charge density regime. Thus, the technique reported here provides unique and valuable insights directly relevant to charge transport in solar cell configuration. A surprising finding, with respect to ssSSCs, is that the electron mobility in the TiO_2 is significantly higher than the hole-mobility in neat Spiro-MeOTAD over the entire operating regime.

In order to understand the operation of the solar cell, it is relevant to raise the notion of ambipolar charge transport in the photoactive layer of a ssSSC and the concept of "ambipolar mobility" (μ_A). Since the photocurrent in a solar cell is ambipolar, the rate of flow of charge through the device is directly influenced by both the mobilities (or diffusion coefficients) for electrons and holes (μ_n and μ_p respectively) and the respective charge densities (n and p)[44,45]. To satisfy current continuity,

$$\mu_A = \frac{n\mu_n\mu_p - p\mu_p\mu_n}{n\mu_n + p\mu_p} \qquad (5.4.1)$$

Hence, a balanced collection rate for electron and holes, as is required for current continuity, can be achieved by either having matched mobility or by having significantly greater electron or hole densities to compensate for a lower mobility of either carrier. μ_A most closely reflects either μ_n or μ_p depending upon whether the product of $n\mu_n$ or $p\mu_p$ is smaller. i.e. if $n\mu_n << p\mu_p$ then $\mu_A \sim \mu_n$ and the solar cell could be considered to be "electron limited". It is now insightful to consider the conductivity ($\sigma = q\mu n(p)$) of the HTMs at a given photo-induced charge density in relation to the conductivity of the TiO_2.

The conductivity of the materials versus charge density is plotted in Figure 5.7, for the HTMs with and without the LiTFSI and *t*BP additives (denoted by (A) in the legend). It must be noted here that the charge density values on the x-axis are not the absolute charge density values for the LiTFSI doped materials (A), but the photo-induced charge density, since the LiTFSI tends to p-dope the HTMs (Chapter 4)[20,46]. As expected, adding LiTFSI increases the conductivity of all of the HTMs significantly, with doped P3HT reaching extremely high conductivities of 10^{-2} Scm^{-2}, PCPDTBT reaching 10^{-3} Scm^{-2}, and Spiro-MeOTAD approaching 10^{-4} Scm^{-2} at the higher charge densities. The doped HTMs show very constant conductivities over this range of photo-induced charge density, which can be explained by these materials' doping-induced free hole density being higher than the photo-induced hole density. The neat HTMs show extremely low conductivities at low charge densities, but increase with photo-induced charge density. LiTFSI is known to intercalate into TiO_2 to lower the quasi Fermi level of the free electrons by inducing sub bandgap states, resulting in a decrease in mobility, explaining the lower conductivity observed for the LiTFSI and *t*BP treated TiO_2[47,48]. The flattening of the slope and slightly higher conductivity at low charge densities may be due to a mild n-doping of the lithium treated TiO_2 by facilitating the formation of oxygen vacancies[49].

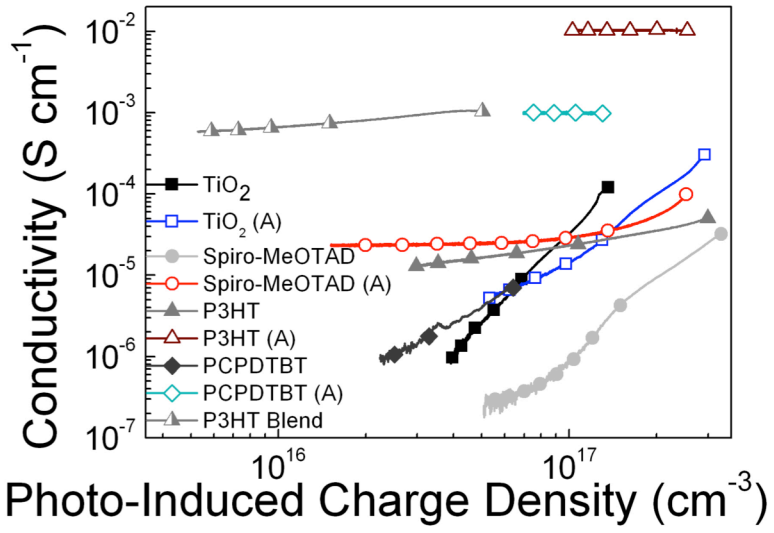

Figure 5.7. The conductivity of the various materials is displayed, with and without the standard LiTFSI and *t*bp additives (A), as a function of photo-induced charge density. The coloured data with open markers represent the conductivities with additives, ie the configuration used in the best ssSSCs. The samples were prepared by Jongchul Lim of the Chemical Engineering Department at Pohang University of Science and Technology, Korea.

While the mobility of TiO_2 is much higher than that of Spiro-MeOTAD, the conductivities with the additives present are more comparable due to the p-doping of Spiro-MeOTAD with LiTFSI. From the discussion of the ambipolar mobility above, it is evident that at the low charge density regime found at short-circuit conditions ($< 2 \times 10^{17}$ cm^{-3})[20,50], the low TiO_2 conductivity will limit charge conduction in the solar cells for all combinations of materials except that of the undoped Spiro-MeOTAD and possibly the undoped PCPDTBT. This is consistent with what has been reported for standard ssSSCs made using P3HT and Spiro-MeOTAD doped with LiTFSI: charge collection at short-circuit appears to be limited by the slow electron diffusion through TiO_2. However, it is evident that for all material combinations except the doped P3HT and doped PCPDTBT, the large increase in TiO_2 conductivity results in the HTM limiting the charge transport at the high charge densities ($> 2 \times 10^{17}$ cm^{-3}) that would be found at forward bias in ssSSCs. While it has previously been speculated that the charge transport close to open-circuit conditions is limited by the HTM[51], this work gives the first quantitative evidence for this phenomenon, and it is possible to resolve at which photo-induced charge density the cross-over from electron- to hole-limited conduction is likely to occur. Moreover, it is clear that this is dependent on the HTM used, and that in the case of doped PCPDTBT and P3HT, the conductivities remain higher than that of the TiO_2 over the entire range of charge densities, so that TiO_2 will be transport-limiting at all points of device operation. These results give additional insight into the importance of doping of low mobility HTMs in ssSSCs, and indeed indicate that doping of the TiO_2 to enhance the electron conductivity could be useful when combined with higher conductivity polymers.

5.6

Mobility of P3HT in polymer blends

To demonstrate the versatility of TMS, identical measurements to those reported above were performed on bulk heterojunction architectures employing blends of P3HT as the light absorbing hole conductor with 5-10 wt % of $PC_{60}BM$ as the electron acceptor. Keeping the $PC_{60}BM$ content this low ensures that any in-plane charge conduction is through the P3HT, but it is high enough to enable

significant charge separation[52]. The mobility for blends with 5 and 10 wt %, with and without annealing, are presented in Figure 5.8. The devices were spin-coated on glass, some were annealed at 150 °C, and sealed in a nitrogen atmosphere (< 1 ppm oxygen). The measurements were then performed as before, where the P3HT was excited at 600 nm (tail of the absorption) to obtain close to uniform charge generation throughout the film depth. Since the absorption profile of the P3HT polaron in this blend may differ from that in the sDSSC, the literature value of the polaron extinction coefficient at 980 nm is used, which is very close to the experimental value obtained here via the charge extraction method. The charge density regime obtained here is somewhat lower than what was obtained for the ssSSCs, but this is only natural, as this is a sub-optimal system where charge separation is not expected to be unity. Going much lower in charge density is also not possible because of the limits in signal to noise ratio of the setup. Still, the charge density regime corresponds to what is commonly reported to be relevant in P3HT:$PC_{60}BM$ solar cells[7].

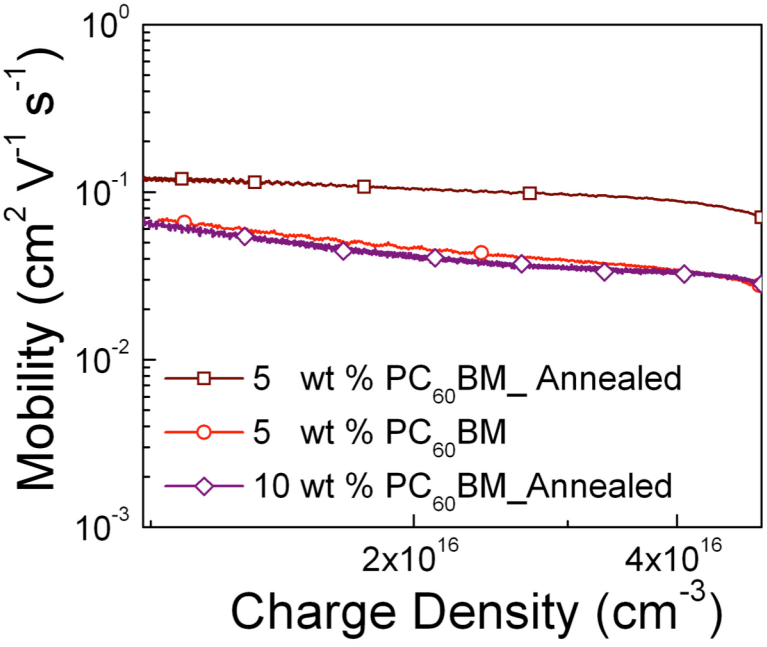

Figure 5.8. The effective mobility in P3HT:$PC_{60}BM$ BHJ architecture is presented for two different weight concentrations of the acceptor (5 and 10 wt %). For the 5 wt % samples, the effect of annealing at 150 °C (in an N_2 filled glovebox) was also evaluated. Note that the mobilities are relatively constant with charge density, as opposed to the samples prepared in ssSSC architecture presented in Figure 5.6. Data is shown for charge densities between 10^{16} and 5×10^{16} (cm^{-3}) because higher charge densities could not be obtained with the laser excitation used here (600 nm at 50 μJ cm^{-2}), likely due to incomplete charge separation in the blends with low $PC_{60}BM$ concentrations.

The mobility of the P3HT in this annealed thin film configuration is found to be 0.1 $cm^2\ V^{-1}\ s^{-1}$ (also shown as an inset in Figure 5.6). Not surprisingly, this is significantly higher than that found in the ssSSC architecture, and matches previously reported values for thin film crystalline P3HT from FET measurements[9]. The relatively constant nature of the mobility versus charge density is an indication of the high degree of crystallinity of P3HT in this configuration, and suggests a very low trap density. The conductivity, as shown in Figure 5.7, increases with increasing charge density, confirming that the material was not significantly p-doped. The slight decreasing slope of carrier mobility (< factor 2 over half a decade in charge density) could be due to unintentional doping or defect levels raising the conductivity of the neat material. This must be relatively minor however, as evidenced from the almost perfectly linearly increasing slope of conductivity with charge carrier density. Comparing these mobility values to those obtained for P3HT in the mesoporous architecture then highlights the importance of morphology on charge carrier mobility and demonstrates that the mesoscopic disorder inherent in the ssSSC architecture is far from ideal when using polymer HTMs, confirming what has been previously reported by McGehee *et al.*[23,53]. The effective mobility is expected to decrease with increased $PC_{60}BM$ content, as has been previously reported[54], and this is observed in Figure 5.8 as the $PC_{60}BM$ content is increased from 5 to 10 wt % with the mobility decreasing by approximately a factor of 2-3. This is more than can be accounted for by considering that the P3HT content has decreased from 95 to 90 wt %. Similarly, not annealing 5 wt % films results in a 2-3 fold decrease in mobility, confirming the importance of annealing protocols on crystallization in P3HT fims[54]. Finally, it should be noted that the mobility here is measured laterally, which is the preferential direction of charge transport for P3HT films as the polymer chains tend to align along the horizontal plane[9]. The work done here confirms observations often made in the field of BHJ solar cells, and demonstrates that the TMS technique is effective for use in both ssSSC and BHJ architectures.

5.6

Implications to ssSSC performance

To further correlate these measurements to solar cell device characteristics, a series of ssSSCs with HTM compositions identical to those used for the TMS measurements were prepared. *J-V* (curves under simulated sun light) are plotted in Figure 5.9, with the inset showing the series resistance for the device close to open-circuit, as determined by fitting the *J-V* curve to an ideal diode model. Extracting the series resistance was performed as in Chapter 4. It is evident that the LiTFSI and *t*BP additives are essential for good device performance in Spiro-MeOTAD and PCPDTBT based devices, while the P3HT devices seem to function moderately well even in the absence of doping. The reason for the lower short-circuit photocurrents achieved for the "doped" P3HT and PCPDTBT devices is likely to be the result of the parasitic absorbance of the polymers, since their absorption spectra overlap with that of the C106 sensitizing dye, but the excited polymers cannot undergo efficient charge transfer at the TiO_2 interface[29,31,37]. There are a plethora of influences the ionic additives have on charge generation and recombination, which have been discussed in Chapter 4[20,28,55–57]. In the case of this ruthenium dye, however, one of the dominant

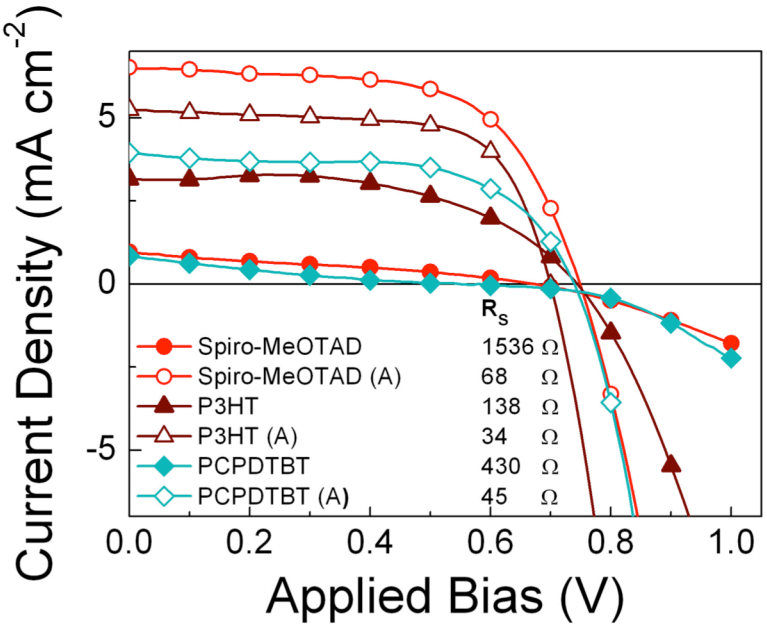

Figure 5.9. *J-V* curves for ssSSCs employing the various HMTs with and without the standard LiTFSI and *t*bp additives. The legend also denotes the series resistance of the different configurations at forward bias, arrived at by fitting to the ideal diode model as described in Chapter 4. The data with open markers denotes the use of additives. The samples were prepared by Jongchul Lim of the Chemical Engineering Department at Pohang University of Science and Technology, Korea.

effects of the lithium salt shown here is to reduce the series resistance to charge transport (estimated around open-circuit), and that the relative series resistances in the devices follow an identical trend to what is found for the conductivities at high charge density in Figure 5.8.

$$\sigma_{\text{neat spiro}} < \sigma_{\text{neat PCPDTBT}} < \sigma_{\text{neat P3HT}} < \sigma_{\text{doped spiro-OMeTAD}} < \sigma_{\text{doped PCPDTBT}} < \sigma_{\text{doped P3HT}}$$

Notably, the series resistance for the doped P3HT device is only marginally, and not orders of magnitude, lower than the doped Spiro-MeOTAD device, consistent with the P3HT device being electron-limited by the conduction through the TiO_2 at forward bias.

P3HT-based devices perform remarkably well in the absence of any additives. The higher photocurrent in the presence of the additives is likely to be due to the effect of the lithium ions on charge generation, separation, and recombination at the TiO_2 interface[28,55]. The undoped Spiro-MeOTAD and PCPDTBT devices, however, only generate approximately 1 mA cm^{-2} in the absence of additives. Since the undoped P3HT-based devices deliver approximately 3 mA cm^{-2}, the poor performance of the undoped Spiro-MeOTAD and PCPDTBT devices is not due solely to poor electron injection rates, but to the extremely low HTM conductivity in the low charge density regime. Since the charge density changes by approximately an order of magnitude from open-circuit to short-circuit, the hole mobility drops by an order of magnitude, and hence the series resistance in the solar cell may change by more than two orders of magnitude going from open- to short-circuit. This will clearly lead to series resistance limited *J-V* characteristics (even though the *J-V* curve may not look linear) where charges recombine before they are extracted. This is a new insight into the operation of ssSSCs and fully elucidates why doping is essential for attaining high performance Spiro-MeOTAD based devices. The findings here also complement the findings of Chapter 4, where the importance of HTM conductivity on the series resistance and FF was established, but the influence on the short circuit current still not completely understood and mostly ascribed to changes in charge generation and recombination dynamics. The work presented here, however, demonstrates that while the additives do influence charge generation and recombination, by far the most significant influence is that of raising the conductivity of the HTMs to enable

efficient charge collection. This, of course dpends on which sensitizer is used; where electron transfer from D102 for example benefits more from LiTFSI than from C106 due to differences in polarizability.

5.7

Lessons Learned for Thick ssSSCs

The work presented in the last two chapters demonstrates the importance of p-doping the commonly used Spiro-MeOTAD HTM for high performance ssSSCs. Making thicker devices to match the absorption depth of most commonly used sensitizing dyes, a goal of a great deal of recent research[27,40,58–60], will result in series resistance issues becoming even more paramount. Indeed, to successfully make thicker ssSSCs, higher LiTFSI contents have often been employed, although the reason why was not completely understood[40,58]. The understanding gained in this thesis thus far has however elucidated the roles of LiTFSI. It is now possible to

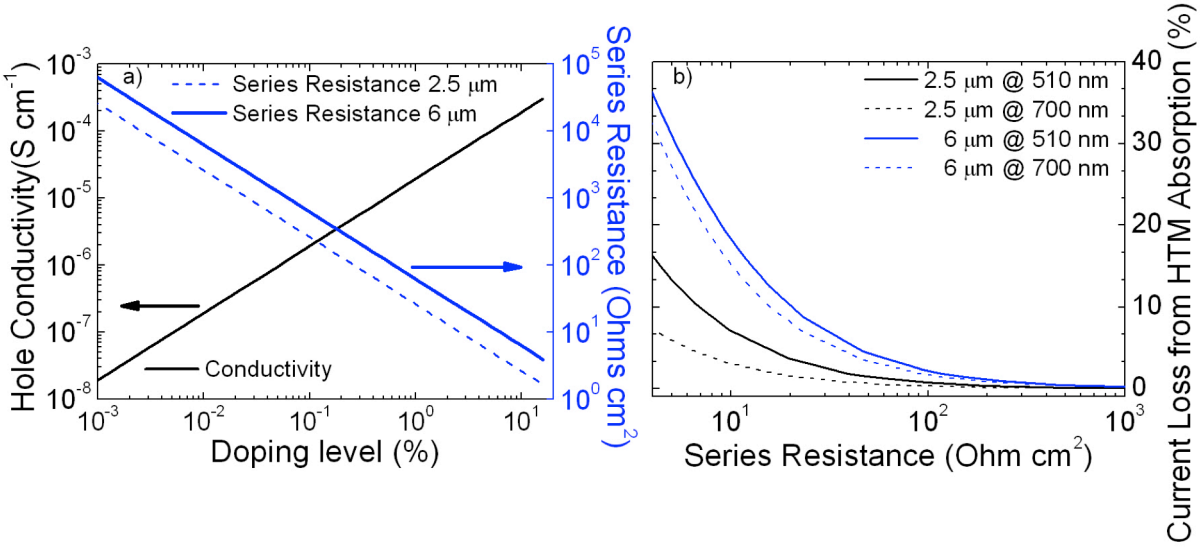

Figure 5.10. (a) Depiction of the hole conductivity (left axis) and resulting series resistance (in Ohms cm^2) in both 2.5 and 6 μm thick ssSSCs as a function of the doping density, assuming a constant hole mobility of 10^{-4} cm^2 V^{-1} s^{-1} for Spiro-MeOTAD. It is clear that to maintain a suitably low series resistance (< 10 Ohms cm^2) in thick films, doping levels of several mol % are required. (b) Here the loss in photo-current due to parasitic absorption is plotted as a function of the series resistance for the same two device thicknesses at both 510 and 700 nm, using the doping levels from (a) and the known extinction coefficients of oxidized Spiro-MeOTAD along with the known extinction coefficients of the commonly used Z907 dye[61]. This is a very rough estimation, and does not take the losses due to the HTM capping layer into account, making the current losses an under estimate.

propose a pathway to attaining higher performance thick ssSSCs.

Perhaps the most important factor that has been overlooked in past research is the fact that p-doped (oxidized) Spiro-MeOTAD absorbs strongly with peaks around 500 and 700 nm. As a result, the oxidized HTM will compete with the dye for light absorption. This has been briefly discussed in a recent work by Margulis *et al.*[61], but implications to charge transport and improving thick ssSSC device performance were not explored. Because thicker devices will be more limited by series resistance in the HTM, the HTM will need to be more highly doped, resulting in an increase in parasitic absorption.

Figure 5.10 gives a rough estimation of the interplay between desired doping levels and photo-current losses due to parasitic absorption. Knowing the extinction coefficient of oxidized Spiro-MeOTAD from this work and from the literature[62], as well as that of a commonly employed ruthenium complex dye Z907[61], it is possible to estimate the amount of light absorbed by the dye and the oxidized HTM as a function of doping concentration. First, an estimate of the relationship between the doping level and the material conductivity must be established. For simplicity, a constant mobility of 10^{-4} was assumed for Spiro-MeOTAD. This is because the mobility found here for neat Spiro-MeOTAD is likely to be different from that in the highly doped material, and 10^{-4} is a reasonable approximation of the mobility as displayed in Figure 5.6. It is then simple to calculate the conductivity as a function of doping density, using the same relation that has been applied throughout the text (Eq. 5.3.1). Assuming that the holes must travel, on average, half the device thickness to reach the cathode (this is an underestimation that assumes a constant charge generation profile in the device), the expected series resistance due to hole transport is calculated as a function of doping level. Here, the same procedure was used as described in Chapter 4.

To estimate the percentage of photo-current lost to parasitic absorption, the extinction coefficients of the sensitizer and oxidized HTM species must be known. The extinction coefficient of oxidized Spiro-MeoTAD at 510 nm has been determined in this work, while that at 700 nm is taken from the literature (the charge extraction experiments presented above show that the literature values are applicable to the

ssSSC device architecture). The commonly employed Z907 dye is used for the analysis, because it is a high performance dye in thick DSSCs using liquid electrolytes, with an absorption tail into the NIR part of the solar spectrum[63]. As such, a dye like Z907 would be an ideal candidate for making thick ssSSCs with high photo-currents. The extinction coefficients for the dye are taken from recently published work by Margulis *et al*.[61]. To model how much light is absorbed by the oxidized HTM as opposed to the dye, the extinction coefficients are converted into an effective absorption cross-section in terms of ssSSC film thickness. The absorption in the composite is then approximated as going through alternating 25 nm thick sections of HTM and TiO_2/dye. The difference between how much light is absorbed by the dye composite in presence and absence of doped HTM is divided by the amount of light absorbed in absence of doped HTM to give the percentage of photo-current lost to parasitic absorption. Since the relation between doping density and the device series resistance has already been established, it is trivial to then plot the percentage of photo-current lost to parasitic absorption as a function of series resistance in the device, as is done in Figure 5.10b. A series resistance of less than 10 Ohms cm^2 (corresponding to 100 Ohms in the device configuration used here) is required to minimize series resistance losses, as described in Chapter 4. To achieve such a low series resistance, however, high doping levels must be used, especially in thick films. This comes at the cost of parasitic absorption, which begins to cause losses of over 20 % at both 510 and 700 nm, and much more so for thicker ssSSCs. This analysis then demonstrates that using HTMs with low mobility, requiring high doping levels to minimize series resistance, limits the possibility to make devices thicker because parasitic absorption becomes more and more dominant. With recent work demonstrating that charge diffusion lengths (at short circuit)[35] and HTM pore filling[60,62] do not limit the device thickness, the work presented here may give the breakthrough in understanding required to finally realize thick ssSSCs with high light harvesting efficiencies.

5.8

Summary and Outlook

Transient Mobility Spectroscopy (TMS) has been developed to determine the conductivity and mobility of a variety of material composites commonly used in organic based photovoltaics in device-like thin film mesostructured architectures, over the relevant range in charge carrier density. The mobility of the materials commonly used in ssSSCs is heavily dependent on the charge carrier density as well as the morphology. By comparing the conductivity of the materials as a function of charge density, it is possible to identify which charge transporting component in ssSSCs is "transport limiting" at a given charge density and hence any point on the solar cell *J-V* curve. It is evident that in the current state of the art ssSSCs employing Spiro-MeOTAD, the HTM is heavily doped but still limits charge transport at charge densities found at forward bias. p-Type doping of low mobility ($< 10^{-4}$ cm V^{-1} s^{-1}) HTMs is essential for effective solar cell operation, but the higher mobility organic semiconductors such as P3HT do not necessitate doping. Indeed, for further improvements with higher mobility polymers, enhanced conductivity in the TiO_2 is required. This also suggests that a route towards dopant free ssSSCs will require the development of new HTMs with high hole mobilities ($> 10^{-3}$ cm V^{-1} s^{-1}). Being able to develop dopant free ssSSCs would be beneficial for maintaining long-term and thermally stable charge transport characteristics in the HTM. As it stands, the reactive nature of the LiTFSI dopant means that the charge transport characteristics of the HTM are likely to fluctuate with atmospheric conditions, with clear repercussions to the device series resistance and performance.

The work from Chapters 4 and 5 has highlighted the paramount importance of HTM doping in the best performing ssSSCs. For ssSSCs to be able to compete with conventional photovoltaic devices such as Si and GaAs based devices, however, they will simply have to be able to improve in light harvesting efficiency. This can be done by making the devices thicker, so that they absorb more light. This has been predicted to be possible, as recent findings suggest that neither pore filling nor the charge diffusion length limit the performance of thick ssSSCs. The work presented in Chapter 4 and 5, and specifically the estimations presented in Section 5.7,

demonstrate that parasitic absorption becomes more and more important in thicker films as the doping level in the HTM is increased to minimize the series resistance. This is a new insight, and gives clear direction for future work: HTMs with higher mobilities must be found that require less doping and exhibit less parasitic absorption to realize high efficiency thick ssSSCs. Alternatively, more strongly absorbing dyes could be used that do not necessitate thick active layers.

5.9

References

(1) Sirringhaus, H.; Tessler, N.; Friend, R. H. *Science (80-.).* **1998**, *280*, 1741.

(2) Greenham, N. C.; Moratti, S. C.; Bradley, D. D. C.; Friend, R. H.; Holmes, A. B. **1993**.

(3) Yu, G.; Gao, J.; Hummelen, J. C.; Wudl, F.; Heeger, A. J. *Sci. Pap. Ed.* **1995**, *270*, 1789.

(4) Bach, U.; Lupo, D.; Comte, P.; Moser, J. E.; Weissortel, F.; Salbeck, J.; Spreitzer, H.; Grätzel, M. *Nature* **1998**, *395*, 583.

(5) O'Regan, B.; Grätzel, M. *Nature* **1991**, *353*, 737.

(6) Fishchuk, I. I.; Arkhipov, V. I.; Kadashchuk, A.; Heremans, P.; Bässler, H. *Phys. Rev. B* **2007**, *76*, 45210.

(7) Shuttle, C. G.; Hamilton, R.; Nelson, J.; O'Regan, B. C.; Durrant, J. R. *Adv. Funct. Mater.* **2010**, *20*, 698.

(8) Snaith, H. J.; Grätzel, M. *Phys. Rev. Lett.* **2007**, *98*, 177402.

(9) Sirringhaus, H.; Brown, P. J.; Friend, R. H.; Nielsen, M. M.; Bechgaard, K.; Langeveld-Voss, B. M. W.; Spiering, A. J. H.; Janssen, R. A. J.; Meijer, E. W.; Herwig, P. *Nature* **1999**, *401*, 685.

(10) Poplavskyy, D.; Nelson, J. *J. Appl. Phys.* **2003**, *93*, 341.

(11) Sze, S. M.; Irvin, J. C. Resistivity, mobility and impurity levels in GaAs, Ge, and Si at 300°K. *Solid-State Electronics*, 1968, *11*, 599–602.

(12) Holliday, S.; Donaghey, J. E.; McCulloch, I. *Chem. Mater.* **2013**, *26*, 647.

(13) Blom, P. W. M.; de Jong, M. J. M.; van Munster, M. G. *Phys. Rev. B* **1997**, *55*, R656.

(14) Tanase, C.; Meijer, E. J.; Blom, P. W. M.; de Leeuw, D. M. *Phys. Rev. Lett.* **2003**, *91*, 216601.

(15) Pasveer, W. F.; Cottaar, J.; Tanase, C.; Coehoorn, R.; Bobbert, P. A.; Blom, P. W. M.; De Leeuw, D. M.; Michels, M. A. J. *Phys. Rev. Lett.* **2005**, *94*, 206601.

(16) Coropceanu, V.; Cornil, J.; da Silva Filho, D. A.; Olivier, Y.; Silbey, R.; Brédas, J.-L. *Chem. Rev.* **2007**, *107*, 926.

(17) Blom, P. W. M.; Mihailetchi, V. D.; Koster, L. J. A.; Markov, D. E. *Adv. Mater.* **2007**, *19*, 1551.

(18) Terao, Y.; Sasabe, H.; Adachi, C. *Appl. Phys. Lett.* **2007**, *90*, 103515.

(19) Markov, D.; Tanase, C.; Blom, P.; Wildeman, J. Simultaneous enhancement of charge transport and exciton diffusion in poly(p-phenylene vinylene) derivatives. *Physical Review B*, 2005, *72*.

(20) Abate, A.; Leijtens, T.; Pathak, S.; Teuscher, J.; Avolio, R.; Errico, M. E.; Kirkpatrik, J.; Ball, J. M.; Docampo, P.; McPherson, I.; Snaith, H. J. *Phys. Chem. Chem. Phys.* **2013**, *15*, 2572.

(21) Yan, H.; Chen, Z.; Zheng, Y.; Newman, C.; Quinn, J. R.; Dötz, F.; Kastler, M.; Facchetti, A. *Nature* **2009**, *457*, 679.

(22) De Boer, R. W. I.; Jochemsen, M.; Klapwijk, T. M.; Morpurgo, A. F.; Niemax, J.; Tripathi, A. K.; Pflaum, J. *J. Appl. Phys.* **2004**, *95*, 1196.

(23) Yang, H.; Shin, T. J.; Yang, L.; Cho, K.; Ryu, C. Y.; Bao, Z. *Adv. Funct. Mater.* **2005**, *15*, 671.

(24) Petrozza, A.; Groves, C.; Snaith, H. J. *J. Am. Chem. Soc.* **2008**, *130*, 12912.

(25) Snaith, H. J.; Grätzel, M. *Adv. Mater.* **2007**, *19*, 3643.

(26) Bach, U.; Tachibana, Y.; Moser, J.; Haque, S. A.; Durrant, J. R.; Grätzel, M. *J. Am. Chem. Soc.* **1999**, *121*, 7445.

(27) Hardin, B. E.; Snaith, H. J.; McGehee, M. D. *Nat. Photonics* **2012**, *6*, 162.

(28) Kruger, J.; Plass, R.; Cevey, L.; Piccirelli, M.; Grätzel, M.; Bach, U. *Appl. Phys. Lett.* **2001**, *79*, 2085.

(29) Grancini, G.; Santosh Kumar, R. S.; Abrusci, A.; Yip, H.-L.; Li, C.-Z.; Jen, A.-K. Y.; Lanzani, G.; Snaith, H. J. *Adv. Funct. Mater.* **2012**, *22*, 2160.

(30) Abrusci RSS Al-Hashimi, M Heeney, M Petrozza, A Snaith, HJ, A. K. *Adv. Funct. Mater.* **2011**, *21*, 2579.

(31) Abrusci, A.; Stranks, S. D.; Docampo, P.; Yip, H.-L.; Jen, A. K. Y.; Snaith, H. J. *Nano Lett.* **2013**.

(32) Cao, Y.; Bai, Y.; Yu, Q.; Cheng, Y.; Liu, S.; Shi, D.; Gao, F.; Wang, P. *J. Phys. Chem. C* **2009**, *113*, 6290.

(33) Kuciauskas, D.; Monat, J. *J. Phys. Chem. B* **2002**, 9347.

(34) Anderson, A. Y.; Barnes, P. R. F.; Durrant, J. R.; O'Regan, B. C. *J. Phys. Chem. C* **2010**, *114*, 1953.

(35) Snaith, H. J.; Humphry-Baker, R.; Chen, P.; Cesar, I.; Zakeeruddin, S. M.; Grätzel, M. *Nanotechnology* **2008**, *19*, 424003.

(36) Burschka, J.; Dualeh, A.; Kessler, F.; Baranoff, E.; Cevey-Ha, N.-L.; Yi, C.; Nazeeruddin, M. K.; Grätzel, M. *J. Am. Chem. Soc.* **2011**, *133*, 18042.

(37) Abrusci, A.; Ding, I. K.; Al-Hashimi, M.; Segal-Peretz, T.; McGehee, M. D.; Heeney, M.; Frey, G. L.; Snaith, H. J. *Energy Environ. Sci.* **2011**, *4*, 3051.

(38) Liao, H. H.; Yang, C. M.; Liu, C. C.; Horng, S. F.; Meng, H. F.; Shy, J. T. *J. Appl. Phys.* **2008**, *103*, 104506.

(39) Anta, J.; Nelson, J.; Quirke, N. Charge transport model for disordered materials: Application to sensitized TiO2. *Physical Review B*, 2002, *65*.

(40) Leijtens, T.; Ding, I. K.; Giovenzana, T.; Bloking, J. T.; McGehee, M. D.; Sellinger, A. *ACS Nano* **2012**, *6*, 1455.

(41) Snaith, H. J.; Grätzel, M. *Appl. Phys. Lett.* **2006**, *89*, 262114.

(42) Hou, J.; Chen, T. L.; Zhang, S.; Yang, Y. *J. Phys. Chem. C* **2009**, *113*, 1601.

(43) Morana, M.; Wegscheider, M.; Bonanni, A.; Kopidakis, N.; Shaheen, S.; Scharber, M.; Zhu, Z.; Waller, D.; Gaudiana, R.; Brabec, C. *Adv. Funct. Mater.* **2008**, *18*, 1757.

(44) Sablikov, V. A. *Phys. status solidi* **1973**, *15*, 735.

(45) Tuladhar, S. M.; Poplavskyy, D.; Choulis, S. A.; Durrant, J. R.; Bradley, D. D. C.; Nelson, J. *Adv. Funct. Mater.* **2005**, *15*, 1171.

(46) Cappel, U. B.; Daeneke, T.; Bach, U. *Nano Lett.* **2012**, *12*, 4925.

(47) Kopidakis, N.; Benkstein, K. D.; van de Lagemaat, J.; Frank, A. J. *J. Phys. Chem. B* **2003**, *107*, 11307.

(48) Van de Krol, R.; Goossens, A.; Meulenkamp, E. A. *J. Appl. Phys.* **2001**, *90*, 2235.

(49) Olson, C. L.; Nelson, J.; Islam, M. S. *J. Phys. Chem. B* **2006**, *110*, 9995.

(50) Moon, S.-J.; Yum, J.-H.; Humphry-Baker, R.; Karlsson, K. M.; Hagberg, D. P.; Marinado, T.; Hagfeldt, A.; Sun, L.; Grätzel, M.; Nazeeruddin, M. K. *J. Phys. Chem. C* **2009**, *113*, 16816.

(51) Fabregat-Santiago, F.; Bisquert, J.; Cevey, L.; Chen, P.; Wang, M.; Zakeeruddin, S. M.; Grätzel, M. *J. Am. Chem. Soc.* **2008**, *131*, 558.

(52) Mikhnenko, O. V; Azimi, H.; Scharber, M.; Morana, M.; Blom, P. W. M.; Loi, M. A. *Energy Environ. Sci.* **2012**, *5*, 6960.

(53) Coakley, K. M.; McGehee, M. D. *Chem. Mater.* **2004**, *16*, 4533.

(54) Vanlaeke, P.; Swinnen, A.; Haeldermans, I.; Vanhoyland, G.; Aernouts, T.; Cheyns, D.; Deibel, C.; D'Haen, J.; Heremans, P.; Poortmans, J.; Manca, J. V. *Sol. Energy Mater. Sol. Cells* **2006**, *90*, 2150.

(55) Bai, Y.; Zhang, J.; Wang, Y.; Zhang, M.; Wang, P. *Langmuir* **2011**, *27*, 4749.

(56) Furube, A.; Katoh, R.; Hara, K.; Sato, T.; Murata, S.; Arakawa, H.; Tachiya, M. *J. Phys. Chem. B* **2005**, *109*, 16406.

(57) Yu, Q.; Wang, Y.; Yi, Z.; Zu, N.; Zhang, J.; Zhang, M.; Wang, P. *ACS Nano* **2010**, *4*, 6032.

(58) Ding, I. K.; Tétreault, N.; Brillet, J.; Hardin, B. E.; Smith, E. H.; Rosenthal, S. J.; Sauvage, F.; Grätzel, M.; McGehee, M. D. *Adv. Funct. Mater.* **2009**, *19*, 2431.

(59) Melas-Kyriazi, J.; Ding, I. K.; Marchioro, A.; Punzi, A.; Hardin, B. E.; Burkhard, G. F.; Tétreault, N.; Grätzel, M.; Moser, J.-E.; McGehee, M. D. *Adv. Energy Mater.* **2011**, *1*, 407.

(60) Docampo, P.; Hey, A.; Guldin, S.; Gunning, R.; Steiner, U.; Snaith, H. J. *Adv. Funct. Mater.* **2012**, n/a.

(61) Margulis, G. Y.; Hardin, B. E.; Ding, I. K.; Hoke, E. T.; McGehee, M. D. *Adv. Energy Mater.* **2013**, *3*, 959.

(62) Cappel, U. B.; Gibson, E. A.; Hagfeldt, A.; Boschloo, G. *J. Phys. Chem. C* **2009**, *113*, 6275.

(63) Wang, M.; Moon, S.-J.; Xu, M.; Chittibabu, K.; Wang, P.; Cevey-Ha, N.-L.; Humphry-Baker, R.; Zakeeruddin, S. M.; Grätzel, M. *Small* **2010**, *6*, 319.

Chapter 6

Organometal Trihalide Perovskite Absorbers; Importance of Perovskite Pore Filling

The work presented in this chapter has been published in:

(1) Leijtens, T.; Lauber, B.; Eperon, G. E.; Stranks, S. D.; Snaith, H. J. The Importance of Perovskite Pore Filling in Organometal Mixed Halide Sensitized TiO2-Based Solar Cells. *J. Phys. Chem. Lett.* **2014**, 1096–1102.

6.1

Context

The insights gained in Chapters 4 and 5 highlight a clear pathway for making more efficient, thick, ssSSCs. Other than making thick ssSSCs, however, a higher extinction coefficient absorber could also be employed on the TiO_2 surface. This would negate the need to increase the device thickness and overcome issues with series resistance and parasitic absorption due to the low mobility Spiro-MeOTAD HTM layer. Organometal trihalide perovskites have recently been introduced as absorbers in ssSSCs with broad and intense absorption across the visible solar spectrum[1–3]. This development has resulted in rapid improvements in photocurrent and device performance. As such, the idea of making thicker ssSSCs with sensitizing dyes may now be less relevant for high efficiency applications. This chapter will focus on ssSSCs using this class of perovskite as the absorber.

One extremely fascinating and useful property of the perovskite absorbers is that they can be used as both light absorbing and charge transporting materials, changing the requirements for efficient device architectures[2,4–6]. The perovskite deposition can vary from merely sensitizing the TiO_2 electron-transporting scaffold as an endowment of small nanoparticles, to completely filling the pores where it acts as both light absorber and hole transporting material in one[4,7]. A thorough

understanding of device operation in such different configurations is essential to allow for rational design of future perovskite solar cells. In this chapter, charge transport, recombination, and device performance is analysed for several different configurations. By decreasing the TiO_2 scaffold layer thickness, the solar cell architecture is changed from perovskite - sensitized to completely perovskite – filled. The latter case leads to improvements in device performance because higher electron densities can be sustained in the TiO_2, improving electron transport rates and photo-voltage. Importantly, the primary recombination pathway between the TiO_2 and the hole transporting material is blocked by the perovskite itself. This understanding helps to rationalize the high voltages attainable on mesoporous TiO_2 based perovskite solar cells, and suggests routes towards future improvements.

6.2

Introduction

Dye sensitized ssSSCs have fallen short of the predicted performances, reaching a maximum of 7.2 % power conversion efficiency when using custom-synthesized light-absorbing dyes and specially-designed dopants to improve the charge transport in the hole transporting layer[8]. This is largely because the current generation of high performance sensitizing dyes require device thicknesses over 5 μm for complete light harvesting, but optimized device thicknesses are around 2 μm[9,10]. The reasons for this have been discussed in Chapters 2 and 5. It was only recently, with organometal halide perovskites sensitizing the mesoporous TiO_2 electron-collecting anode, that solid-state sensitized solar cells have started to approach their predicted high performances. Following earlier work from Kojima *et al.*[1], Kim *et al.*[5] and Lee *et al.*[6] demonstrated the use of $CH_3NH_3PbI_3$ and a "mixed halide" $CH_3NH_3PbI_{3-x}Cl_x$, respectively, in traditional ssSSC architectures. The materials have since been shown to be capable of efficiently transporting charge carriers and hence can function in a "thin film" planar heterojunction solar cell configuration[11–14]. In ssSSC architecture, the perovskites were shown to be effective hole transporters, negating the requirement to infiltrate the organic hole transporter, Spiro-MeOTAD, into the TiO_2 mesopores[2,4,6,12,15–17]. Indeed, the planar

heterojunction solar cells have reached high performances to of over 15 %[6,12,13,18,19]. Moreover, some of the best results using $CH_3NH_3PbI_3$ in ssSSCs come from device architectures where the perovskite deposition has been optimized to fill the TiO_2 mesopores and leave a capping layer of perovskite on top of the TiO_2 layer, yielding performances over 15 %[20–22]. The processes of charge transport and recombination in such devices will necessarily differ from those in traditional dye sensitized ssSSCs but, at the time of this work, there has been no work on understanding the importance of perovskite filling of the mesoporous TiO_2 for device performance. This chapter focuses on the differences in operation of purely perovskite "sensitized" and perovskite "filled" ssSSCs. The perovskite used is the "mixed" halide perovskite $CH_3NH_3PbI_{3-x}Cl_x$.

6.3

Perovskite Pore Filling

Figure 6.1 shows cross-sectional SEM images of the four different architectures used in this study, ranging from sensitized to completely perovskite-filled TiO_2 composites. A "sensitized" architecture (Fig. 6.1a) is ensured by using a thick (750 nm) TiO_2 scaffold in conjunction with a low (30 wt %) concentration of perovskite precursor spin coating solution[2]. Such films, however, do not absorb light very strongly, as will be shown in Figure 6.3a. To enhance the absorption, the same scaffold thickness is used in conjunction with a 40 wt % concentration of the perovskite precursor solution. In this case, a higher but still non-continuous coverage of the perovskite is expected on the TiO_2 nanoparticles. These films then absorb much more strongly, as will be seen in Figure 6.3a. To ensure a close to complete filling of the TiO_2 mesopores, the scaffold thickness is decreased to 440 and 260 nm, as seen in Figures 6.1c and 6.1d respectively, while using a 40 wt% precursor solution. Since capping layers of perovskite begin to form at TiO_2 scaffold thicknesses of just under 400 nm[15], it is at this thickness that the perovskite is expected to begin to completely, or close to completely, fill the pores of the TiO_2. Figure 6.1d clearly demonstrates the tendency of the perovksite to form a capping

layer over the thin (260 nm) TiO_2 scaffold, and perovskite pore filling is hence expected to be high in such films.

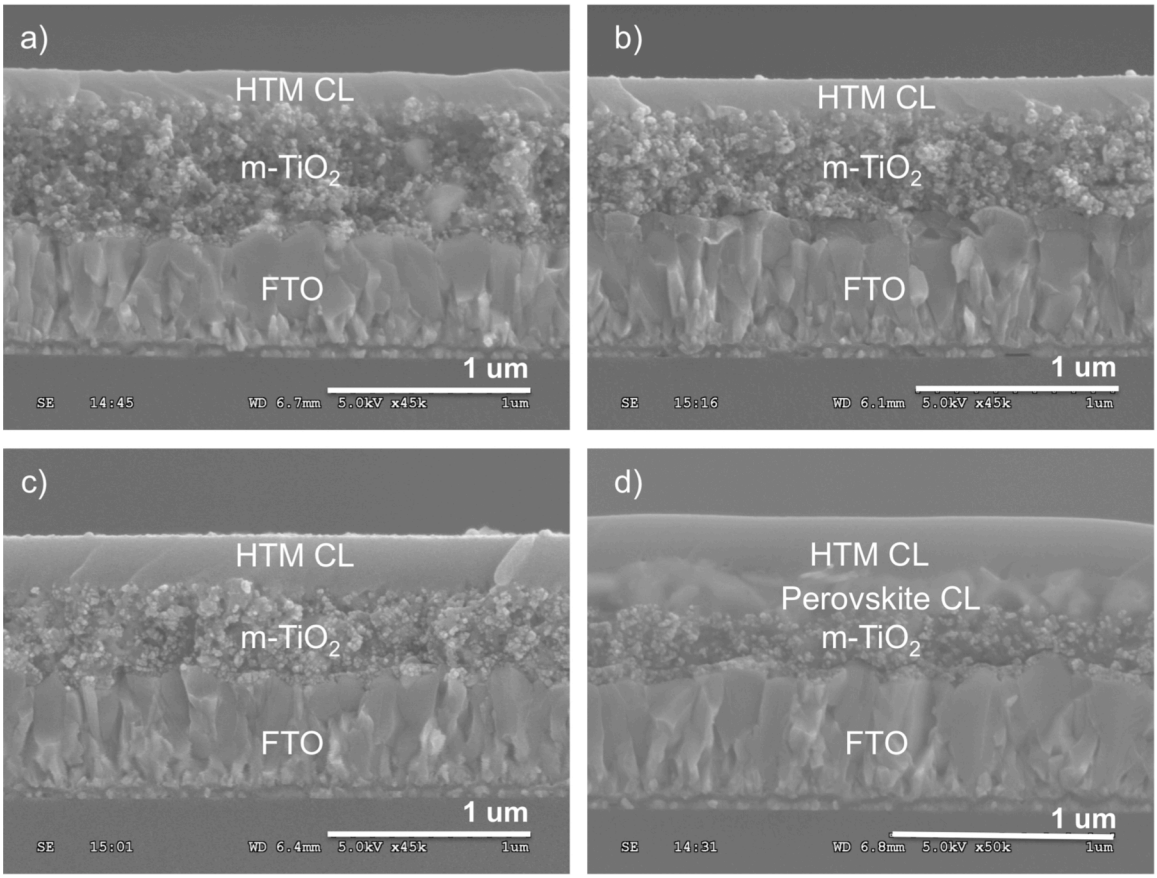

Figure 6.1. Cross-sectional scanning electron microscope (SEM) images of the different ssSSC architectures used in this study. m-TiO_2 stands for mesoporous TiO_2. The architectures range from: (a) a 750 nm TiO_2 scaffold (m-TiO_2) with 30 wt% perovskite precursor solution to (b) 750 nm TiO_2 with 40 wt% to (c) 440 nm TiO_2 with 40 wt% to (d) 260 nm TiO_2 with 40 wt%. These architectures should correspond to changes from (a), (b) sensitized with nonuniform coverage to (c) fully perovskite-filled to (d) fully perovskite filled with a perovskite capping layer (CL). These images were taken by Giles E Eperon at the Department of Physics, University of Oxford.

Meso-TiO_2 Thickness	750 nm	750 nm	440 nm	260 nm
Perovskite concentration	30 wt%	40 wt%	40 wt%	40 wt%
Pore Filling Fraction (%)	47 ± 2	70 ± 3	108 ± 4	100 ± 5

Table 6.1. Estimation of perovskite pore filling fraction and coating thickness. These calculations were performed by Giles E Eperon at the Department of Physics, University of Oxford.

In order to measure the pore filling fractions, samples of perovskite on TiO_2 were prepared as for devices (Chapter 3) but on larger area FTO glass substrates (5.6x5.6cm). Prior to perovskite deposition, the thickness of the TiO_2 and the mass of the substrate were measured, using a Dektak profilometer and an accurate balance, respectively. Subsequent to perovskite deposition and annealing, the samples were re-weighed, and the difference in mass before and after perovskite deposition used to determine the mass of perovskite deposited on each sample.

The density of the perovskite can be determined by knowing the size of the tetragonal unit cell from x-ray diffraction measurements (Figure 6.2), in good agreement with previous reports[23]. A unit cell for a tetragonal lattice with a=8.87 Å, b=8.87 Å, c=12.67Å has volume of 997Å^3, which contains 4 × (MA+Pb+3I), for a total M_w of 2480[24]. The calculated density for the perovskite from this is thus 4.13gcm^{-3}. We note that here we assume negligible chloride incorporation in the annealed perovskite, as reported in the literature, and assume that the crystal structure is the same as that of the pure methylammonium triiodide perovkite[23,25]. From the density of the perovskite and mass of perovskite deposited, it is trivial to determine the volume of perovskite deposited in the TiO_2 film.

The porosity of TiO_2 prepared in this way has been previously reported to be 0.5[26]. From this the volume of pores in the TiO_2 is calculated for a given film thickness, and then knowing the volume of perovskite deposited in the TiO_2, a perovksite pore filling fraction is calculated, defined as the ratio of perovskite volume in film to the TiO_2 pore volume in the film. Errors in the pore filling fraction arise predominantly from errors in substrate size. It must also be noted that if there are any impurities present within the perovskite phase, this will result in an overestimation of the perovskite filling fraction in the TiO_2 pores, so the error is difficult to quantify exactly.

The results are presented in Table 6.1. The error in the calculation comes from consideration of the sensitivity of the scale, error in estimation of the substrate size, and error in determination of the size of the $CH_3NH_3PbI_{3-x}Cl_x$ unit cell. The pore filling fractions are evidently heavily dependent on the TiO_2 scaffold thickness, increasing

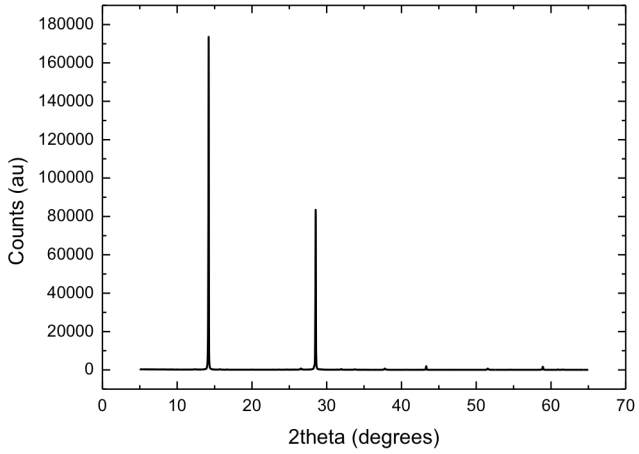

Figure 6.3. A representative X-ray diffraction spectrum of the annealed mixed halide perovskite. Peaks at 14.2°, 28.4° and 43° are assigned to the (110), (220) and (330) planes of a highly oriented tetragonal perovskite structure as reported in the literature[24]. This data was taken by by Giles E Eperon at the Department of Physics, University of Oxford.

from 47 % in the thick TiO_2 scaffolds to around 100 % with TiO_2 layers thinner than 400 nm. In the latter case, since there is negligible remaining porosity, the organic HTM spiro-MeOTAD is clearly unable to infiltrate the pores. Thus, the perovskite absorber must be transporting holes through the active layer to the p-type heterojunciton[20,21]. Where there is a perovskite capping layer, the perovskite must necessarily be capable of transporting both holes and electrons towards the mesoporous TiO_2.

6.3

Device Performance

Figure 6.3b depicts the *J-V* curves of the best solar cells with the architectures just described, and the extracted device performance parameters are displayed in Table 6.2. The mean and standard deviation of each parameter are also displayed for a given batch of devices. As the perovskite concentration increases and the scaffold thickness decreases (ie perovskite pore filling increases), there is a rapid improvement in both the photocurrent and photo-voltages of the solar cells. For the series using the same 40 wt % precursor solutions, the short-circuit currents rise

quickly with decreased scaffold thickness, even though the optical density of the films is marginally decreased (Figure 6.3a). This means that the differences in photocurrent do not lie in light absorption, but rather in the charge collection efficiency. The greater than 100 mV improvement in photo-voltage with decreased TiO_2 thickness could be expected if the electron density in the TiO_2 is increased partly because the total generated charge is concentrated in a smaller volume of scaffold. This will lead to an increase in the electron quasi-Fermi level in the TiO_2, improving the photovoltage[27–29]. The other possibility is that in devices with high perovskite pore filling, the charge actually resides in and is transported through the perovskite itself, resulting in improved charge extraction and photovoltages[2].

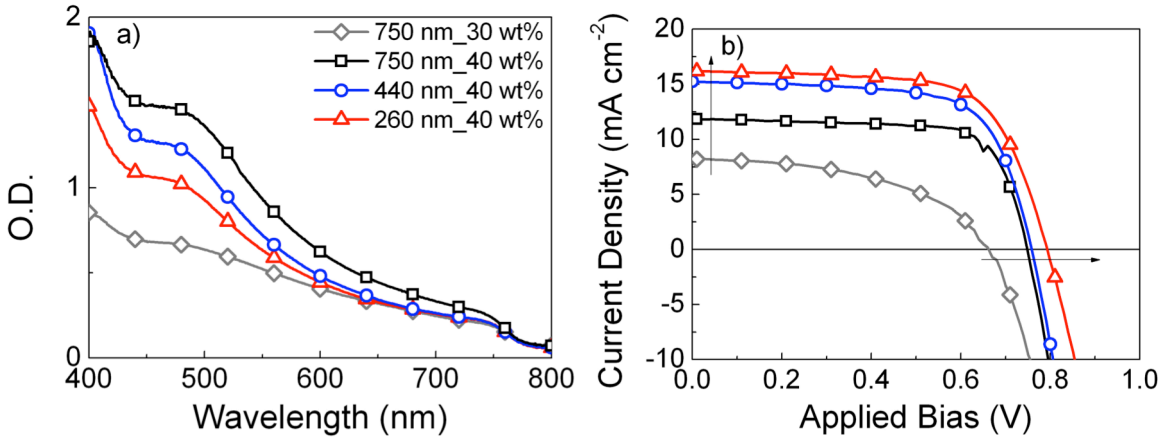

Figure 6.3. (a) Optical density (O.D.) of the different architectures described in Figure 6.1, taken with an integrating sphere to account for scattering effects. (b) *J-V* characteristics of the same samples after top silver electrode evaporation under 100 mW cm^{-2} simulated AM1.5 solar irradiation.

Meso-TiO_2 Thickness	750 nm	750 nm	440 nm	260 nm
Perovskite concentration	30 wt%	40 wt%	40 wt %	40 wt%
Pore Filling Fraction (%)	47 ± 2	70 ± 3	108 ± 4	100 ± 5
Jsc (mA cm-2)	8.2	11.8	15.3	16.5
(mean)	6.3 ± 1.4	11.2 ± 2.0	13.6 ±1.8	15.5 ±1.3
PCE (%)	2.6	6.3	7.6	8.6
(mean)	1.9 ± 0.5	5.06 ±1.2	6.3 ±1.2	6.4 ±1.6
Voc	0.66	0.75	0.76	0.8
(mean)	0.67 ±0.07	0.73 ± 0.03	0.74 ± 0.04	0.76 ± 0.05
FF	0.60	0.73	0.68	0.67
(mean)	0.49 ±0.07	0.64 ± 0.08	0.62 ±0.1	0.57 ± 0.1

Table 6.2. Performance parameters of the best devices with different perovskite pore filling fractions. The mean values and the standard deviations for the batch of devices are reported below the performance parameters of the highest performance solar cells.

6.4

Charge Dynamics

PIA spectroscopy (Figure 6.4) was employed with the aim to understand whether the improved photo-voltage of the solar cells with thinner TiO_2 layers does indeed come from an increase in electron density within the TiO_2. By preparing samples identical to those used for the solar cells (but without Spiro-MeOTAD or metal electrodes), it is possible to qualitatively monitor the electron density in each architecture under illumination. The HTM was omitted since holes on Spiro-MeOTAD will dominate the PIA spectrum (see Chapter 5). The PIA spectra (normalized for device thickness and O.D.) of the different architectures are plotted in Figure 6.4, and all samples show a clear absorption peak centred around 1000 nm, which has been previously assigned to shallowly trapped electrons in TiO_2[30]. This suggests that even when the TiO_2 pores are largely filled with perovskite, electrons are transferred to the TiO_2 with a high efficiency, just as Abrusci *et al*. and Marchioro *et al*. have demonstated via photoluminescence quenching and TAS, respectively[31,32]. Recent impedance spectroscopy and microwave conductivity studies have also demonstrated this to be the case for the $CH_3NH_3PbI_3$ perovskite infiltrated into mesoporous TiO_2[33–35]. When the photo-induced change in transmission is normalized

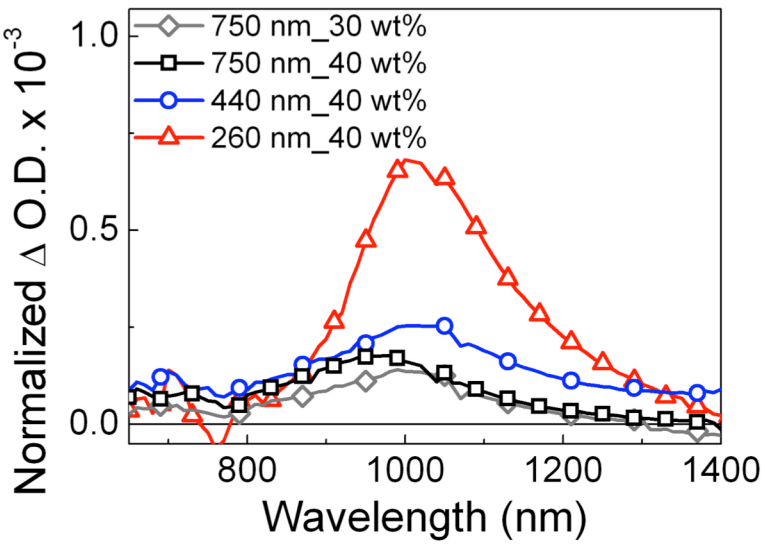

Figure 6.4. Quasi steady state photo-induced absorption spectra (PIA) were taken at an excitation wavelength of 514 nm and a fluence of 50 mW cm^{-2}, chopped at 23 Hz. The spectra for the relevant architectures are normalized by device thickness and optical density at the excitation wavelength of 514 nm to adjust for differences in the generation rate.

for TiO_2 layer thickness and film O.D. at the laser excitation wavelength of 514 nm, it is apparent that at a given generation rate, the electron density is indeed much higher in the thin TiO_2 layers than in the thicker layers. This is expected, since the thinner (260 nm) TiO_2 layers still have large capping layers of perovskite over significant portions of the active layer. Charges generated in the capping layer are rapidly transferred to the TiO_2 because of the high diffusivity of photogenerated carriers within the perovskite[12] meaning that the total number charges generated throughout the active layer is effectively concentrated into a thinner TiO_2 film.

The charge recombination rate may also be expected to be slower in the thin samples with high perovskite pore filling fractions. Assuming the recombination is between electrons in the TiO_2 with holes in the perovskite in the HTM – free samples, then there is simply less available surface area with the perovskite through which such recombination could occur. Reduced recombination rates would hence also contribute to an increased electron density in the thinner TiO_2 layers. While this may not be the dominant recombination pathway in working solar cells with HTM layers, the decreased surface area should generally slow all recombination rates for electrons in the TiO_2. It is then no surprise that the solar cells do demonstrate significant improvements in photovoltage with decreasing TiO_2 thickness.

To probe the cause for improved photocurrents with decreased scaffold thicknesses, small perturbation photocurrent and photovoltage decay measurements were performed as described in Chapter 3[36]. This technique makes it possible to probe the charge transport lifetimes as well as the short-circuit recombination lifetimes, the relative magnitudes of which can give an indication of the charge collection efficiency[37]. The results are depicted in Figure 6.5. It should be noted that the charge transport lifetimes will be limited by the slow electron transport through the mesoporous TiO_2 at the relatively low charge densities found at short circuit[2,29,38]. In Figure 6.5a, the charge transport rates are plotted as a function of the background light intensity. Here, it is evident that at a given light intensity, the solar cells with thinner TiO_2 layers benefit from a decreased charge transport lifetime, or increased transport rate.

If, however, the results are plotted as a function of the short-circuit electron density in TiO_2 (obtained through charge extraction measurements described in Chapter 3) as in Figure 6.5b, the reason for the aforementioned improved charge transport lifetimes can be understood. It is now apparent that the transport lifetimes in each architecture are very similar when compared at the same electron densities in the TiO_2. Moreover, the slopes of the lifetimes with electron density are also similar, demonstrating that regardless of device architecture, the electron transport is governed by the same multi-trapping mechanism that has been widely accepted to be the mechanism for electron transport in mesoporous TiO_2, as discussed in Chapters 2, 4 and 5[29,38–40]. As already observed in Figure 6.4, the thinner scaffolds simply build up higher charge densities in the TiO_2 at any given light intensity, and this leads to shorter charge transport lifetimes in the solar cells.

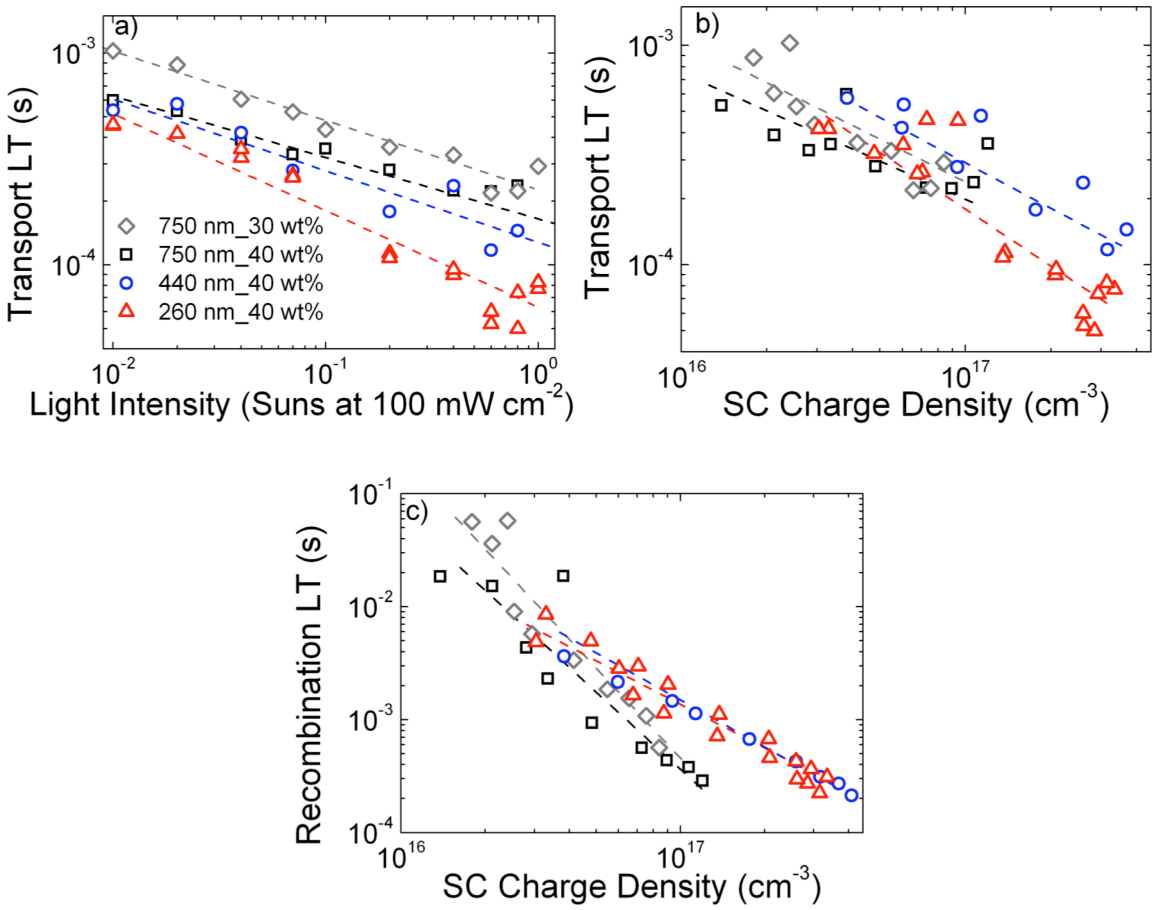

Figure 6.4. Charge transport and recombination lifetimes. (a) The charge transport lifetimes in different architectures are plotted as a function of background light intensity. These are replotted in (b) as a function of short circuit (SC) charge density. The Recombination lifetimes are plotted as a function of SC charge density in (c). Comparison of the lifetimes in (b) and (c) allow for a qualitative estmation of the charge collection efficiency. The dotted lines are merely guides to the eye.

For the improved charge transport rates to translate to improved charge collection efficiencies, the recombination rate at short circuit in the thin solar cells must be significantly slower than the charge transport. In Figure 6.5c, the short circuit recombination lifetimes are plotted as a function of charge density. Two distinctly different classes of behaviour are immediately apparent: there are far steeper decreases in recombination lifetime with increasing charge density in the sensitized solar cells with thicker scaffolds, and hence low perovskite pore filling fractions, than in the solar cells with thinner scaffolds and higher perovskite pore filling. In fact, the short circuit recombination lifetimes for the thinner scaffolds are far slower, compared to those for the thicker scaffolds, at the high charge densities that correspond to conditions under one sun. The lifetimes for recombination ($\sim$ 2-3 $\times$ 10^{-4} s) and transport ($\sim$ 2-3 $\times$ 10^{-4} s) at high charge densities (one sun light intensity) are similar for the solar cells with low perovskite pore filling fractions, such that the collection is expected to be inefficient,[37] whereas the transport lifetimes ($\sim$ 6 $\times$ 10^{-5} s) are significantly faster than the recombination lifetimes ($\sim$ 3 $\times$ 10^{-4} s) for the solar cells with highest perovskite pore filling fractions under the same light intensity.

Hence, the solar cells made with thinner TiO_2 layers and higher pore filling fractions benefit significantly from improved charge collection efficiencies. This appears to be because they can sustain high electron densities in the TiO_2, accelerating electron transport, without suffering from the rapid increase in recombination rates observed for the solar cells with lower perovskite coverage. In addition, a significant proportion of the electron migration across the active layer must take place within the solid perovskite film, prior to transferring to the mesoporous TiO_2. By comparing the slopes of electron transport lifetime with the electron density, it can be concluded that the electron transport mechanism responsible for the decay of the photocurrent remains the same, regardless of TiO_2 scaffold thickness, i.e. electrons are transported through the mesoporous TiO_2 to the collection electrode.

Perhaps the most interesting finding here is the decrease in the recombination rate's dependence on charge density, signifying a change in recombination mechanism. In the solar cells with low perovskite coverage, the

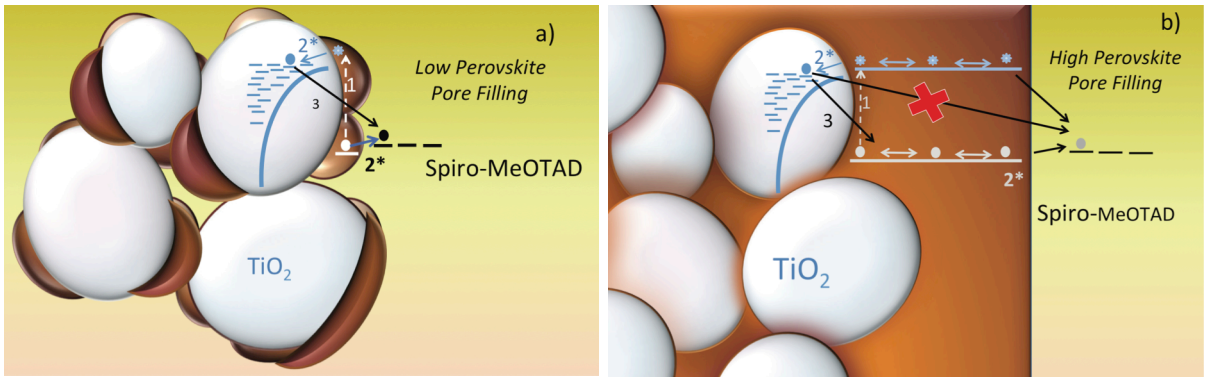

Scheme 6.1. Proposed recombination mechanisms for solar cells with incomplete (a) and complete (b) perovskite pore filling fractions. Step 1 (white arrow) stands for photo-excitation of the perovskite absorber, step 2 (light blue arrow) to electron injection into TiO_2 and hole transfer to the HTM, while steps 3 (black arrows) represent the recombination pathways.

recombination mechanism is expected to be similar to that found in dye sensitized solar cells, where electrons in the TiO_2 recombine with holes on Spiro-MeOTAD[27,33,41]. Since the coverage of perovskite is not expected to be completely uniform and there is likely to be some exposed TiO_2 allowing more unwanted contact with the Spiro-OMeTAD, the recombination rates may even be expected to be faster than in solid state dye sensitized solar cells where the dye molecules form a dense layer on the TiO_2 surface. Indeed, the recombination lifetime of 3×10^{-4} s at a charge density of 10^{17} cm^{-3} observed here for perovskite sensitized cells is much faster than the 10^{-3} s or so observed in Chapter 4 and in the literature at similar charge densities in solid state dye sensitized solar cells[33,41,42].

Based on the above analysis, a mechanism for charge recombination is developed and depicted in Scheme 6.1 for architectures with low and high perovskite pore filling fractions. The case where there is incomplete perovskite coverage on the mesoporous TiO_2 is depicted in Scheme 6.1a, while that for high pore filling fractions is depicted in Scheme 6.1b. When the pores start to be completely filled with perovskite, the Spiro-MeOTAD – TiO_2 contact will be virtually eliminated[20]. Hence the primary recombination pathway will be largely removed. Recombination of electrons in TiO_2 with holes in the perovskite itself is moreover unlikely to be very fast, since the hole density in the perovskite should be relatively low due to their high diffusivity and effective transfer to Spiro-MeOTAD at the planar heterojunction[12]. The same applies for the recombination of holes in Spiro-MeOTAD with electrons in the

perovskite: the electron density in the perovskite will be very low due to the fast electron transfer to the TiO_2 nanoparticles, meaning this recombination mechanism will also be very slow[34].

These realizations rationalize why some of the best performing perovskite ssSSCs reported in the literature are those with large perovskite capping layers[20–22]. In this work, perovskite capping layers could only be formed on relatatively thin TiO_2 electrodes, limiting the overall thickness and light absorption of the devices (Figure 6.3). This is due to limitations in the chosen spin coating deposition technique. Alternative deposition techniques such as sequential deposition, recently introduced by Burshka *et al*.[22] should allow for high perovskite pore filling fractions and capping layers to be achieved on thicker scaffolds, which would increase the O.D. and hence photocurrent and electron fermi level in the TiO_2. This is a clear path towards further optimization of perovskite ssSSCs.

6.5

Summary and Outlook

By changing the TiO_2 scaffold thickness along with the perovskite precursor solution concentration, it was possible to control the degree of perovskite pore filling in the TiO_2 mesopores. The devices were characterized in terms both photovoltaic conversion efficiency as well as charge dynamics. The understanding gained in this chapers suggests certain design rules for preparing high efficiency TiO_2 - based perovskite solar cells. The most important factor to control is the completeness of perovskite coverage on the TiO_2 nanoparticles, as this reduces recombination rates. This means that higher charge densities can be maintained in the TiO_2, improving the charge transport rates and collection efficiencies of the solar cells. This, together with the fact that thinner TiO_2 scaffolds serve to concentrate the electron density at a given generation rate, also leads to a raising of the electron quasi Fermi level in the TiO_2 to improve the photovoltage of the solar cells. In this work, this is achieved by reducing the TiO_2 scaffold thickness, which unfortunately decreases the optical density of the film. Future work is likely to be focused on using new deposition processes, such as the sequential deposition process introduced by Burschka et. al.[22],

to achieve high perovskite pore filling fractions with thicker (but still on the order of 1 μm) active layers. The work presented here also emphasizes that the most efficient TiO_2 based perovskite solar cells operate in a distinctly different manner to conventional sensitized solar cells[20]. The photogenerated electrons within the perovskite capping layer diffuse throughout this layer to the mesoporous TiO_2 electrode, and the holes throughout the whole of the photoactive layer are transported within the perovskite phase back to the planar heterojunction with the p-type hole-transporter. In essence, the mesoporous TiO_2 is performing the function of a rough electrode to facilitate long-lasting charge separation.

This Chapter has studied the use of a new absorber, $CH_3NH_3PbI_{3-x}Cl_x$, in ssSSCs. The broad and intense absorption spectrum of the material allows ssSSCs to achieve high photocurrents in thin solar cell architectures. In addition, the perovskite absorber can be infiltrated into the TiO_2 mesopores to function as a hole transporter in its own right. ssSSCs of this configuration then overcome the difficulties associated with achieving higher O.D. dye sensitized ssSSCs, as series resistance and parasitic absorption losses due to the low mobility HTM are no longer large factors limiting conversion efficiency.

6.6

References

(1) Kojima, A.; Teshima, K.; Shirai, Y.; Miyasaka, T. *J. Am. Chem. Soc.* **2009**, *131*, 6050.

(2) Lee, M. M.; Teuscher, J.; Miyasaka, T.; Murakami, T. N.; Snaith, H. J. *Science (80-.).* **2012**, *338*, 643.

(3) Kim, H.-S.; Lee, C.-R.; Im, J.-H.; Lee, K.-B.; Moehl, T.; Marchioro, A.; Moon, S.-J.; Humphry-Baker, R.; Yum, J.-H.; Moser, J. E.; Grätzel, M.; Park, N.-G. *Sci. Rep.* **2012**, *2*.

(4) Etgar, L.; Gao, P.; Xue, Z.; Peng, Q.; Chandiran, A. K.; Liu, B.; Nazeeruddin, M. K.; Grätzel, M. *J. Am. Chem. Soc.* **2012**, *134*, 17396.

(5) Stranks, S. D.; Eperon, G. E.; Grancini, G.; Menelaou, C.; Alcocer, M. J. P.; Leijtens, T.; Herz, L. M.; Petrozza, A.; Snaith, H. J. *Science* **2013**, *342*, 341.

(6) Liu, M.; Johnston, M. B.; Snaith, H. J. *Nature* **2013**, *501*, 395.

(7) Malinkiewicz, O.; Yella, A.; Lee, Y. H.; Espallargas, G. M.; Graetzel, M.; Nazeeruddin, M. K.; Bolink, H. J. *Nat. Photonics* **2013**, *8*, 1.

(8) Burschka, J.; Dualeh, A.; Kessler, F.; Baranoff, E.; Cevey-Ha, N.-L.; Yi, C.; Nazeeruddin, M. K.; Grätzel, M. *J. Am. Chem. Soc.* **2011**, *133*, 18042.

(9) Ding, I. K.; Tétreault, N.; Brillet, J.; Hardin, B. E.; Smith, E. H.; Rosenthal, S. J.; Sauvage, F.; Grätzel, M.; McGehee, M. D. *Adv. Funct. Mater.* **2009**, *19*, 2431.

(10) Hardin, B. E.; Snaith, H. J.; McGehee, M. D. *Nat. Photonics* **2012**, *6*, 162.

(11) Docampo, P.; Ball, J. M.; Darwich, M.; Eperon, G. E.; Snaith, H. J. *Nat. Commun.* **2013**, *4*, 2761.

(12) Stranks, S. D.; Eperon, G. E.; Grancini, G.; Menelaou, C.; Alcocer, M. J. P.; Leijtens, T.; Herz, L. M.; Petrozza, A.; Snaith, H. J. *Science (80-.).* **2013**, *342*, 341.

(13) Eperon, G. E.; Burlakov, V. M.; Docampo, P.; Goriely, A.; Snaith, H. J. *Adv. Funct. Mater.* **2013**, *24*, 151.

(14) Liu, D.; Kelly, T. L. *Nat. Photonics* **2013**, *8*, 1.

(15) Ball, J. M.; Lee, M. M.; Hey, A.; Snaith, H. J. *Energy Environ. Sci.* **2013**, *6*, 1739.

(16) Laban, W. A.; Etgar, L. *Energy Environ. Sci.* **2013**, *6*, 3249.

(17) Eperon, G. E.; Burlakov, V. M.; Docampo, P.; Goriely, A.; Snaith, H. J. *Adv. Funct. Mater.* **2013**, *24*, 151.

(18) Docampo, P.; Ball, J. M.; Darwich, M.; Eperon, G. E.; Snaith, H. J. *Nat. Commun.* **2013**, *4*, 2761.

(19) Jeng, J.-Y.; Chiang, Y.-F.; Lee, M.-H.; Peng, S.-R.; Guo, T.-F.; Chen, P.; Wen, T.-C. *Adv. Mater.* **2013**, *25*, 3727.

(20) Heo, J. H.; Im, S. H.; Noh, J. H.; Mandal, T. N.; Lim, C.-S.; Chang, J. A.; Lee, Y. H.; Kim, H.; Sarkar, A.; NazeeruddinMd, K.; Grätzel, M.; Seok, S. Il. *Nat Phot.* **2013**, *7*, 486.

(21) Noh, J. H.; Im, S. H.; Heo, J. H.; Mandal, T. N.; Seok, S. Il. *Nano Lett.* **2013**, *13*, 1764.

(22) Burschka, J.; Pellet, N.; Moon, S.-J.; Humphry-Baker, R.; Gao, P.; Nazeeruddin, M. K.; Grätzel, M. *Nature* **2013**, *499*, 316.

(23) Colella, S.; Mosconi, E.; Fedeli, P.; Listorti, A.; Orlandi, F.; Ferro, P.; Besagni, T.; Rizzo, A.; Calestani, G.; Gigli, G.; Angelis, F. De; Mosca, R.; Gazza, F. *Chem. Mater.* **2013**, *25*, 4613.

(24) Baikie, T.; Fang, Y.; Kadro, J. M.; Schreyer, M.; Wei, F.; Mhaisalkar, S. G.; Grätzel, M.; White, T. J. *J. Mater. Chem. A* **2013**, *1*, 5628.

(25) You, J.; Hong, Z.; Yang, Y. M.; Chen, Q.; Cai, M.; Song, T.; Chen, C.; Lu, S.; Liu, Y.; Zhou, H.; Yang, Y. *ACS Nano* **2014**, *7*, 994.

(26) Docampo, P.; Hey, A.; Guldin, S.; Gunning, R.; Steiner, U.; Snaith, H. J. *Adv. Funct. Mater.* **2012**, n/a.

(27) Fabregat-Santiago, F.; Bisquert, J.; Cevey, L.; Chen, P.; Wang, M.; Zakeeruddin, S. M.; Grätzel, M. *J. Am. Chem. Soc.* **2008**, *131*, 558.

(28) Snaith, H. J. *Adv. Funct. Mater.* **2010**, *20*, 13.

(29) Leijtens, T.; Lim, J.; Teuscher, J.; Park, T.; Snaith, H. J. *Adv. Mater.* **2013**, *25*, 3227.

(30) Anderson, A. Y.; Barnes, P. R. F.; Durrant, J. R.; O'Regan, B. C. *J. Phys. Chem. C* **2010**, *114*, 1953.

(31) Abrusci, A.; Stranks, S. D.; Docampo, P.; Yip, H.-L.; Jen, A. K. Y.; Snaith, H. J. *Nano Lett.* **2013**.

(32) Marchioro, A.; Teuscher, J.; Friedrich, D.; Kunst, M.; van de Krol, R.; Moehl, T.; Grätzel, M.; Moser, J.-E. *Nat. Photonics* **2014**, *8*, 250.

(33) Zhao, Y.; Nardes, A. M.; Zhu, K. *J. Phys. Chem. Lett.* **2014**, 490.

(34) Marchioro, A.; Teuscher, J.; Friedrich, D.; Kunst, M.; van de Krol, R.; Moehl, T.; Grätzel, M.; Moser, J.-E. *Nat. Photonics* **2014**, *8*, 250.

(35) Ponseca, C. S.; Savenije, T. J.; Abdellah, M. a.; Zheng, K.; Yartsev, A. P.; Pascher, T.; Harlang, T.; Chabera, P.; Pullerits, T.; Stepanov, A.; Wolf, J.-P.; Sundstrom, V. *J. Am. Chem. Soc.* **2014**, *136*, 5189.

(36) O'Regan, B. C.; Lenzmann, F. *J. Phys. Chem. B* **2004**, *108*, 4342.

(37) Sivaram, V.; Kirkpatrick, J.; Snaith, H. *J. Appl. Phys.* **2013**, *113*, 063709.

(38) Kopidakis, N.; Benkstein, K. D.; van de Lagemaat, J.; Frank, A. J. *J. Phys. Chem. B* **2003**, *107*, 11307.

(39) Docampo, P.; Guldin, S. *J. Phys. Chem. Lett.* **2013**, *4*, 698.

(40) Van de Lagemaat, J.; Frank, A. J.; Lagemaat, J. Van De. *J. Phys. Chem. B* **2001**, *105*, 11194.

(41) Kruger, J.; Plass, R.; Cevey, L.; Piccirelli, M.; Grätzel, M.; Bach, U. *Appl. Phys. Lett.* **2001**, *79*, 2085.

(42) Abate, A.; Leijtens, T.; Pathak, S.; Teuscher, J.; Avolio, R.; Errico, M. E.; Kirkpatrik, J.; Ball, J. M.; Docampo, P.; McPherson, I.; Snaith, H. J. *Phys. Chem. Chem. Phys.* **2013**, *15*, 2572.

Chapter 7

Ultraviolet Light Induced Instability of Mesoporous TiO_2 in Solid State Sensitized Solar Cells

The work presented in this chapter has been published and discussed in:

(1) Leijtens, T.; Eperon, G. E.; Pathak, S.; Abate, A.; Lee, M. M.; Snaith, H. J. Overcoming Ultraviolet Light Instability of Sensitized TiO_2 with Meso-Superstructured Organometal Tri-Halide Perovskite Solar Cells. *Nat. Commun.* **2013**, *4*, 2885.

2) *Docampo, P.; *Guldin, S.; *Leijtens, T.; Noel, N. K.; Steiner, U.; Snaith, H. J. Lessons Learned: From Dye-Sensitized Solar Cells to All-Solid-State Hybrid Devices. *Adv. Mater.* **2014**, n/a–n/a.

3) Pathak, S. K.; Abate, A.; Leijtens, T.; Hollman, D. J.; Teuscher, J.; Pazos, L.; Docampo, P.; Steiner, U.; Snaith, H. J. Towards Long-Term Photostability of Solid-State Dye Sensitized Solar Cells. *Adv. Energy Mater.* **2014**, n/a–n/a.

* These three authors contributed equally (statement in acknowledgements section).

7.1

Context

Organometal trihalide perovskite absorbers with broad and intense absorption across the solar spectrum have recently been introduced as sensitizers in ssSSCs, resulting in rapid improvements in photo-currents and device performances, as described in Chapter 6. As such, the idea of making thicker ssSSCs with sensitizing dyes may now be less relevant for making high performance ssSSCs. In the most basic configuration, these solar cells operate in the same way as the dye sensitized ssSSCs, so that any problems with regards to the stability of either mesoporous TiO_2 anode or HTM layers will be common to all ssSSC architectures.

As promising as the development of high performance (15 %) ssSSCs based on organometal trihalide perovskites is, long-term operational stability is even more

important than initial conversion efficiency when it comes to the development of practical solid-state solar cells. As such, this chapter will focus on a major stability issue that applies to all ssSSC configurations, whether they employ dye or perovskite absorbers. The tools developed in Chapter 5 provide a unique opportunity to study electron and hole transport processes during aging of ssSSCs. In this chapter, it is found that a critical instability in mesoporous-TiO_2-sensitized solar cells arises from light-induced desorption of surface adsorbed oxygen. Changing the recombination pathway by changing the perovskite pore filling fraction (as described in Chapter 6), as well as completely removing the mesoporous TiO_2 layer, both help in overcoming the light induced instability of ssSSCs.

7.2

Introduction

ssSSCs, where mesoporous TiO_2 is used as the electron transporter, have reached close to commercial power conversion efficiencies of over to 17 % with solid-state hole transporters and organometal halide perovskite absorbers, as described in Chapter 6[1–5]. The improvement over conventional ssSSCs using dye sensitizers is due to the perovskite materials' broad and intense absorption, demonstrated in Chapter 2. Additionally, organometal halide perovskites are capable of transporting both electrons and holes[3,6], and operate efficiently in a planar p-i-n heterojunction configuration, delivering over 15% efficiency[2,7–10]. When $CH_3NH_3PbI_{3-x}Cl_x$ is coated onto an insulating alumina scaffold, it can yield performances of up to 16 % in a mesoporous TiO_2 – free hybrid solar cell, which has been termed a meso-superstructured solar cell (MSSC)[2,3,11,12]. These solid-state approaches have the advantage that they do not suffer from electrolyte leakage, nor does the hole transporting material (HTM) possess any corrosive qualities that we know of, so that such devices are lauded as more fundamentally stable than their liquid electrolyte counterparts[13–15]. As the efficiency is likely to increase and become comparable with the best thin-film and wafer based technologies, a critical challenge for global adoption of perovskite based solar cells is the proof or realisation of longevity.

Realising stable modules is an industrial task, largely down to effective encapsulation and module design, rather than a fundamental academic task. However, ensuring that the basic chemistry from which the technology is constructed is fundamentally stable will reduce the subsequent industrial effort required and greatly help the technology to enter the market.

Considering the importance of a solar cell's long-term stability and the premise of solid-state sensitized solar cells delivering superior stability than the liquid electrolyte counterparts, there is very little published research on the topic[4,16–21]. The studies which have been conducted to date for dye sensitized and perovskite sensitized ssSSCs are not clear in the exact nature of encapsulation, nor on the precise ageing and testing conditions[3,4,16,17,19,21]. Additionally, ultra violet (UV) cut off filters are often employed, but the effect of UV light on solar cell stability is not yet well understood[3,4,16,17,19,21]. In contrast, a great deal of literature is available on the subject of long term stability regarding polymer-based solar cells, which require encapsulation to protect the organic components from oxidation in air[22–25]. Air sensitivity of organics, coupled with the moisture sensitivity of the current generation of perovskite absorbers, makes it clear that this new class of solar cells will require a high level of encapsulation to attain eventual outdoor lifetimes of over 25 years[3,16,26].

A number of previous reports on dye sensitized ssSSCs elude to significant performance deteriorations when operated in an inert atmosphere. This has been assigned to changes in the metal oxide surface and changes to the level of p-doping in the hole-transporter[20,27–29]. With this in mind, this chapter investigates the influence of UV light and atmospheric conditions on ssSSCs employing both dye-sensitizers (D102 and C106) and the $CH_3NH_3PbI_{3-x}Cl_x$ perovskite absorber.

7.3

Influence of Atmosphere and UV light on ssSSC Performance

Figure 7.1 shows the evolution of solar cell performance parameters over time under illumination for perovskite sensitized ssSSCs, measured in air, encapsulated in a nitrogen filled glove box, and encapsulated but with filtration of the UV component of the light by employing a 435 nm UV cut off filter. It should be noted that these solar cells, comprised of an 800 nm TiO_2 scaffold infiltrated with 20 wt % perovskite precursor solution, are very much similar to conventional dye sensitized ssSSCs, as described in Chapter 6. Surprisingly, the encapsulated sensitized TiO_2 cells decay much faster than the non-encapsulated solar cells when subject to full spectrum sun light, falling to less than 10 % of their initial performance within 5 hours due to a rapid decrease in photocurrent and a smaller decrease in photovoltage. This is in contrast to only 50 % decay over 5 hour illumination for the non-encapsulated devices tested in ambient conditions. When a UV filter (435 nm cut-off) is employed, however, the solar cells are more stable, with

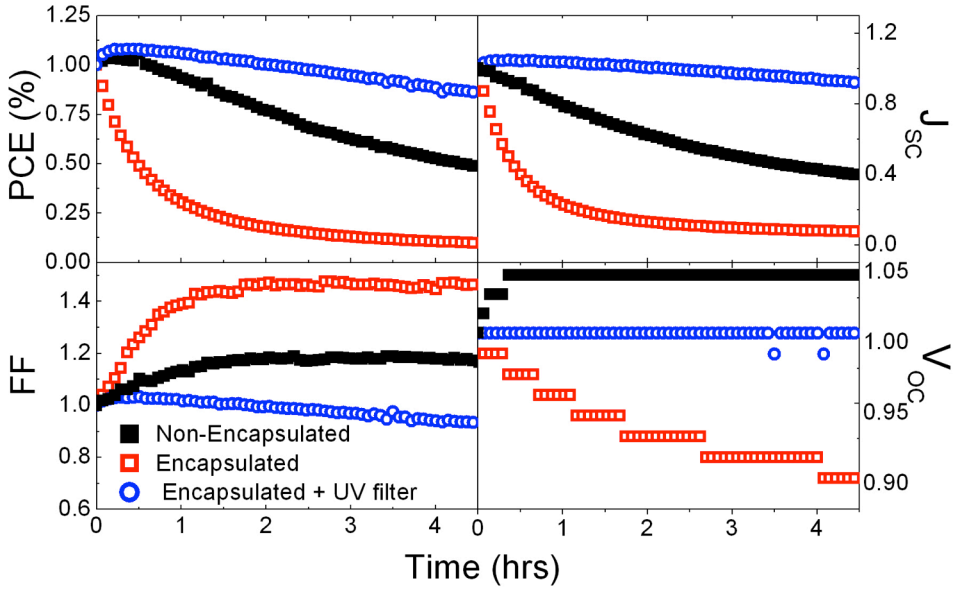

Figure 7.1. Evolution of normalized solar cell performance parameters, power conversion efficiency (PCE), short circuit current (J_{sc}), fill factor (FF), and open circuit voltage (V_{oc}) over 5 hours of AM1.5 100 mW cm^{-2} solar illumination. The figure compares the behaviour of perovskite sensitized TiO_2 solar cells which are non-encapsulated and encapsulated with and without a < 435 nm cut-off filter. All devices had initial PCEs of at least 5 %, with short circuit currents of at least 10 mA cm^{-2}, representing typical working solar cells of this type. The devices were prepared together with Giles E Eperon at the Department of Physics at the University of Oxford.

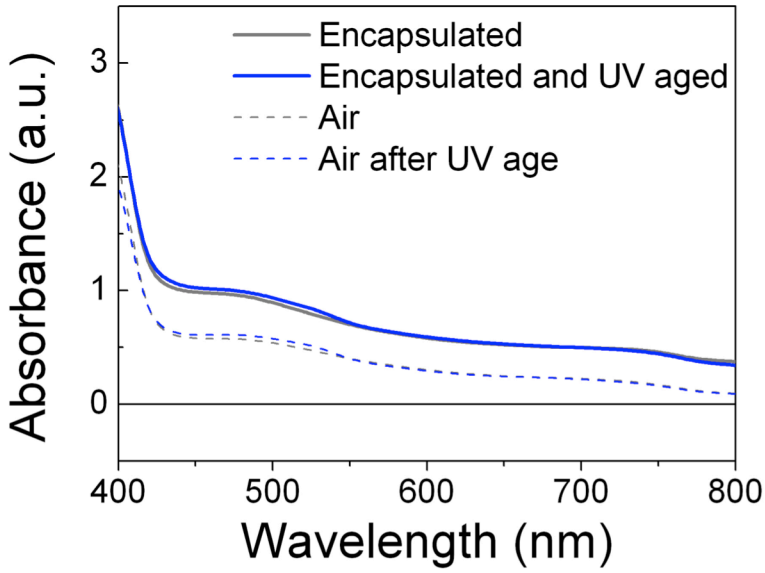

Figure 7.2. UV-vis absorption taken for encapsulated and non encapsulated perovskite sensitized ssSSCs (the same as those in Figure 7.1 but without top gold electrode) before and after 3 hours of full AM1.5 100 $mWcm^{-2}$ solar illumination. The offset for the encapsulated samples is simply due to the extra reflectionat the air / glass interface of the encapsulating glass.

the encapsulated sensitized TiO_2 cells decaying to only 85 % of their initial performance within the 5 hours. Notably for the UV filtered device (435 nm cut-off), the degradation of the photocurrent is much diminished (but still present), while the photovoltage stays constant and the fill factor decreases slightly. The fill factor drop may simply be due to non-optimum doping of the HTM.[15] One simple cause for the drop in photocurrent could be that the perovskite material is degrading, so that less light is absorbed. Figure 7.2, however, demonstrates that the UV-vis absorption spectra of the samples remains unchanged for both encapsulated and non-encapsulated devices after full solar simulated light exposure.

To ensure that this effect is not unique to perovskite sensitized ssSSCs, similar studies were carried out on dye sensitized ssSSCs. The *J-V* curves for both D102 and C106 sensitized ssSSCs in a nitrogen-filled testing chamber are presented in Figures 6.2a and 6.2b, respectively. Here, there is a similar rapid drop in photocurrent upon light exposure under inert conditions (the cells were tested under vacuum in a sealed testing chamber). Again, application of a < 435 nm cut-off filter, while diminishing the total initial photocurrent simply because there is less light on the sample, results in stable device operation. The fact that both perovskite and dye sensitized ssSSCs behave identically with respect to UV light and inert testing

conditions suggests that the problem does not lie with the perovskite absorber material, but elsewhere, and is common to all ssSSCs. The fact that the same behaviour is seen upon encapsulation in an inert atmosphere as upon evacuation of the entire testing chamber suggests that the degradation is not caused by the sealing procedure itself, but rather by the lack of oxygen and possibly water normally present in air.

Chapter 4 and 5 discussed the importance of oxygen induced doping the HTM in ssSSCs. A natural first thought is that the observed degradation in an inert

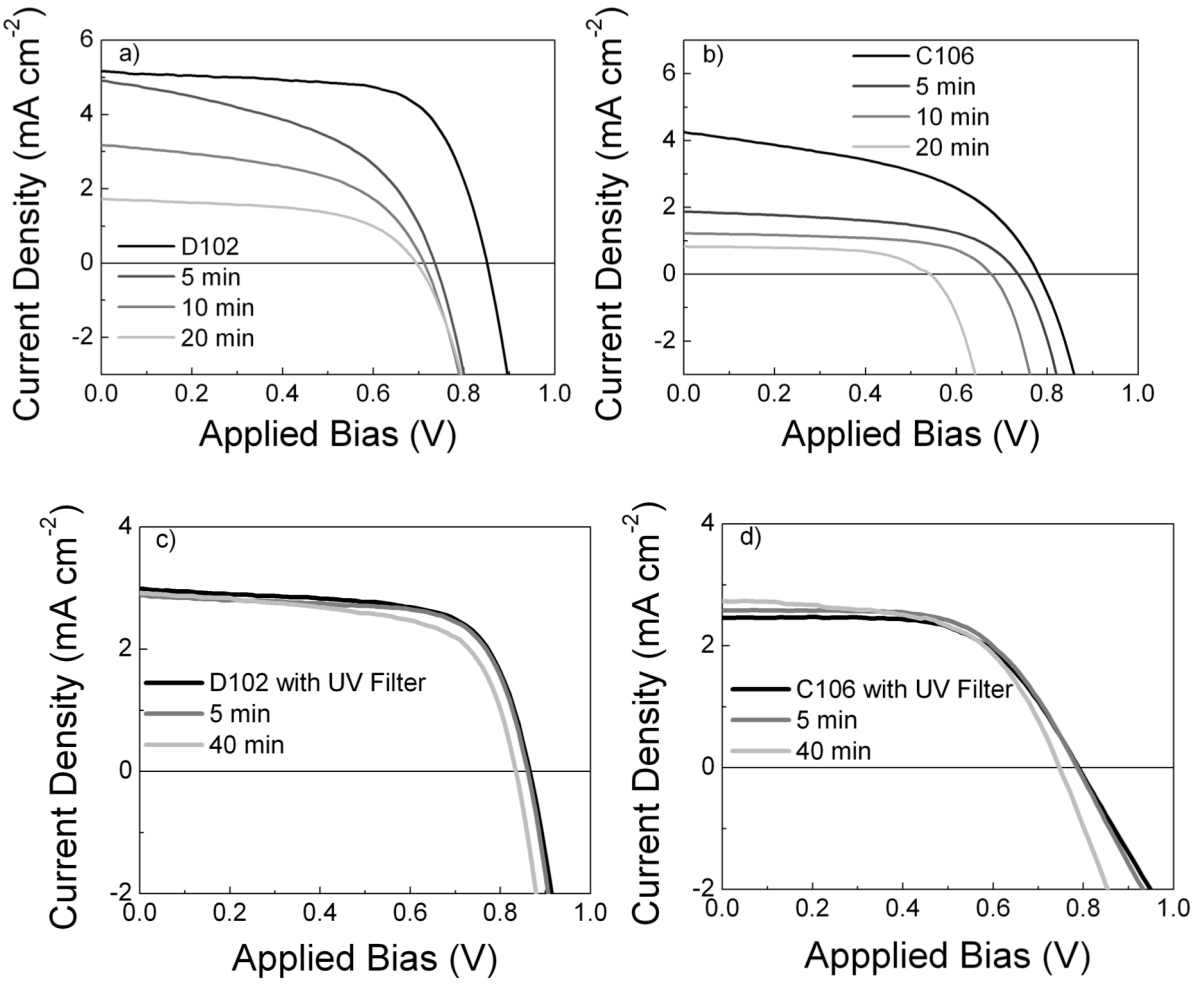

Figure 7.3. *J-V* characteristics of dye sensitized ssSSCs as a function of time, tested under vacuum in a sealed testing chamber. (a) shows the characteristics of D1O2 sensitized ssSSCs, while (b) shows the behaviour of C106 sensitized ssSSCs. Both show very similar behaviour. The devices were again exposed to air for 3 days in the dark and recovered up to 90 % of the initial performance. (c) and (d) show the same as (a) and (b), but with the addition of a < 435 nm cut-off filter removing the UV component of the light. After the devices were mounted, the chamber was purged with nitrogen and then evacuated three times. Then it was evacuated for 2 hours by an oil pump, and then sealed. The incident light was 70 mW cm^{-2} in intensity, and no UV cut-off filters were employed. The current for the cells under the UV filter is naturally lower due to the extra reflections at the air/filter/air interfaces as well as the simple fact that none of the light at higher energy than 435 nm is incident on the samples.

atmosphere, under full solar spectrum illumination is due to changes in the HTM conductivity. On the other hand, the *J-V* curves presented in Figure 7.3 show no evidence for an increased series resistance, as would be expected if the cause for degradation was a "de-doping" of the HTM. To investigate atmospheric effects on ssSSCs more closely, all the steps of dye (D102) sensitized ssSSC assembly, starting with dye sensitization, were performed in a nitrogen-filled glovebox. The completed devices (with the optimized additive concentration) were mounted in a testing chamber that was sealed before removal from the glovebox. The *J-V* characteristics were then taken for the devices in the inert condition, after stabilization in air, and then again after placing in a nitrogen environment and exposing to unfiltered simulated sunlight for 5 minutes. The results are plotted in Figure 7.4.

The *J-V* curve of the device before exposure to oxygen looks remarkably similar to that presented in Chapter 5 for ssSSCs without LiTFSI, again reinforcing the importance of oxygen and LiTFSI induced p-doping of the HTM. After two days in air, all of the device parameters are vastly improved, and the slope of the *J-V* curve is much steeper near open circuit as might be expected from the increased oxygen-induced doping of the hole transporter described in Chapters 4 and 5[27,28,30]. After

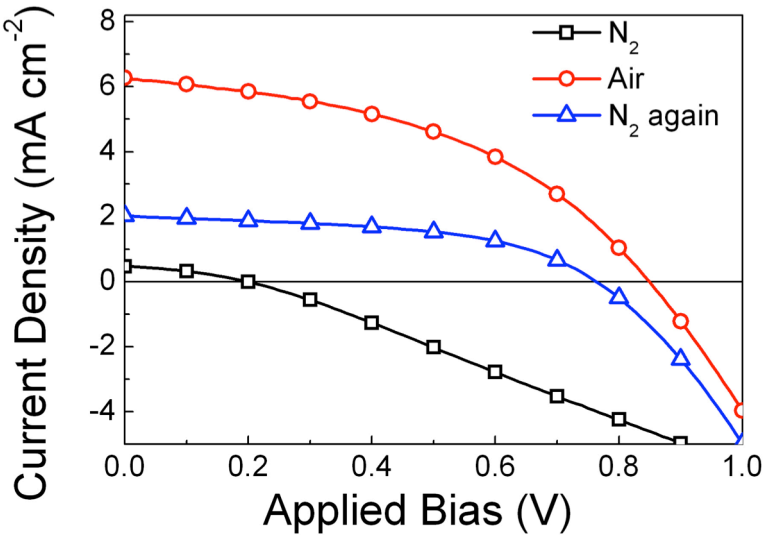

Figure 7.4. Current density-voltage curves for a representative D102 sensitized ssSSC fabricated (every step after the $TiCl_4$ treatment) in a nitrogen-filled glovebox. The black open squares depict the JV curve for the solar cell measured in a nitrogen atmosphere, without any air exposure. The open red circles depict the JV curve for the same solar cell after 48 hours of air exposure. The open blue triangles depict the JV curve of the cell after another 48 hours in a nitrogen filled glovebox, and tested in a nitrogen environment after 5 minutes of unfiltered light exposure. These cells were measured in a small testing chamber at 70 mW cm^{-2} solar simulated light intensity.

two days back in the nitrogen filled glovebox, and 5 minutes under the solar simulator, the solar cells have again dropped dramatically in photocurrent. Notably, the slope of the *J-V* curve near open circuit is very similar to those seen in air, suggesting that the series resistance through the hole transporter has not been significantly altered by placing the devices back in nitrogen. This suggests that after oxygen-induced p-doping of the hole transporter, which is stable even after the removal of oxygen (as shown in Chapter 4)[28], the solar cells suffer from a decreased photo-current when tested in an oxygen-free atmosphere. This is then unlikely to be related to a change in conductivity of the hole transporter. This will be conclusively demonstrated below. Hence, it is very likely that the degradation mechanism is taking place at the TiO_2 surface.

7.4

Charge Collection in "Aged" Devices

In an attempt to determine whether the drop in photocurrent is caused by deterioration in charge generation or charge collection, simultaneous charge extraction (at short circuit) and transient absorption spectroscopy (TAS) measurements were performed on complete solar cells with semi-transparent electrodes (15 nm gold), using a 550 nm laser pulse as the excitation. As shown in Chapter 5, this method can be used to quantify the extinction coefficient of oxidized Spiro-MeOTAD in devices known to have near unity charge collection efficiency[30]. Here, this technique is used to simultaneously monitor the decay of the oxidized Spiro-MeOTAD signal and the decay of the photocurrent following a light pulse, before and after ("aged") degradation of the sealed TiO_2-based solar cells. It is then possible to determine the ratio of charges generated (G, determined from the early time oxidized Spiro-MeOTAD absorption signal) to the total number of charges collected (C, determined from the time integrated short-circuit photocurrent perturbation). The ratio between the charges generated (G) to those collected (C) is a direct measurement of the collection efficiency (C / G × 100 %). Figure 6.5a depicts the transient short-circuit photocurrent trace, and Figure 6.5b shows the transient

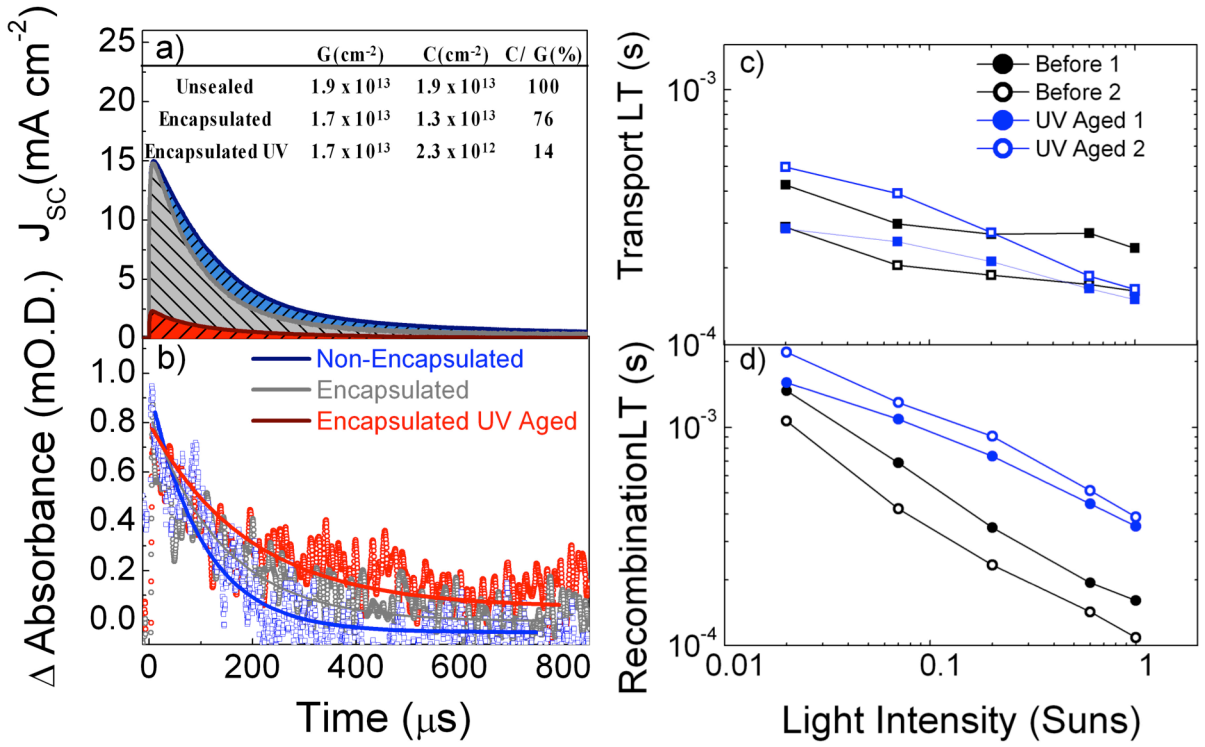

Figure 7.5. In the top panel (a), the current collected from full perovskite -sensitized TiO_2 solar cells with semi-transparent electrodes (15 nm gold) is plotted against time after the excitation (5 ns 550 nm). Non-encapsulated (blue), encapsulated after ambient light exposure (grey) and encapsulated after UV aging (red) (5 minutes at 40 mW cm^{-2} 365 nm) are compared. The area underneath the curves represent the total amount of collected charge. The bottom panel (b) shows the TAS trace at short circuit, monitoring the hole on Spiro-MeOTAD (probed at 510 nm), performed simultaneously with the current extraction. The lines are merely guides to the eye. The table in Figure 7.5a shows the charge generated (G, estimated from the early time transient absorption signal), collected (C, by integrating the current decay), and the ratio between the two as a percentage (C / G). The laser intensity was 80 μJ cm^{-2}, giving charge densities similar to those found in devices under operating conditions.[28] Short circuit charge transport (c) and recombination lifetimes (d) for encapsulated perovskite sensitized ssSSCs are given before (black squares and circles) and after (blue squares and circles) an hour of exposure to full spectrum solar simulated sunlight AM1.5 at 100 mW cm^{-2}.

absorption signal. The table inset to Figure 6.5a gives the calculated values for G, C and charge collection efficiency. For this analysis, the number of holes in Spiro-MeOTAD is assumed to be equivalent to the number of electrons in the TiO_2, an assumption verified later.

The charge collection efficiency for unsealed devices is approximately unity. Upon sealing and subsequent measuring, there is a moderate decrease in the estimated charge collection efficiency, to 76%, but continuous exposure to the 550 nm laser for an hour does not result in further deterioration. In contrast, subsequent

exposure of the same cells (Encapsulated UV Aged) to 5 minutes of 365 nm light (40 mW cm^{-2}) results in a substantial drop of the photocurrent extraction by close to a factor of 7 with the collection efficiency dropping to 14%. By simultaneously monitoring the absorption of oxidized Spiro-MeOTAD (Figure 3b) while these photocurrent extraction measurements are performed, it is clear that the number of generated charges is not strongly affected by the encapsulation or the UV exposure. In addition, the decay lifetime of the oxidized Spiro-MeOTAD signal at short circuit is also not sped up, but actually somewhat slowed suggesting that the charge extraction rate has slowed. Since the short circuit TAS decay is a superposition of charge collection and recombination however, it is difficult to extract detailed information from this change in rate of decay.

To understand the nature of the decrease in collection efficiency and gain an insight into electronic changes in the photoactive layer, small perturbation photocurrent and photovoltage decay measurements (described in Chapter 3) were performed before and after UV light exposure and are displayed in Figures 7.5a and 7.5d respectively. At a given background light intensity, there is no discernible change in the charge transport lifetime, while recombination lifetimes appear to become slightly (factor of 2) longer after UV aging. This is at odds with the direct measurement of the collection efficiency presented in Figure 7.5a since the transient measurements would suggest an increase in the charge collection efficiency. To account for the lost charge after UV aging, it is proposed that UV-degraded cells suffer from a deep trapping of injected electrons within newly available sites in the TiO_2. The photocurrent extraction measurements suggest that these trapped electrons are immobile, while the TAS shows that they recombine with oxidized Spiro-MeOTAD species on the μs - ms time-scale. The charge that is collected must still be transported via the accepted trap limited diffusion process through shallow trap sites in the TiO_2 described in Chapter 2, distinct from the deep UV generated traps, explaining the negligible change in transport lifetimes and hence collection efficiencies determined via small perturbation photocurrent decay measurements.

7.5

Electron Trapping in Aged ssSSCs

If a large portion of the injected electrons in the TiO_2 are indeed deeply trapped and immobile, as suggested by the charge collection measurements above, this can be confirmed via time resolved conductivity measurements. Chapter 5 has introduced a new technique, combining conductivity measurements of dye sensitized TiO_2 with TAS[30]. This technique was applied to observe the effects of UV aging on the conductivity of electrons injected into the TiO_2 by a sensitizer. Using a sensitizing dye (C106) rather than the perovskite sensitizer makes it possible to monitor the photo-bleach of the ground state dye absorption to gain a quantitative insight into the density of injected electrons. This is a valid substitution, since all encapsulated ssSSCs appear to respond very similarly to UV exposure (Figures 7.1-7.4). The absence of a hole transporter or the perovskite means that it is possible to measure electron conductivity in the TiO_2 only, as discussed in Chapter 5.

Figure 7.6 shows the laser pulse induced increase in conductivity before and after UV exposure of encapsulated TiO_2 conductivity samples. The first noticeable difference before and after UV light exposure is the increase in absolute background conductivity ($t < 0$) after aging. One would expect such an increase in background conductivity to represent a filling of the TiO_2 sub gap states, increasing the electron mobility, as was observed in Chapter 5[30–33].

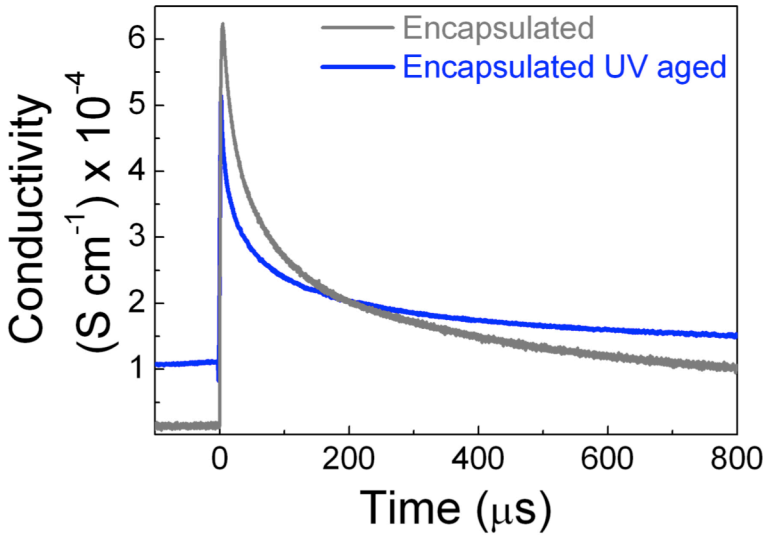

Figure 7.6. The photo-induced change in conductivity of dye-sensitized TiO_2, measured after a 5 ns laser excitation (550 nm at 80 μJ cm^{-2}).

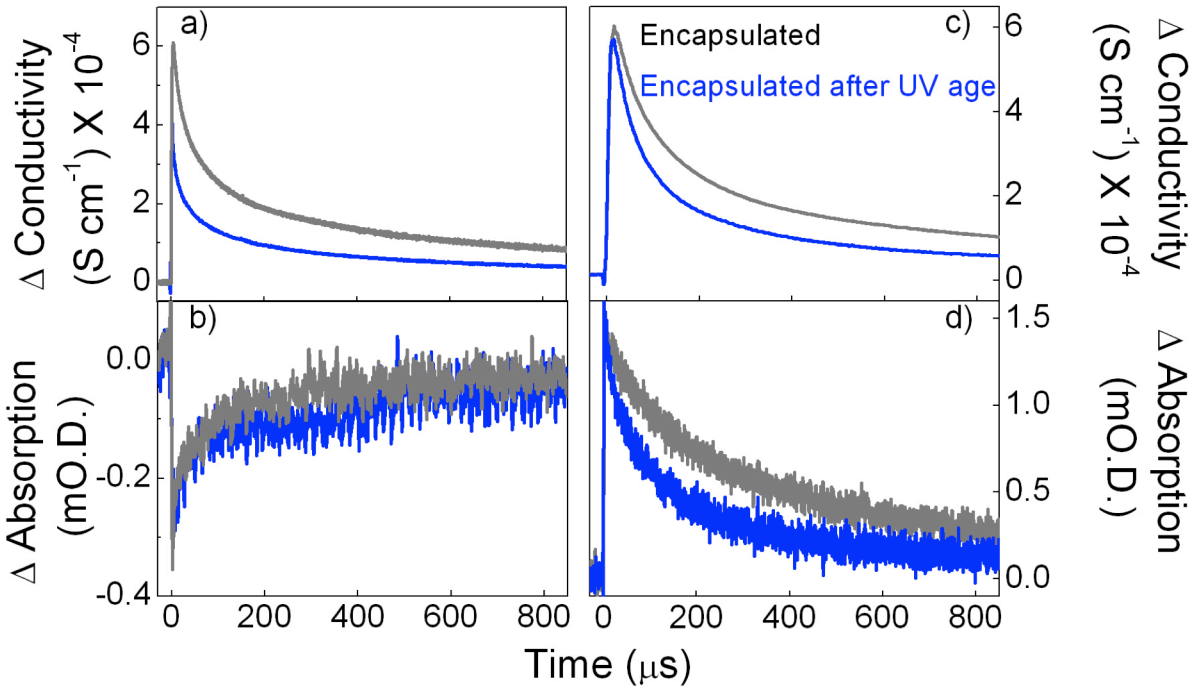

Figure 7.7. (a) The photo-induced change in conductivity of dye-sensitized TiO_2, measured after a 5 ns laser excitation (550 nm at 80 μJ cm^{-2}), and (b) simultaneous transient absorption spectroscopy to monitor the bleach of the dye ground state absorption at 500 nm. Grey corresponds to the encapsulated sample before UV exposure, while the blue trace corresponds to the same sample after 5 minutes UV exposure (40 mW cm^{-2} at 365 nm). The same experiment is performed for samples where the Spiro-MeOTAD is contacted to monitor changes in photo-induced conductivity (c) of the Spiro-MeOTAD and photo-induced hole population in Spiro-MeOTAD (d), as monitored at 510 nm probe wavelength.

The UV aging in absence of oxygen should then result in an increased mobility and overall conductivity for injected electrons. For a closer analysis, the photo-induced change in conductivity is plotted along with the photo-induced bleach of the dye groundstate (due to charge transfer to TiO_2) absorption (500 nm) in Figure 7.7a and 7.7b. Here, it is apparent that although the number of electrons injected into the TiO_2 upon excitation of the dye does not change, the resulting photo-induced increase in conductivity is significantly less for the UV aged samples. This is strong evidence that a large fraction of injected electrons are deeply trapped (either directly or after injection on a time scale much faster than the resolution in the TAS setup of < 5 ns) and do not contribute to the measured conductivity. The same experiment was performed to monitor hole conductivity in the HTM by infiltrating the dye-sensitized TiO_2 with Spiro-MeOTAD, and monitoring the oxidized Spiro-MeOTAD density as described in Chapter 5. The data is presented in Figures 7.7c and 7.7d, and demonstrate negligible change in the photo-induced conductivity of the hole

transporter after UV aging, while the recombination rate is increased. The combined measurements on dye-sensitized TiO_2 with and without the hole transporter give a clear picture of what is occurring: photo-induced electron transfer to TiO_2 and hole-transfer to Spiro-MeOTAD are largely unaffected, but a large fraction of the electrons injected into TiO_2 are trapped in deep sites from which they cannot move, eventually recombining with holes in Spiro-MeOTAD.

7.6

Mechanisms of Electron Trapping

To justify the degradation mechanism, the surface chemistry of TiO_2 must be considered. TiO_2 is known to contain many oxygen vacancies (or Ti^{3+} sites), particularly at the surface, which are effectively deep electron donating sites[34,35]. The electrons in these sites, at approximately 1 eV below the conduction band edge[36], interact with molecular oxygen in the atmosphere, which adsorbs to the oxygen vacancy sites[37–41]. As a result, a charge transfer complex (O_2^- - Ti^{4+}) is formed[39–42]. Based on the referenced work on oxygen adsorption on TiO_2 surfaces and the findings presented here, the mechanism illustrated in Figure 7.8 is proposed to be responsible for the photocurrent degradation in the solar cells. Upon bandgap excitation of TiO_2, an electron-hole pair is formed. The holes in the valance band have been shown to recombine with the electron at the oxygen adsorption site, desorbing the oxygen[40,42]. This leaves a free electron in the conduction band and a positively charged, unfilled oxygen vacancy site at the TiO_2 surface. It seems likely that it is in the now unfilled deep trap sites that the lost photo-induced electrons are trapped, and from which they recombine with holes in Spiro-MeOTAD[43–45]. Chapters 4 and 5 demonstrated that Spiro-MeOTAD is heavily p-doped when used as the HTM in such solar cells, so that there are excess holes (more than the photo-generated hole density at 1 sun), which will readily recombine with the free electron left behind from the bandgap excitation of the TiO_2 either directly or through the now empty surface states which may act as recombination centers[27,28,30]. Since the rate of oxygen desorption (and hence activation of these trap sites) is likely to be low and reversible,[40,41] the steady-state number of empty deep trap sites will be dependent upon the partial pressure of oxygen in the hole-

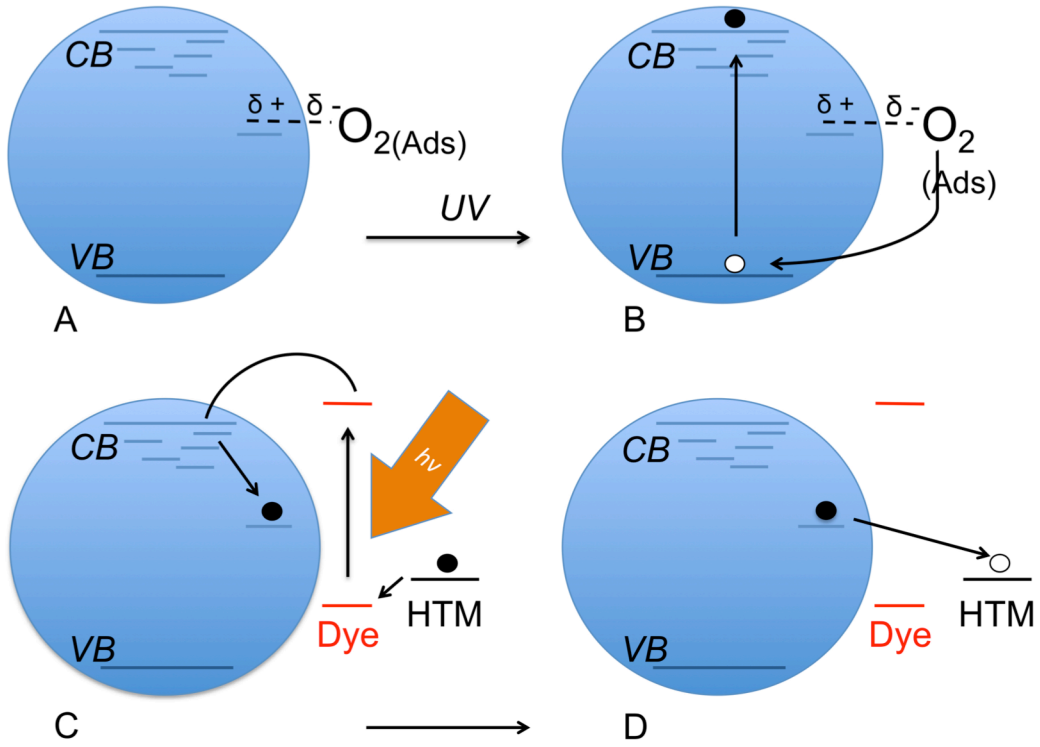

Figure 7.8. Upon UV light absorption, the photo-generated holes in TiO_2 react with the oxygen radicals adsorbed at surface oxygen vacancies (A-B). Molecular oxygen is desorbed from these sites, leaving unoccupied, deep surface traps sites and a free electron per site. These electrons will recombine with the excess of holes in the doped hole transporter. Upon photo-excitation of the sensitizer, electrons are injected either (1) into the conduction band from which they become deeply trapped, or (2) directly into the deep surface traps (C). These deeply trapped electrons are not mobile, and recombine readily with holes on the Spiro-MeOTAD hole transporter (D).

transporter, and hence far lower in the presence of oxygen than in the absence of oxygen. By this means, oxygen serves to pacify these sites. The above discussion is just proposed as a hypothesised mechanism for sensitized TiO_2 solar cell degradation in the absence of oxygen. Further studies are required to definitively establish the mechanism. Interestingly, acetonitrile has been shown to pacify Ti^{3+} oxygen vacancies sites in TiO_2[34,35]. This may explain why this rapid UV degradation has not been reported for liquid electrolyte DSSCs employing nitrile based solvents, although as mentioned earlier, UV cut-off filters are usually employed during long term stability measurements[14,46–48].

7.7

Reducing UV Instability by Slowing Electron-Hole Recombination

Having established that TiO_2 based solar cells suffer from an inherent instability under UV illumination, there are several options to achieve superior stability. Obvious routes are to develop a route to effectively and stably pacify the TiO_2 surface states in the solid-state, prevent the UV light from reaching the mesoporous TiO_2 while still using it to generate photocurrent, slow recombination of trapped electrons with holes so that the sites "fill up", or completely remove the mesoporous TiO_2. With regard to the second option, down-converting nanoparticles have been demonstrated to efficiently absorb UV light and re-emit visible light that can be harvested by the sensitizer in ssSSCs[49]. Developing such routes to harvest all of the light of shorter wavelengths than 435 nm before it reaches the mesoporous TiO_2 should allow for enhanced stability without a loss in photocurrent.

If the recombination rate between trapped electrons and Spiro-MeOTAD were reduced, many more of the deep trap sites would be filled at steady state under

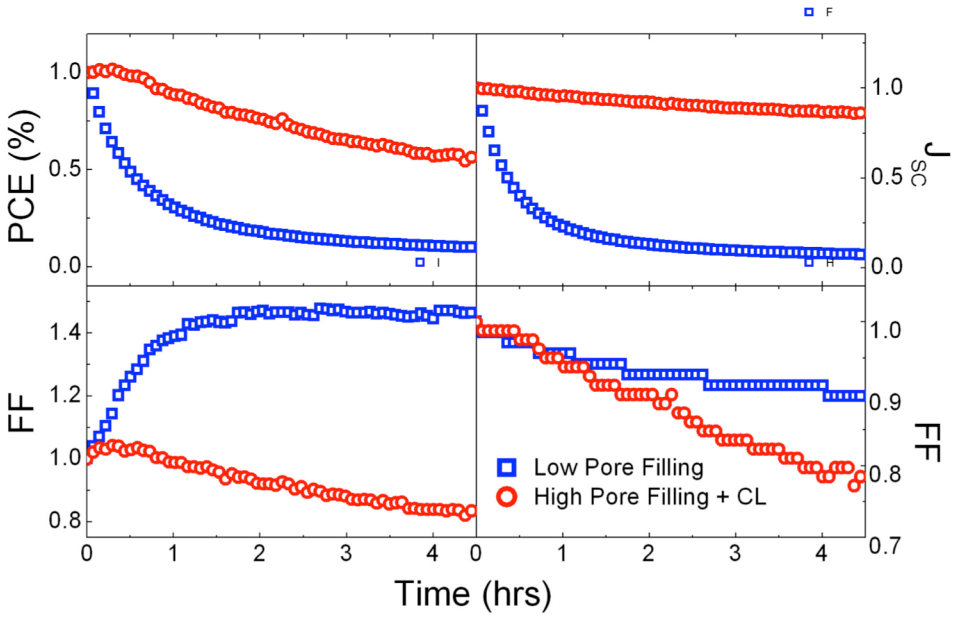

Figure 7.8. Evolution of normalized solar cell performance parameters, power conversion efficiency (PCE), short circuit current (J_{SC}), fill factor (FF), and open circuit voltage (V_{OC}) over 5 hours of AM1.5 100 $mWcm^{-2}$ solar illumination. The figure compares the behaviour of encapsulated perovskite sensitized TiO_2 solar cells with low pore filling fractions to those with high pore filling fractions and a capping layer (CL), as described in Chapter 6. The devices were prepared together with Giles E Eperon at the Department of Physics at the University of Oxford.

illumination. If the recombination were to be slowed enough, it would be possible to effectively fill all of the sites, to result in improved charge transport and collection efficiencies (similar to what was demonstrated in Chapter 6) even upon UV light exposure. Chapter 6 demonstrated that structures with high perovskite pore filling fractions and thick perovskite capping layers benefit from slowed recombination rates because the contact between TiO_2 and Spiro-MeOTAD is removed. As such, devices with this architecture, which deviates somewhat from the ssSSC architecture, should benefit from relatively improved UV stability when encapsulated.

Solar cells with high perovskite pore filling fractions and a perovskite capping layer were prepared (as described in Chapter 6), encapsulated, and exposed to unfiltered solar simulated light for 5 hours. The normalized results are plotted in Figure 7.8, and compared to the behaviour of the solar cells with low perovskite pore filling fractions (and hence a typical ssSSC architecture) described in Figure 7.1. It is immediately apparent that the photocurrent and hence performance of the devices with high pore filling and a perovskite capping layer are far more stable than that of perovskite sensitized ssSSCs. This supports the hypothesis that trapped electrons recombining with Spiro-MeOTAD drives the rapid deterioration of performance, as it enables a constant emptying of the trap sites. In the case with high perovskite pore filling fraction, recombination at the TiO_2 and Spiro-MeOTAD interface is not possible. The dominant recombination mechanism is likely to be between electrons in TiO_2 and holes in the perovskite, of which there are unlikely to be many because of rapid transfer to the Spiro-MeOTAD capping layer[8,50]. Recombination between TiO_2 surface states and holes in the perovskite may also not be as favourable as that between these sites and holes in Spiro-MeOTAD in ssSSCs[43], because the electron wavefunction overlap will necessarily be different. As a result, the steady state will be such that many of the sites will be occupied. As a result, fewer photo-generated charges are "lost".

7.8

Achieving 1000 Hours of UV Stability by Removing TiO_2

One option to overcoming UV instability of ssSSCs is of course to remove the source of the instability: the mesoporous TiO_2 layer. Perovskite based MSSCs have been recently developed, where the mesoporous TiO_2 is replaced with an insulating mesoporous Al_2O_3 scaffold (Figure 7.9)[2,3]. The solar cell architecture is displayed in Figure 7.9. Here, the perovskite itself performs the tasks of light absorption, charge separation, and charge transport to the electrodes in a thin film p-i-n solar cell[51]. Of course, these solar cells cannot be classified as ssSSCs, but still benefit from all the advantages coming with being solution processed. Removing the TiO_2 also removes one fundamental energy loss step: electron transfer to TiO_2, which means that MSSCs are capable of delivering far superior photovoltages of over 1 V at open circuit[2,3].

Figure 7.10 shows the device performance parameters, measured every 15 minutes whilst exposing the MSSCs to continuous simulated AM 1.5 (76.5 $mWcm^{-2}$) illumination at 40 ^oC with no UV cut-off filter present. It is quite evident that the perovskite MSSCs are indeed considerably more resilient to UV irradiation than the perovskite sensitized TiO_2 analogue. Contrary to the behaviour observed for TiO_2 based cells under UV light exposure (almost complete decay within 3 hours), the photocurrent remains stable at close to 15 mA cm^{-2} over the 1000 hour exposure

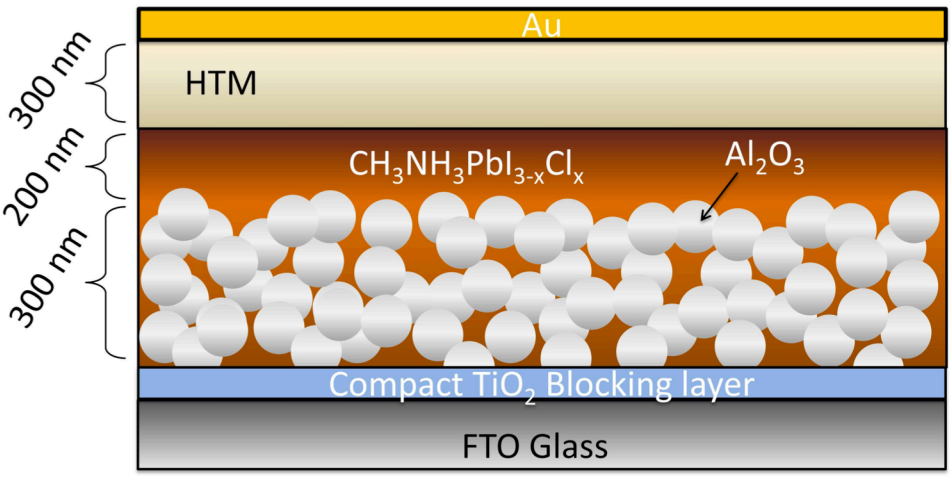

Figure 7.9. Schematic of a solar cell where the perovskite itself is functioning as both light absorber and charge carrier transporter. The Al_2O_3 is functioning as a scaffold to enhance film formation, while the Spiro-MeOTAD HTM is functioning as a hole extraction layer.

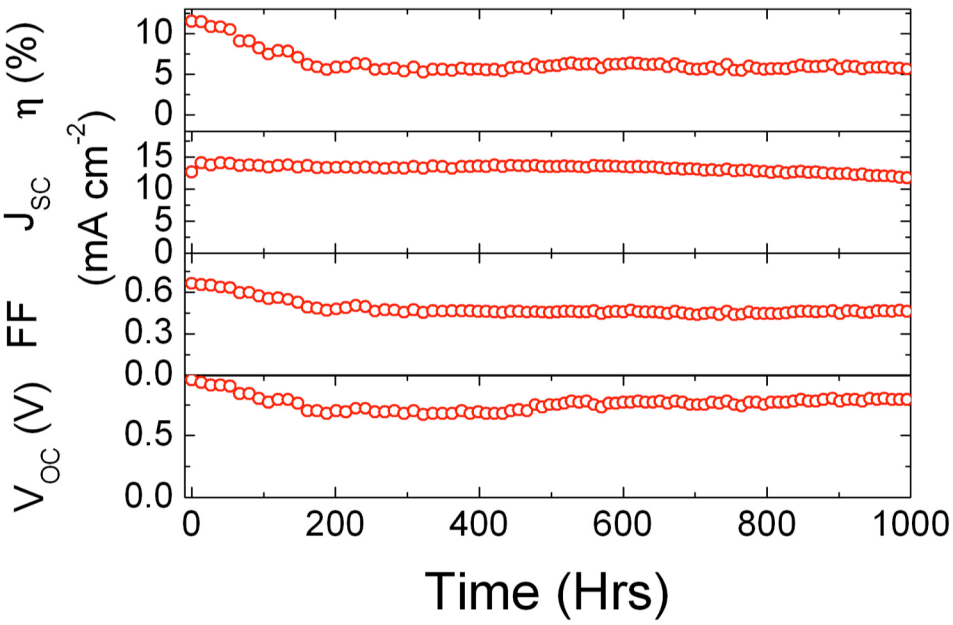

Figure 7.10. Solar cell performance parameters measured directly during aging of a representative Al_2O_3 based perovskite solar cell monitored every 15 minutes under continuous illumination of approximately one sun light intensity (actual intensity 76.5 $mWcm^{-2}$) at 40 ºC (Atlas CPSPlus Xenon lamp aging box). The device was encapsulated with epoxy resin and a glass cover slide in a nitrogen-filled glove box and no UV cut-off filters are employed. The devices were prepared together with Giles E Eperon at the Department of Physics at the University of Oxford.

period. There is some initial deterioration in the fill factor and open-circuit voltages of the cells over the first 200 hours of exposure. This could be due to a number of factors, including partial de-doping of the Spiro-MeOTAD hole conductor, oxygen desorption at vacancy sites on the remaining TiO_2 compact layer, changes to the Spiro-MeOTAD - Au electrode contact, or some subtle changes within the perovskite absorber. However, the optical stability of the mixed halide perovskite under full spectrum simulated sunlight has already been demonstrated[3], so it does not appear that this contributes to the initial degradation. This is supported by the lack of degradation in photocurrent over the first several hundred hours. The rudimentary encapsulation technique employed using epoxy resin may also induce some degradation due to migration of reactants into the photoactive layer. The possible sources of and mechanism for the long-term changes are currently under intensive investigation.

Still, following the initial drop within the first 200 hours, a stable power conversion efficiency of approximately 6 % is achieved which subsequently remains constant throughout the 1000 hours. This is already superior to any results obtained

previsously in this study or other in the literature when using TiO_2 as the electron transporter in ssSSCs and exposing the solar cells to full spectrum simulated sunlight[4,17,19–21]. A recent study by Burschka *et al.* did demonstrate methylammonium lead tri-iodide sensitized TiO_2 solar cells to be stable up to 500 hours[4], but this was accomplished under white light emitting diodes, in the absence of UV light, and such cells are likely to suffer from the same UV sensitivity as observed here for sensitized TiO_2 solar cells. The relative stability of the TiO_2 – free solar cells presented in Figure 7.10 also supports the mechanism of UV induced degradation of ssSSCs presented in this chapter.

7.9

Summary and Outlook

This chapter has identified a major instability of solid-state sensitized TiO_2 based solar cells; they are unstable to UV illumination when encapsulated in an inert atmosphere. Encapsulation is however, absolutely necessary to prevent rapid deterioration of the organic charge transport layers and absorbers. Unless addressed, such an instability will inhibit commercial deployment of these solar cells. It is possible to decrease the rate of performance deterioration by "shutting off" the primary recombination pathway by increasing the perovskite pore filling fraction in the perovskite ssSSCs. The Al_2O_3 based MSSCs circumvent this inherent instability, and display stable photocurrents under continuous full spectrum sun light for a period of over 1000 hours. Though this is only the first step in the path towards the requisite 25 year outdoor operational lifetime, it illustrates that the thin film and meso-superstructured perovskite solar cells have bi-passed a critical instability of the mesoporous TiO_2 based solar cells, and show significant promise as a large scale, long term energy source.

While the sensitized TiO_2 based solar cells do appear to be more stable when a UV filter is used, this comes at a cost of photocurrent, and requires an extremely stable and cheap UV-filter. Additionally, since the absorption tail of mesoporous TiO_2

extends into the visible, there may be degradation over a longer time scale due to absorption in the tail[52]. Indeed, the encapsulated TiO_2 - sensitized cells tested beneath a 435 nm cut-off filter do degrade to approximately 85 % of their initial performance over the first 4 hours (Figure 7.1), whereas the TiO_2 – free solar cells are perfectly stable (and even improve) over this short time period.

Chapter 6 demonstrated how it is possible to overcome thickness limitations in ssSSCs by utilizing highly absorbing organometal halide perovskite absorbers instead of sensitizing dyes. This approach has led to ssSSCs reaching over 17 % efficiency. The main remaining obstacle for commercialization is then the stability of the devices. This chapter has demonstrated that ssSSCs suffer from a major instability, that can however be overcome by using the perovskite absorber in a TiO_2 – free architecture. This work suggests that the future of solution processed hybrid photovoltaics may lie in novel structures that do not include the unstable TiO_2.

7.10

References

(1) Heo, J. H.; Im, S. H.; Noh, J. H.; Mandal, T. N.; Lim, C.-S.; Chang, J. A.; Lee, Y. H.; Kim, H.; Sarkar, A.; NazeeruddinMd, K.; Grätzel, M.; Seok, S. Il. *Nat Phot.* **2013**, *7*, 486.

(2) Ball, J. M.; Lee, M. M.; Hey, A.; Snaith, H. J. *Energy Environ. Sci.* **2013**, *6*, 1739.

(3) Lee, M. M.; Teuscher, J.; Miyasaka, T.; Murakami, T. N.; Snaith, H. J. *Science (80-.).* **2012**, *338*, 643.

(4) Burschka, J.; Pellet, N.; Moon, S.-J.; Humphry-Baker, R.; Gao, P.; Nazeeruddin, M. K.; Grätzel, M. *Nature* **2013**, *499*, 316.

(5) Ryu, S.; Noh, J. H.; Jeon, N. J.; Chan Kim, Y.; Yang, W. S.; Seo, J.; Seok, S. Il. *Energy Environ. Sci.* **2014**.

(6) Etgar, L.; Gao, P.; Xue, Z.; Peng, Q.; Chandiran, A. K.; Liu, B.; Nazeeruddin, M. K.; Grätzel, M. *J. Am. Chem. Soc.* **2012**, *134*, 17396.

(7) Eperon, G. E.; Burlakov, V. M.; Docampo, P.; Goriely, A.; Snaith, H. J. *Adv. Funct. Mater.* **2013**, *24*, 151.

(8) Stranks, S. D.; Eperon, G. E.; Grancini, G.; Menelaou, C.; Alcocer, M. J. P.; Leijtens, T.; Herz, L. M.; Petrozza, A.; Snaith, H. J. *Science (80-.).* **2013**, *342*, 341.

(9) Liu, M.; Johnston, M. B.; Snaith, H. J. *Nature* **2013**, *501*, 395.

(10) Liu, D.; Kelly, T. L. *Nat. Photonics* **2013**, *8*, 1.

(11) Wang, J. T.-W.; Ball, J. M.; Barea, E. M.; Abate, A.; Alexander-Webber, J. a; Huang, J.; Saliba, M.; Mora-Sero, I.; Bisquert, J.; Snaith, H. J.; Nicholas, R. J. *Nano Lett.* **2013**, *14*, 724.

(12) Wojciechowski, K.; Saliba, M.; Leijtens, T.; Abate, A.; Snaith, H. J. *Energy Environ. Sci.* **2014**, *7*, 1142.

(13) Bach, U.; Tachibana, Y.; Moser, J.; Haque, S. A.; Durrant, J. R.; Grätzel, M. *J. Am. Chem. Soc.* **1999**, *121*, 7445.

(14) Kroon, J. M.; Bakker, N. J.; Smit, H. J. P.; Liska, P.; Thampi, K. R.; Wang, P.; Zakeeruddin, S. M.; Grätzel, M.; Hinsch, A.; Hore, S.; Würfel, U.; Sastrawan, R.; Durrant, J. R.; Palomares, E.; Pettersson, H.; Gruszecki, T.; Walter, J.; Skupien, K.; Tulloch, G. E. *Prog. Photovolt Res. Appl.* **2007**, *15*, 1.

(15) Leijtens, T.; Ding, I. K.; Giovenzana, T.; Bloking, J. T.; McGehee, M. D.; Sellinger, A. *ACS Nano* **2012**, *6*, 1455.

(16) Kim, H.-S.; Lee, C.-R.; Im, J.-H.; Lee, K.-B.; Moehl, T.; Marchioro, A.; Moon, S.-J.; Humphry-Baker, R.; Yum, J.-H.; Moser, J. E.; Grätzel, M.; Park, N.-G. *Sci. Rep.* **2012**, *2*.

(17) Burschka, J.; Dualeh, A.; Kessler, F.; Baranoff, E.; Cevey-Ha, N.-L.; Yi, C.; Nazeeruddin, M. K.; Grätzel, M. *J. Am. Chem. Soc.* **2011**, *133*, 18042.

(18) Wang, P.; Zakeeruddin, S. M.; Moser, J. E.; Nazeeruddin, M. K.; Sekiguchi, T.; Grätzel, M. *Nat. Mater.* **2003**, *2*, 402.

(19) Wang, M.; Moon, S.-J.; Xu, M.; Chittibabu, K.; Wang, P.; Cevey-Ha, N.-L.; Humphry-Baker, R.; Zakeeruddin, S. M.; Grätzel, M. *Small* **2010**, *6*, 319.

(20) Docampo, P.; Snaith, H. J. *Nanotechnology* **2011**, *22*, 225403.

(21) Chen, C.-Y.; Wang, M.; Li, J.-Y.; Pootrakulchote, N.; Alibabaei, L.; Ngoc-le, C.-H.; Decoppet, J.-D.; Tsai, J.-H.; Grätzel, C.; Wu, C.-G.; Zakeeruddin, S. M.; Grätzel, M. *ACS Nano* **2009**, *3*, 3103.

(22) Brabec, C. J.; Gowrisanker, S.; Halls, J. J. M.; Laird, D.; Jia, S.; Williams, S. P. *Adv. Mater.* **2010**, *22*, 3839.

(23) Jørgensen, M.; Norrman, K.; Krebs, F. C. Stability/degradation of polymer solar cells. *Solar Energy Materials and Solar Cells*, 2008, *92*, 686–714.

(24) Krebs, F. C.; Spanggaard, H. *Chem. Mater.* **2005**, *17*, 5235.

(25) Peters, C. H.; Sachs-Quintana, I. T.; Mateker, W. R.; Heumueller, T.; Rivnay, J.; Noriega, R.; Beiley, Z. M.; Hoke, E. T.; Salleo, A.; McGehee, M. D. *Adv. Mater.* **2012**, *24*, 663.

(26) Noh, J. H.; Im, S. H.; Heo, J. H.; Mandal, T. N.; Seok, S. Il. *Nano Lett.* **2013**, *13*, 1764.

(27) Cappel, U. B.; Daeneke, T.; Bach, U. *Nano Lett.* **2012**, *12*, 4925.

(28) Abate, A.; Leijtens, T.; Pathak, S.; Teuscher, J.; Avolio, R.; Errico, M. E.; Kirkpatrik, J.; Ball, J. M.; Docampo, P.; McPherson, I.; Snaith, H. J. *Phys. Chem. Chem. Phys.* **2013**, *15*, 2572.

(29) Yang, L.; Xu, B.; Bi, D.; Tian, H.; Boschloo, G.; Sun, L.; Hagfeldt, A.; Johansson, E. M. J. *J. Am. Chem. Soc.* **2013**, *135*, 7378.

(30) Leijtens, T.; Lim, J.; Teuscher, J.; Park, T.; Snaith, H. J. *Adv. Mater.* **2013**, *25*, 3227.

(31) Eppler, A. M.; Ballard, I. M.; Nelson, J. In *Physica E: Low-Dimensional Systems and Nanostructures*; 2002; Vol. 14, pp. 197–202.

(32) Anta, J.; Nelson, J.; Quirke, N. Charge transport model for disordered materials: Application to sensitized TiO2. *Physical Review B*, 2002, *65*.

(33) O'Regan, B. C.; Lenzmann, F. *J. Phys. Chem. B* **2004**, *108*, 4342.

(34) Schwanitz U Hunger, R Mayer, T Jaegermann, W, K. W. *J. Phys. Chem. C* **2007**, *111*, 854.

(35) Schwanitz, K.; Mankel, E.; Hunger, R.; Mayer, T.; Jaegermann, W. Photoelectron Spectroscopy at the Solid–Liquid Interface of Dye–Sensitized Solar Cells: Unique Experiments with the Solid–Liquid Interface Analysis System SoLiAS at BESSY. *CHIMIA International Journal for Chemistry*, 2007, *61*, 796–800.

(36) Nakamura, I.; Negishi, N.; Kutsuna, S.; Ihara, T.; Sugihara, S.; Takeuchi, K. *J. Mol. Catal. A Chem.* **2000**, *161*, 205.

(37) Cronemeyer, D. C. *Phys. Rev.* **1959**.

(38) Bisquert, J.; Fabregat-Santiago, F.; Mora-Ser??, I.; Garcia-Belmonte, G.; Barea, E. M.; Palomares, E. *Inorganica Chim. Acta* **2008**, *361*, 684.

(39) Henderson, M. A.; Epling, W. S.; Perkins, C. L.; Peden, C. H. F.; Diebold, U. *J. Phys. Chem. B* **1999**, *103*, 5328.

(40) Lu, G.; Linsebigler, A.; Yates, J. T. *J. Chem. Phys.* **1995**, *102*, 4657.

(41) Lu, G.; Linsebigler, A.; Yates, J. T. *J. Chem. Phys.* **1995**, *102*, 3005.

(42) Munuera, G.; Rives-Arnau, V.; Saucedo, A. *J. Chem. Soc. Faraday Trans. 1 Phys. Chem. Condens. Phases* **1979**, *75*, 736.

(43) Bisquert, J.; Zaban, a; Salvador, P. *J. Phys. Chem. B* **2002**, *106*, 8774.

(44) Yu, Y.; Wu, K.; Wang, D. *Appl. Phys. Lett.* **2011**, *99*, 192104.

(45) Weidmann, J.; Dittrich, T.; Konstantinova, E.; Lauermann, I.; Uhlendorf, I.; Koch, F. *Sol. Energy Mater. Sol. Cells* **1998**, *56*, 153.

(46) Hinsch, A.; Kroon, J. M.; Späth, M.; Roosmalen, J. A. M. van; Bakker, N. J.; Sommeling, P. M.; Burg, N. P. G. van der; Kinderman, R.; Kern, R.; Herber, J.; Schill, C.; Schubert, M.; Meyer, A.; Meyer, T.; Uhlendorf, I.; Holzbock, J. In *16th European Photovoltaic Solar Energy Conference and Exhibition*; 2000; Vol. 1702, pp. 1–7.

(47) Sommeling, P. M.; Späth, M.; Smit, H. J. P.; Bakker, N. J.; Kroon, J. M. *J. Photochem. Photobiol. A Chem.* **2004**, *164*, 137.

(48) Pettersson, H.; Gruszecki, T. *Sol. Energy Mater. Sol. Cells* **2001**, *70*, 203.

(49) Wu, J.; Wang, J.; Lin, J.; Xiao, Y.; Yue, G.; Huang, M.; Lan, Z.; Huang, Y.; Fan, L.; Yin, S. *Sci. Rep.* **2013**, *3*.

(50) Marchioro, A.; Teuscher, J.; Friedrich, D.; Kunst, M.; van de Krol, R.; Moehl, T.; Grätzel, M.; Moser, J.-E. *Nat. Photonics* **2014**, *8*, 250.

(51) Edri, E.; Kirmayer, S.; Mukhopadhyay, S.; Gartsman, K.; Hodes, G.; Cahen, D. *Nat Commun* **2014**, *5*, 3461.

(52) Boschloo, G.; Fitzmaurice, D. *J. Phys. Chem. B* **1999**, *103*, 2228.

Chapter 8

Conclusions and Outlook

8.1

Summary of Key Findings of the Thesis

This thesis has studied solution-processed photovoltaics, with a specific focus on solid-state sensitized solar cells (ssSSCs). In particular, charge transport phenomena governing ssSSCs were investigated by a combination of established and new techniques. Throughout the thesis, the work has been very much focused towards understanding the importance of the findings on ssSSC power conversion efficiency (PCE) and stability under working conditions. The work presented here has provided new insights into the fundamental limits preventing ssSSCs from reaching comparable PCEs as their counterparts utilizing liquid redox electrolytes, and gone on to propose solutions. A critical and fundamental instability of ssSSCs was also identified to be due to the TiO_2 anode, and routes to overcome this instability were suggested and employed.

p-Doping of the most commonly employed HTM Spiro-MeOTAD was investigated in Chapter 4. The standard additive, LiTFSI, was shown to be involved in far more than had been previously assumed in the literature. Indeed, since the first conception of the ssSSC by Bach *et al.*[1] in 1998, the LiTFSI additive has been employed in high performance ssSSCs with the thought that it improves charge transfer from the sensitizer to the TiO_2 and slows recombination rates at the TiO_2 / HTM interface[1–3]. By a combination of conductivity measurements, solar performance measurements, absorption spectroscopy, and density function theory (DFT) calculations, the work presented here provided the first evidence that while the aforementioned effects did indeed play a role, one very important and previously overlooked role of the LiTFSI is to facilitate oxygen induced p-doping of the Spiro-MeOTAD. Previous findings in the literature and the results in Chapter 5 furthermore show that this effect is common to

most HTMs, whether they are small molecules or polymers[4–6]. By performing simple analysis on the current density – voltage (*J-V*) characteristics, this work demonstrated that this LiTFSI - facilitated p - doping is absolutely essential to minimize power losses due to series resistance through the HTM. This is a problem that will be even more important with ssSSCs delivering higher photo – currents. The findings presented in this thesis are particularly important when considering the fact that photovoltaic devices are required to have lifetimes of tens of years under harsh operating conditions. The reliance on dopants that interact with the atmosphere is unlikely to provide a long – term stable option for commercial application of ssSSCs, so that future research should focus on developing new stable dopants. In fact, work presented here has led to the development of new atmosphere – independent and stable p-dopants for use in ssSSCs[7]. Still, the optimal solution is of course to develop new transparent HTMs with high hole mobilities, so that doping is not required for efficient device performance.

To more quantitatively understand the impact of hole transport on device performance, it is important to consider that the charge carrier mobility of solution processed semiconductors is likely to vary with the charge density. This is the result of large defect densities. Since the steady-state charge density increases in a solar cell when going from short circuit to forward bias, understanding the charge density dependence of both electron and hole transport is essential to gain a complete picture of balanced ambipolar charge collection in all photovoltaic devices made of solution processed semiconductors.

With this in mind, Chapter 5 presented a new technique, making it possible to easily measure the mobility of semiconductors commonly used in both ssSSCs and bulk heterojunciton (BHJ) polymer blend solar cells, as a function of charge density. The technique moreover makes it possible to measure the charge transport in the architecture used in the actual solar cells, so that the mobility values extracted are directly applicable to solar cell operation. As such, the technique presented in Chapter 5 should allow for more accurate modelling of all solution processed solar cells, and should lead to improved understanding of charge transport within the solar cell architecture. The results presented in this chapter confirm the importance of p-doping the HTM as was suggested in Chapter 4. It was moreover possible to monitor

at which charge density ssSSCs will go from being electron to hole transport limited. This work provides the first conclusive evidence that while electron transport limits charge collection at short circuit, hole transport limits charge collection closer to the maximum power point and open circuit conditions in optimized ssSSCs.

The work done in Chapters 4 and 5 moreover made it possible to develop a novel understanding of why it has proved impossible to make ssSSCs more efficient simply by making them thicker. A great deal of research effort in the past 15 years has been in developing thicker ssSSCs to improve light harvesting[8–10]. The work presented here, however, demonstrates that the requirement to p-dope the HTM comes at the cost of a competing absorption in the form of the oxidized HTM absorption. Indeed, thicker ssSSCs require higher HTM doping levels to minimize series resistance losses, which leads to increased absorption losses due to the absorption of the oxidized HTM. As such, a possible solution could be, again, to develop new transparent HTMs with high mobility that can be readily infiltrated into a thick mesoporous TiO_2 scaffold. Alternatively, new highly absorbing sensitizers would improve the performance of ssSSCs in thin architecures.

Fortuitously, organometal trihalide perovskite sensitizers with large absorption cross-sections were developed concurrently with the work performed for this thesis[11,12]. This new class of absorbers allows for highly efficient thin ssSSCs to be realized. Moreover, the ability of the perovskite materials to themselves rapidly transport charge means that the requirements for efficient device architectures have changed[11,13,14]. Different ssSSC device architectures incorporating such perovskite were studied in Chapter 6, where insight was gained into how to improve the performance of TiO_2 based ssSSCs incorporating this new class of absorbers. Indeed, by changing the architecture from one where the perovskite merely sensitizes the TiO_2 surfaces to one where it completely fills the mesopores and leaves a solid capping layer on top of the mesoporous TiO_2 layer, it is possible to maintain greatly increased charge densities in the TiO_2. This leads to vastly improved charge collection rates and slowed charge recombination rates, as the recombination pathway at the TiO_2 / HTM interface has been removed. This work moreover suggests that improved performances could be achieved if alternative perovskite deposition methods are developed to enable 100 % pore filling fractions and capping

layer formation on thicker (but < 1.5 μm) TiO_2 scaffolds to improve light harvesting even further.

Having identified a system that appears to overcome the problems associated with ssSSCs presented in Chapters 4 and 5, it becomes important to consider the stability of high performance ssSSCs. Work presented in Chapter 7 identifies a critical instability due to the interaction of TiO_2 with the atmosphere and UV light. While it is essential to encapsulate photovoltaic devices using organic components and the highly water sensitive perovskite absorber[15–17], this work demonstrates that ssSSCs are unstable when encapsulated in inert conditions and exposed to UV light. This is linked to the presence of deep oxygen vacancy sites in the mesoporous TiO_2 scaffold. It was possible to slow the performance deterioration by using a device architecture with high perovskite pore filling, as this reduced the rate of recombination between trapped electrons in TiO_2 and holes in Spiro-MeOTAD, but the devices were still not absolutely stable. By completely removing the TiO_2 scaffold, and replacing it with an inert Al_2O_3 scaffold in what has been termed a meso-superstructured solar cell (MSSC)[11,18], 1000 hours of stable photo-current were realized under full simulated solar irradiation. This then strongly suggests that TiO_2 - based ssSSCs will require a great deal more work to become applicable in real-world aplications, while TiO_2 – free architectures may provide a more promising route.

This work has presented several conclusions useful to future development of solution processed photovoltaic devices. In particular, ssSSCs using the more weakly absorbing dye sensitizers would benefit greatly from the use of transparent HTMs with vastly improved hole transport to minimize series resistance losses, the need for doping, and associated parasitic absorption losses. This work does also suggest that all ssSSCs suffer from a fundamental stability problem. While this can be circumvented to some extent by simply placing a UV filter in front of the devices, this will result in an unavoidable efficiency drop and rise in cost. As a result, TiO_2 – free solar cells based on organometal trihalide perovskite absorbers, such as those recently developed and described in Chapter 7, may prove far more suited route to real – world application for solar energy production.

8.2

References

(1) Bach, U.; Tachibana, Y.; Moser, J.; Haque, S. A.; Durrant, J. R.; Grätzel, M. *J. Am. Chem. Soc.* **1999**, *121*, 7445.

(2) Kruger, J.; Plass, R.; Cevey, L.; Piccirelli, M.; Grätzel, M.; Bach, U. *Appl. Phys. Lett.* **2001**, *79*, 2085.

(3) Bai, Y.; Zhang, J.; Wang, Y.; Zhang, M.; Wang, P. *Langmuir* **2011**, *27*, 4749.

(4) Leijtens, T.; Ding, I. K.; Giovenzana, T.; Bloking, J. T.; McGehee, M. D.; Sellinger, A. *ACS Nano* **2012**, *6*, 1455.

(5) Abrusci, A.; Ding, I. K.; Al-Hashimi, M.; Segal-Peretz, T.; McGehee, M. D.; Heeney, M.; Frey, G. L.; Snaith, H. J. *Energy Environ. Sci.* **2011**, *4*, 3051.

(6) Xia, J.; Masaki, N.; Lira-Cantu, M.; Kim, Y.; Jiang, K.; Yanagida, S. *J. Am. Chem. Soc.* **2008**, *130*, 1258.

(7) Abate, A.; Hollman, D. J.; Teuscher, J.; Pathak, S.; Avolio, R.; D'Errico, G.; Vitiello, G.; Fantacci, S.; Snaith, H. J. *J. Am. Chem. Soc.* **2013**, *135*, 13538.

(8) Bach, U.; Lupo, D.; Comte, P.; Moser, J. E.; Weissortel, F.; Salbeck, J.; Spreitzer, H.; Grätzel, M. *Nature* **1998**, *395*, 583.

(9) Ding, I. K.; Tétreault, N.; Brillet, J.; Hardin, B. E.; Smith, E. H.; Rosenthal, S. J.; Sauvage, F.; Grätzel, M.; McGehee, M. D. *Adv. Funct. Mater.* **2009**, *19*, 2431.

(10) Snaith, H. J.; Humphry-Baker, R.; Chen, P.; Cesar, I.; Zakeeruddin, S. M.; Grätzel, M. *Nanotechnology* **2008**, *19*, 424003.

(11) Lee, M. M.; Teuscher, J.; Miyasaka, T.; Murakami, T. N.; Snaith, H. J. *Science (80-.).* **2012**, *338*, 643.

(12) Kim, H.-S.; Lee, C.-R.; Im, J.-H.; Lee, K.-B.; Moehl, T.; Marchioro, A.; Moon, S.-J.; Humphry-Baker, R.; Yum, J.-H.; Moser, J. E.; Grätzel, M.; Park, N.-G. *Sci. Rep.* **2012**, *2*.

(13) Heo, J. H.; Im, S. H.; Noh, J. H.; Mandal, T. N.; Lim, C.-S.; Chang, J. A.; Lee, Y. H.; Kim, H.; Sarkar, A.; NazeeruddinMd, K.; Grätzel, M.; Seok, S. Il. *Nat Phot.* **2013**, *7*, 486.

(14) Etgar, L.; Gao, P.; Xue, Z.; Peng, Q.; Chandiran, A. K.; Liu, B.; Nazeeruddin, M. K.; Grätzel, M. *J. Am. Chem. Soc.* **2012**, *134*, 17396.

(15) Brabec, C. J.; Gowrisanker, S.; Halls, J. J. M.; Laird, D.; Jia, S.; Williams, S. P. *Adv. Mater.* **2010**, *22*, 3839.

(16) Peters, C. H.; Sachs-Quintana, I. T.; Mateker, W. R.; Heumueller, T.; Rivnay, J.; Noriega, R.; Beiley, Z. M.; Hoke, E. T.; Salleo, A.; McGehee, M. D. *Adv. Mater.* **2012**, *24*, 663.

(17) Noh, J. H.; Im, S. H.; Heo, J. H.; Mandal, T. N.; Seok, S. Il. *Nano Lett.* **2013**, *13*, 1764.

(18) Ball, J. M.; Lee, M. M.; Hey, A.; Snaith, H. J. *Energy Environ. Sci.* **2013**, *6*, 1739.